SPECTROSCOPIC INVESTIGATION OF METAL-RNA INTERACTIONS

A Dissertation

by

MATTHEW VOGT

Submitted to the Office of Graduate Studies of
Texas A&M University
in partial fulfillment of the requirements for the degree of

DOCTOR OF PHILOSOPHY

December 2004

Major Subject: Chemistry

SPECTROSCOPIC INVESTIGATION OF METAL-RNA INTERACTIONS

A Dissertation

by

MATTHEW VOGT

Submitted to the Office of Graduate Studies of
Texas A&M University
in partial fulfillment of the requirements for the degree of

DOCTOR OF PHILOSOPHY

Approved as to style and content by:

Victoria J. DeRose (Chair of Committee)	
Marcetta Y. Darensbourg (Member)	Steven Wright (Member)
Paul A. Lindahl (Member)	Emile A. Schweikert (Head of Department)

December 2004

Major Subject: Chemistry

ABSTRACT

Spectroscopic Investigation of Metal-RNA Interactions. (December 2004)

Matthew Vogt, B.S., Trenton State College

Chair of Advisory Committee: Dr. Victoria J. DeRose

Metal-RNA interactions are important to neutralize the negative charge and aid in correctly folding the RNA. Spectroscopically active metal ions, especially Mn^{2+}, have been used to probe the type of interaction the metal has with RNA. In previous studies, the hammerhead ribozyme, an RNA motif that catalyzes a site-specific phosphodiester bond cleavage reaction, was determined by room temperature EPR (electron paramagnetic resonance) studies to have a set of tightly and weakly bound metal ions. Under high salt concentrations, the hammerhead was found to bind a single Mn^{2+} ion with high affinity and with a characteristic low temperature EPR signal.

Using site specific ^{15}N labeling of a guanine residue in conjunction with ESEEM (electron spin echo envelope modulation) spectroscopy, the high affinity Mn^{2+} ion was conclusively determined coordinated to G10.1 of the proposed A9/G10.1 site with four water molecules coordinated to the Mn^{2+} ion. EPR power saturation studies determined that under low salt conditions the hammerhead coordinates up to four Mn^{2+} ions in relatively close proximity compared to an RNA duplex.

EXAFS (extended X-ray absorption fine structure) spectroscopy was used to determine that a Cd^{2+} ion coordinates to both the Rp and Sp sulfur atoms of a phosphorothioate modification at the A9 phosphate of the hammerhead. Previous EXAFS results for the Mn^{2+} substituted A9 phosphorothioate suggested that the Mn^{2+} ion

coordinates to the oxygen atom for both isomers. Molecular modeling suggested that the A9/G10.1 metal site will twist the phosphate group in order to accommodate this coordination. A Mn-GMP and Mn-phosphate model complexes were prepared and characterized by EXAFS to assign the origin of the features observed for the hammerhead sample.

A series of RNA sequences with internal loops containing the sheared G-A metal ion binding motif showed greater thermal stabilization of the RNA structure in the presence of Mn^{2+} ions compared to sequences without the motif. The EPR binding isotherms also showed a set of moderately tight metal ion interaction while circular dichroism spectroscopy was used to investigate structural differences between the sequences. These results suggest a mostly electrostatic, not structural role, for the Mn^{2+} ion interactions with these sequences.

ACKNOWLEDGEMENTS

I would like to thank my adviser Dr. Victoria J. DeRose for critical guidance and support throughout my graduate career. Over the years the research has been challenging, rewarding and on the rare occasion actually fun.

I would also like to thank the members of the DeRose group both past and current. In particular, I would like to acknowledge former group members Sue and Ed for providing me extensive training for my research. I would also like to thank the current group members Aurelie, Nak-Kyoon, Murali, Shannon, and Edith. I would also like to acknowledge Murali for help with the EPR simulation program and useful discussion.

Most of all I need to thank my friends and family, without whom I may not have accomplished this. I greatly appreciate my parents who have been extremely supportive and understanding during my time in graduate school. There were both good and bad times and you helped me make it through. My heart goes out especially to Aurélie for all the fun we have had and the life we share.

TABLE OF CONTENTS

Page

ABSTRACT……. iii

ACKNOWLEDGEMENTS……. v

TABLE OF CONTENTS……. vi

LIST OF FIGURES…….. ix

LIST OF TABLES…… xii

CHAPTER

I INTRODUCTION…… 1

Nucleic acids……. 1
RNA folding…….. 4
Metal ion interactions…… 6
Metal ions as spectroscopic probes of RNA structure…... 8
Ribozymes……. 9
The hammerhead ribozyme……... 11

II MATERIALS AND METHODS……..…… 20

Preparation of RNA strands…….. 20
Phosphorothioate substituted RNA……... 21
RNA sample preparation for low temperature EPR……. 22
X-band EPR spectroscopy…… 22
EPR spectral simulation…… 25
Room temperature Mn^{2+} binding isotherms……. 25
Power saturation studies……... 26
ESEEM spectroscopy……... 28
Thermal denaturation of RNA…….. 30
CD spectroscopy……... 33
Molecular modeling of the A9/G10.1 site…… 34
EXAFS spectroscopy…… 35
Crystals of small model complexes…….. 38

III THE LOCATION AND COORDINATION SPHERE OF A HIGH AFFINITY MN^{2+} ION BINDING SITE IN THE HAMMERHEAD RIBOZYME…….. 40

Introduction……... 40

CHAPTER Page

Results and discussion…… 43
Characterization of G10.1 deoxy modified hammerhead.. 43
EPR spectra……..... 44
ESEEM spectroscopy……..... 46
ESEEM H_2O counting…… 47
Model of high affinity Mn^{2+} site……..... 49
Conclusion……. 51

IV INTERACTIONS OF MULTIPLE METAL IONS IN THE HAMMERHEAD RIBOZYME…… 55

Introduction……... 55
Results and discussion…….. 59
Specific vs. non-specific metal-RNA interactions…… 59
Low temperature EPR……... 61
Power saturation…… 62
Line broadening……. 66
Conclusion……. 67

V SPECTROSCOPIC STUDIES OF MODELS FOR METAL-RNA INTERACTIONS…… 71

Introduction……... 71
Results and discussion……... 74
Homogeneity of the Mn^{2+} high affinity site in the hammerhead…….. 74
EPR of small model complexes……. 76
EPR simulations……. 83
Conclusion……. 85

VI EXAFS STUDIES OF METAL-RNA INTERACTIONS……... 89

Introduction……... 89
Results and discussion…….. 93
EXAFS model complexes…….…… 93
Cd EXAFS…… 99
Molecular modeling…….. 103
Phosphorothioate effect at A9 site…… 104
Cd interaction at the A9 site……. 107
Conclusion…… 108

VII CHARACTERIZATION OF MN^{2+}-RNA INTERACTIONS WITH RNA SEQUENCES CONTAINING THE SHEARED G-A METAL ION BINDING MOTIF……. 112

CHAPTER Page

Introduction……... 112
Results and discussion……... 119
Melt profiles……... 119
Metal ion dependency……..... 124
Room temperature EPR……. 128
CD spectroscopy……..... 131
Conclusion.……..... 133

VIII CONCLUSIONS…….. 138

Conclusion……..... 138
Future work…….. 142
Minimal hammerhead……... 142
The extended hammerhead……... 143
Paramagnetic probes……. 144
Metal ion binding motifs……... 144

REFERENCES……. 146

APPENDIX…….. 154

VITA……. 171

LIST OF FIGURES

FIGURE		Page
1-1	The primary structure of RNA…….	2
1-2	Watson-Crick base pairing found in RNA molecules……..	3
1-3	Structural motifs found in the secondary structure of RNA molecules…	5
1-4	Examples of type of metal ion interactions with RNA…….	7
1-5	Reaction mechanism of the cleavage of the phosphodiester bond…….....	10
1-6	Representation of the rolling circle virus replication……	12
1-7	Location of the hammerhead in the genome sequence of the sTRSV…..	13
1-8	Secondary structure of the hammerhead ribozyme..……	14
1-9	Crystal structure of the hammerhead ribozyme……	15
1-10	Folding pathway of the hammerhead ribozyme……	16
2-1	Phosphorothioate substitution of non-bridging oxygen atom……..	21
2-2	EPR energy-level splitting diagram for a Mn^{2+} ion…..……	24
2-3	Room temperature Mn^{2+} EPR spectra comparison……...	26
2-4	ESEEM pulse sequence and time-domain data…..……..	29
2-5	Thermal denaturation of a RNA duplex strand…….	31
2-6	The X-ray absorption edge……	35
2-7	Backscattering of electron producing the EXAFS signal…….	37
3-1	Hammerhead ribozyme construct…….	41
3-2	Crystal structure of the hammerhead ribozyme with a Mn ion at the A9/G10.1 site……	42
3-3	Mn EPR spectra comparison…….	45
3-4	Comparison of ESEEM results obtained for the hammerhead ribozyme..	47

FIGURE		Page
3-5	Field swept echo-detected EPR spectrum of Mn-hammerhead in D_2O…	48
3-6	Hydration determination for Mn^{2+} in the hammerhead high affinity site……..…	50
3-7	Model of the A9/G10.1 site based on EPR results and X-ray cystrallography……..	51
4-1	Crystal structure of the hammerhead ribozyme with Mg ions……...	56
4-2	RNA strands used for EPR power saturation study……..	58
4-3	Room temperature Mn^{2+} EPR binding isotherms…….	60
4-4	Mn concentration dependence on the melting temperature of the 13mer duplex……	61
4-5	Mn EPR spectra of 1:1 metal:RNA complexes…….	63
4-6	Mn^{2+} EPR power saturation plots for the RNA molecules and buffer….	65
5-1	Comparison of various ratios of Mn^{2+} to hammerhead RNA……	74
5-2	Mn^{2+} EPR spectrum of series of mimics for metal-RNA interactions….	75
5-3	Coordination of Mn^{2+} to small complexes……..……..	77
5-4	RT Mn^{2+} EPR titration of LiCl in methanol……	79
5-5	Mn^{2+} EPR spectra comparison……..	80
5-6	Ratios of allowed hyperfine lines from various Mn^{2+} samples…….	82
5-7	Simulation of the Mn^{2+} high affinity hammerhead EPR spectrum……...	85
5-8	Simulation of the Mn^{2+} buffer EPR spectrum……..	86
6-1	Mn EXAFS data and fits for the hammerhead ribozyme high affinity site……	91
6-2	Proposed models for the Mn-A9 sulfur interaction based on previous EXAFS results……..	92
6-3	Crystal structure of [MnGMP]…….	94

FIGURE Page

6-4 Mn EXAFS results for GMP complex……. 95

6-5 Crystal structure of the $[MnP_4O_{16}]^{6-}$ model complex……..... 97

6-6 Mn EXAFS results for phosphate complex…….. 98

6-7 EXAFS results for Mn-ATP(γ)S and Rp S hammerhead……. 101

6-8 Cd^{2+} EXAFS of wild type and phosphorothioate substituted hammerhead…….. 102

6-9 Molecular models of the hammerhead A9 site with Mn ion…… 105

6-10 Molecular models of the hammerhead A9 site with Cd ion…….. 109

7-1 Examples of mismatched RNA bases…… 113

7-2 The G-A metal ion-binding motif……. 115

7-3 Secondary structure of RNA sequences containing internal loops……... 118

7-4 Melt profiles of RNA sequences used in loop study……. 121

7-5 Example of melt profile fit for the hairpin sequence…….…… 122

7-6 T_m values as a function of added metal ions…….. 125

7-7 RT EPR binding isotherms for loop-containing RNA molecules……. 130

7-8 CD spectra of loop containing RNA molecules…… 132

7-9 CD spectra with addition of 1 mM Mn^{2+} ions……... 134

A-1 Catalytic activity of dG10.1 modified hammerhead ribozyme……. 167

A-2 EPR simulations and parameters…….. 168

A-3 Melt fits for GA containing hairpin sequences……. 169

A-4 Melt fits for UU containing hairpin sequences……. 170

LIST OF TABLES

TABLE		Page
4-1	Mn^{2+} power saturation values……...	66
5-1	EPR simulation parameters of the hammerhead and buffer spectra……..	87
6-1	Mn EXAFS fit results……	96
6-2	Cd EXAFS fit results…….	103
6-3	Structural information for Mn^{2+} model complexes at the A9/10.1 site….	107
6-4	Structural information for Cd^{2+} model complexes at the A9/10.1 site…..	110
7-1	Thermodynamic parameters derived from UV thermal denaturation of RNA sequence containing internal loops……..	123
7-2	Apparent affinity constants obtained from metal ion dependence of melt profile……	128
7-3	Binding values of Mn^{2+} ion obtained from RT EPR……..…	131
A-1	Crystal data and structure refinement for Mn-GMP…….	154
A-2	Atomic coordinates for Mn-GMP…….	155
A-3	Bond lengths and angles for Mn-GMP…….	156
A-4	Anisotropic displacement parameters for Mn-GMP…….	159
A-5	Hydrogen coordinates and isotropic displacement for Mn-GMP…….	160
A-6	Crystal data and structure refinement for Mn-phosphate…….	161
A-7	Atomic coordinates for Mn-phosphate…….	162
A-8	Bond lengths and angles for Mn-phosphate…….	163
A-9	Anisotropic displacement parameters for Mn-phosphate…….	165
A-10	Hydrogen coordinates and isotropic displacement for Mn-phosphate….	166

CHAPTER I

INTRODUCTION

Nucleic acids

Nucleic acids are essential for storing and transmitting genetic information in every cell and organism. The two types of nucleic acids are deoxyribonucleic acid (DNA), which stores genetic information and ribonucleic acid (RNA), which among other functions transmits this information.[1] Nucleic acids consist of three main parts, the negatively charged phosphate backbone, a five-member ribose sugar ring, and a purine or a pyrimidine base.[2] In RNA the bases are guanine, adenine, uracil, and cytosine, (Figure 1-1) while in DNA thymine is substituted for uracil. DNA and RNA also differ in the sugar where for RNA there is a hydroxy group at the 2' position on the ribose sugar and DNA has a hydrogen at the 2' position. The phosphate group has two non-bridging oxygen atoms and links the sugars to one another through a phosphodiester bond at the 3' end of one sugar to the 5' end of the next sugar.

The secondary structure of RNA is dominated by base stacking and Watson-Crick base pairings of guanine with cytosine, and adenosine with uracil. The G-C base pairing consists of 3 hydrogen bonds, while the A-U pairing has only 2 hydrogen bonds (shown in Figure 1-2). The G-C base pairs also have a greater ΔH value compared to the A-U pairing that makes a G-C rich strand thermodynamically more stable than an A-U rich strand.[1] The stacking of base pairs occurs when adjacent bases partial overlap each other and this stabilizes the RNA structure by burying the hydrophobic bases.

Nucleic acids duplexes contain numerous alternating base paired regions that

---

This dissertation follows the style of *Journal of American Chemical Society.*

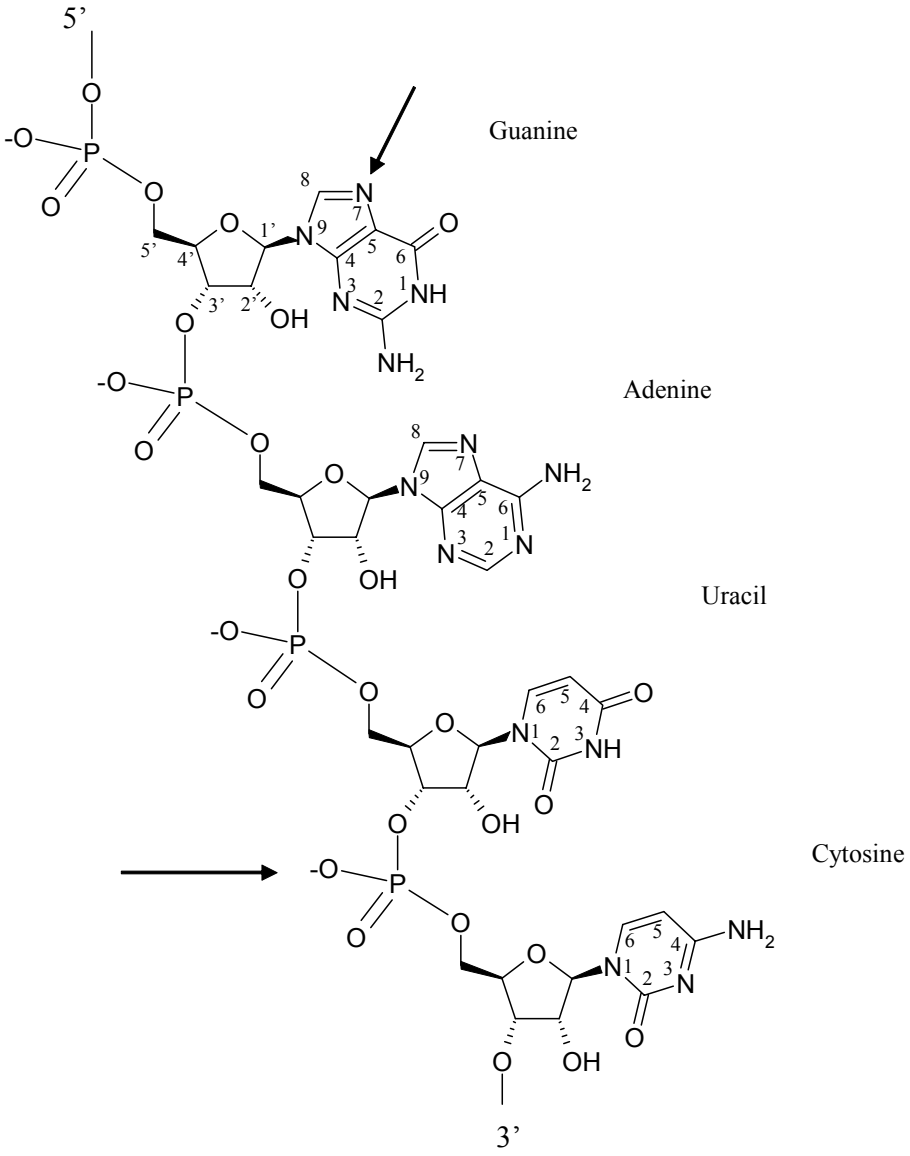

Figure 1-1: The primary structure of RNA. Each nucleotide consists of a nitrogenous base, a ribose sugar, and a phosphate group. Possible metal ion interactions are noted by the arrows and include the phosphate oxygen and the N7 of guanine.

form a spiraling helix. Cellular RNA is usually a long single stranded complex that is folded in compact tertiary structure. RNA-RNA and RNA-DNA containing duplexes are

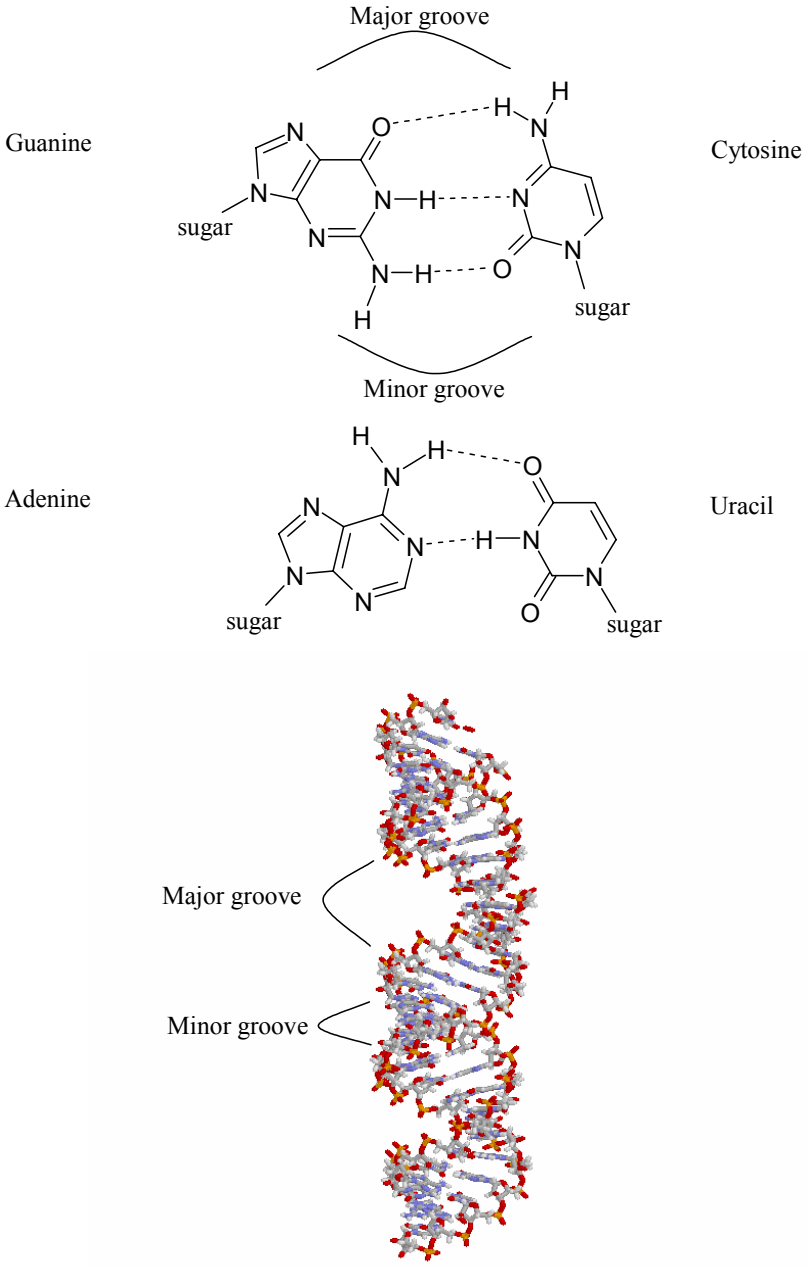

Figure 1-2: Watson-Crick base pairing found in RNA molecules. The G-C base pair has 3 H-bonds and the A-U base pair has 2 H-bonds. The crystal structure of an RNA duplex (PDB code 1QC0) shows the location of the major and minor grooves.

readily found in the A-form helix conformation, while DNA-DNA duplexes are normally found in the B-form.[2] A double stranded RNA helix in A-form has a right-handed helix that turns every 11 bases and has a deep and narrow major groove. The major groove is

where the bases face while the minor groove is the side the sugars are located (see Figure 1-2). The presence of the 2'-OH group on ribose alters the sugar puckering to favor C3'-endo while the deoxyribose has C2'-endo puckering.[2] In RNA there is a steric hindrance between the 2'-OH group and the phosphate group that affects the sugar puckering and alters the overall structure of the RNA helix making it different from the DNA helix.

The central dogma of biochemistry states that from a protein-encoding DNA sequence a complementary mRNA strand is transcribed. This mRNA strand contains codons, or base triplets, corresponding to specific amino acids that are used to translate the RNA sequence into the desired protein. In the ribosome, tRNA molecules transport the amino acids to be synthesized into the protein. In addition to m and tRNAs, RNA is involved in the production of proteins (ribosomal or rRNA), but also has other functions in signal recognition particles (SRP), small nuclear RNA (SnRNA), and RNA interference (RNAi) as well many other cellular processes.[1]

RNA folding

RNA molecules undergo a hierarchal folding pathway with the secondary structure forming first followed by the tertiary structure. RNA strands readily adopt complicated secondary structures with several common structural elements. Some common structural elements found in RNA molecules are hairpins, internal loops, bulges, and three- and four-way junctions (shown in Figure 1-3). A dominant feature found in these elements is mismatched base pairs or unpaired nucleotides. Some common mismatches found in numerous RNA molecules are G-U and G-A mismatches that do not have standard Watson-Crick pairings, but have their own unique H-bonding interactions that provide stability (see figure on page 123).[3] After the secondary structure has formed,

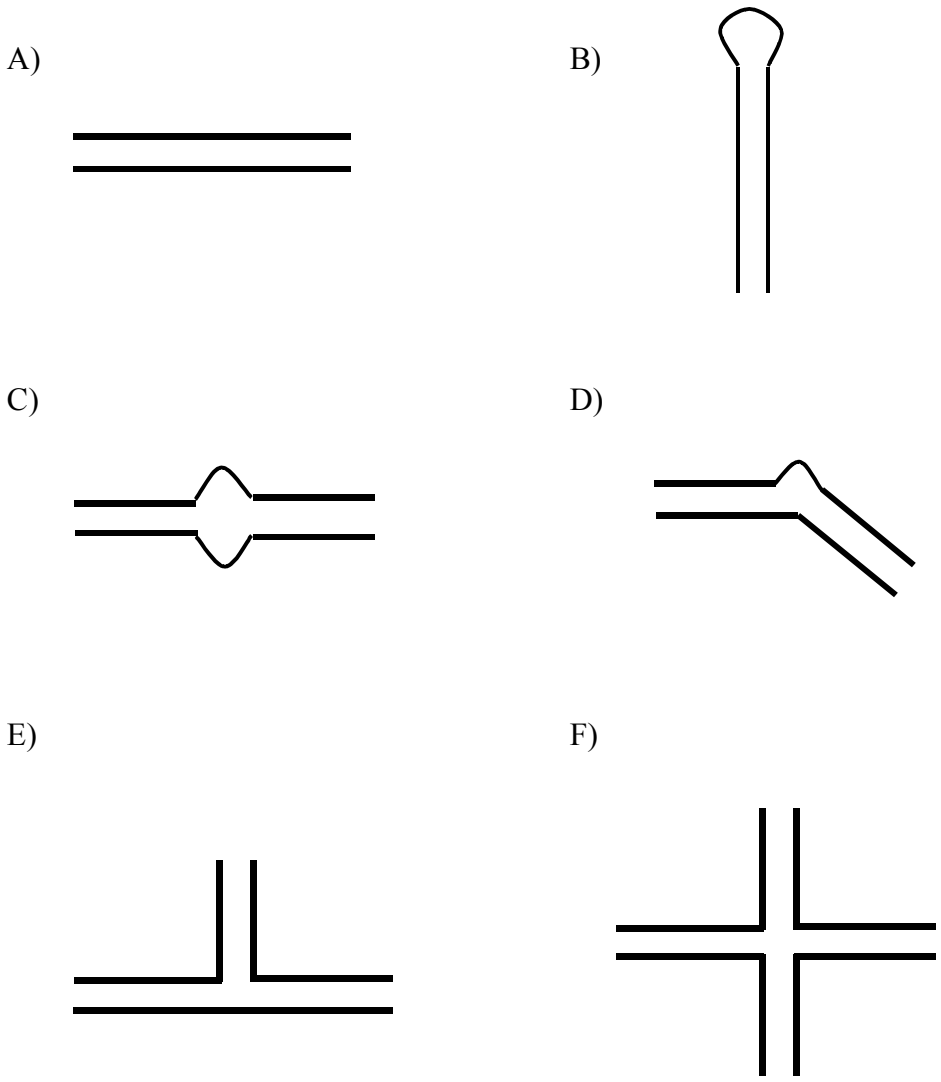

Figure 1-3: Structural motifs found in the secondary structure of RNA molecules. A) duplex, B) hairpin, C) internal loop, D) bulge, E) three-way junction, and F) fourwayjunction.

the RNA then proceeds to fold around specific regions and form defined tertiary interactions that give the RNA molecule its distinctive shape. Some of these features found between regions of the RNA that aid in forming the overall tertiary structure of the molecule are the tetraloop and tetraloop receptors, ribose zippers and kissing hairpins.[4]

These elements consist of residues from one region having H-bonding interactions with residues of another region that help stabilize a compact tertiary structure. One of the most recognizable and extensively studied folded RNA molecule is the yeast $tRNA^{phe}$, which has a distinctive L shape structure as observed in crystal structures.[5,6] Larger RNA molecules, such as the group I intron, have a compact globular form reminiscent of a folded protein of similar size.[7]

Metal ion interactions

Since the phosphate group of RNA and DNA carries a negative charge at neutral pH (phosphate oxygen $pK_a \sim 1$-2), nucleic acids are polyelectrolytes that require positive ions for charge neutralization. This screening of the negative charge can be fulfilled by either mono- or divalent cations. Cation-nucleic acid interactions have been described by three main categories.[8,9] The first is general charge screening of the negative phosphate groups from a "sea" of mono- or divalent cations in a non-specific distant interaction (Figure 1-4A). These interactions are typically through several water molecules and are not specific in the sense that the cations are constantly moving and exchanging positions, but the overall charge remains virtually constant. The second category is outer-sphere coordination where a ligand, such as H_2O, bound to the metal ion is shared with a functional group on the RNA molecule (Figure 1-4B). The third is inner-sphere coordination where the metal ion loses a H_2O ligand and binds directly to the RNA molecule (Figure 1-4C). Examples of specific coordination sites are the phosphate oxygens, and the O6 and N7 positions of guanine residues.

The metal cations that are commonly thought to interact with and stabilize the RNA molecules under physiological conditions are Mg^{2+}, Na^+ and K^+ ions. Sodium or

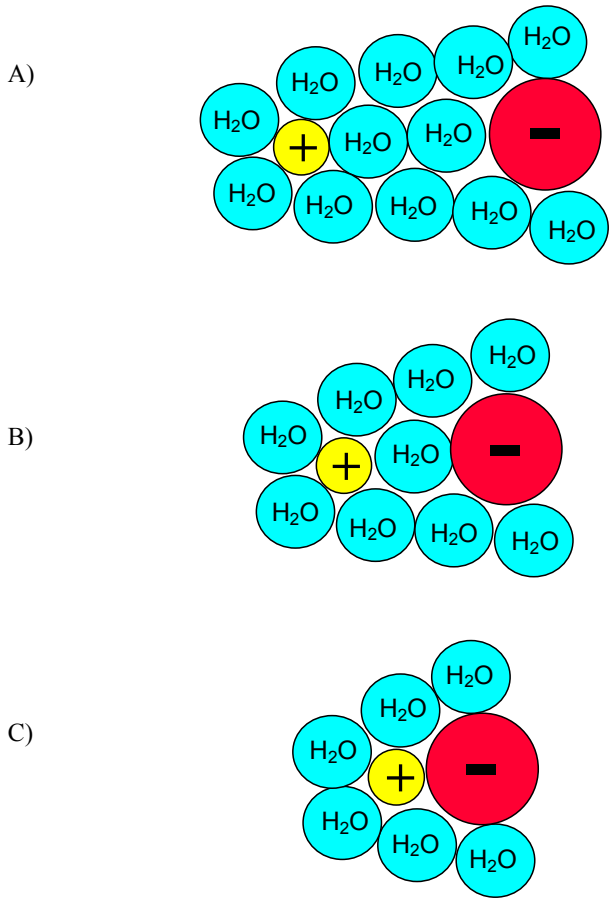

Figure 1-4: Examples of type of metal ion interactions with RNA. A) Diffuse ion interaction, B) outer-sphere interaction, C) inner-sphere interaction. Adapted from Misra and Draper.[8]

potassium ions are quite abundant in living systems at a concentration of approximately 150 mM and are quite efficient at screening the negative charge. Transition metal ions have been observed coordinated to RNA molecules in crystal structures. The main difference between transition metal ions is the ability to directly bond more readily to the RNA in comparison with Mg^{2+} and Na^{+} or K^{+} ions.

The driving force for a metal ion interaction with the RNA molecule is a combination of the energetic benefit versus penalty of direct coordination. To coordinate

directly at a site in the RNA, a metal ion must overcome the high energetic cost of losing one or more H_2O ligands. Also directly coordinating a cation at a specific site reduces the concentration of any proximal diffusely bound cations, reducing the local positive charge by repulsion of the like charges. Keeping these considerations in mind, a site-specific metal ion bound in an RNA molecule must have a high driving force to occupy a specific site.[10] Folding of the RNA molecule creates pockets of high negative potential that are ideal locations for site-specific metal ion binding that compensates for the negative charge of the RNA.

Metal ions as spectroscopic probes of RNA structure

Although Mg^{2+} and Na^{+}/K^{+} are typically involved in metal-RNA interactions under physiological conditions, there are a limited number of spectroscopic methods available to directly study their interaction with an RNA molecule. To alleviate this problem spectroscopically active metal ions can be used as substitutes for Mg^{2+} ions to probe metal-RNA interactions. The luminescence properties of the lanthanide ions Eu^{3+} and Tb^{3+} have been used to determine cation binding sites in several RNA structures.[11, 12, 13, 14] The ligand exchange-inert complex $Co(NH_2)_6^{3+}$ has been used to mimic $Mg(H_2O)_6^{2+}$ outer-sphere interactions in order to determine coordination sites using NMR spectroscopy.[15,16] Placing a sulfur substitution on the phosphate backbone weakens Mg^{2+} ion binding to that site, but enhances coordination of thiophilic Cd^{2+} ions.[17] The paramagnetic Mn^{2+} ion has been used in EPR studies[18-22] as well as for NMR line broadening experiments on several RNA molecules.[15,23]

Ribozymes

Previously, only proteins were believed to be capable of carrying out enzymatic reactions within a cell. The discovery of a class of RNA molecules with the ability to perform unique catalytic reactions in the absence of any proteins was a major milestone in biochemical studies.[24,25] In 1981, Cech discovered that the mRNA precursor of the *Tetrahymena* group I intron was capable of cleaving a phosphodiester bond.[26] Soon after, the RNA component of ribonuclease P (RNaseP) was discovered to be responsible for phosphodiester bond cleavage.[27] These catalytic RNA molecules were dubbed "ribozymes" or RNA enzymes. More recently, it has been discovered that the RNA component of nucleoprotein complexes may be responsible for the chemical functions. The most important such finding is that the ribosome, the protein/RNA complex that synthesizes polypeptides from amino acids, is actually a ribozyme.

The simplest ribozymes perform site-specific cleavage and ligation reactions of RNA involved with replication intermediates and are called the nucleolytic ribozymes. The four types of this ribozyme are the hammerhead found in plant viroids, the hairpin found in plant viroids, the Varkud satellite (VS) found in the mitochondria of *Neurospora*, and the hepatitis delta virus (HDV) found in human hepatitis B virus.[25] Each of these four has an unrelated structure, but in each case performs the same reaction. The cleavage reaction of the nucleolytic ribozymes proceeds by an in-line attack of the scissile phosphate by a deprotonated 2'-OH forming a five coordinate trigonal bypyrimidal transition state (Figure 1-5). The product is a 5'-OH and a 2',3'-cyclic phosphate with inversion of the phosphate center consistent with a S_N2 reaction mechanism. The group I and group II introns, which are involved in the self-splicing of

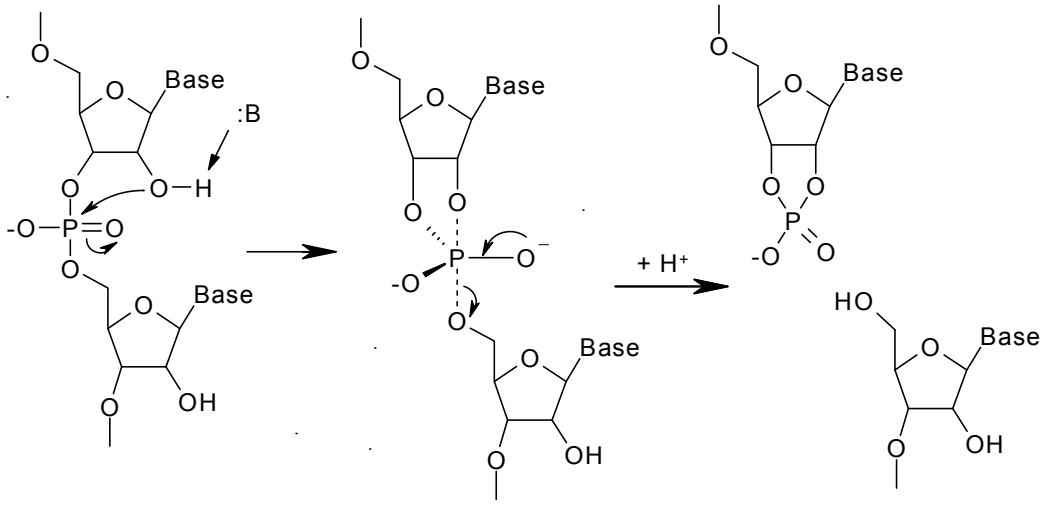

Figure 1-5: Reaction mechanism of the cleavage of the phosphodiester bond. A nucleophilic attack of the 2'-OH by a base abstracts a proton. The oxygen attacks the phosphate group forming a trigonal bipyramidal transition state. The products are 2',3'-cyclic phosphate and 5'-OH RNA strands.

introns, differ from the cleavage reaction of the nucleolytic ribozymes. Instead of using the adjacent 2'-OH as a nucleophile, the group I intron uses the 3'-OH of an exogenous guanosine residue and the group II intron uses a 2'-OH from a distant nucleotide as the nucleophile.

The typical rates measured for ribozymes have been in the range of ~0.1-1 min^{-1}, which is a rate enhancement of 10^5-10^6 for the base-catalyzed reaction of the phosphodiester bond of dinucleotides.[25] Three possible methods by which ribozymes achieve this rate enhancement are general acid-base catalysis, charge stabilization, and conformational effects. Deprotonation of the 2'-OH group by a general base produces a

stronger nucleophile to more readily attack the phosphate group while protonation aids in the stabilizing of the leaving group. The negatively charged transition state may be stabilized by the presence of either monovalent or divalent cations. To create the 5-coordinate transition state, the local conformation of the RNA molecule must rearrange itself to align the 2'-OH group for an in-line attack of the phosphate.[7,28]

As with all RNA molecules ribozymes require the presence of cations to fold into their tertiary structure and consequently the active form. The metal ions, however, may also have a direct role in catalysis. The metal ion could act, as a hydroxo species, to deprotonate the 2'-OH, or may help in stabilizing the negative charge of the penta-coordinated phosphorous transition state. Apart from the possible direct involvement of metal ions in the catalytic reaction, nucleobases may act as general acid-bases in the reaction. The HDV is a prime example of this type of reaction where a conserved cytosine residue with an apparent elevated pK_a is essential for catalytic activity.[25]

The hammerhead ribozyme

The hammerhead is a nucleolytic ribozyme found in several plant viruses and is one of the most studied and well-characterized ribozyme.[29] The hammerhead performs a site-specific phosphodiester bond cleavage reaction to produce a gene copy as part of rolling circle replication[29] as shown in Figure 1-6. To replicate the plus strand, the viroid RNA uses either the host or a viral encoded RNA polymerase to create a long RNA strand containing the minus strand. This new strand undergoes self-cleavage by the hammerhead ribozyme motif to create a new minus strand and is then circularized. This process is repeated using the newly created minus strand to replicate the plus strand. The hammerhead ribozyme sequence used in the experiments here and in many studies is a

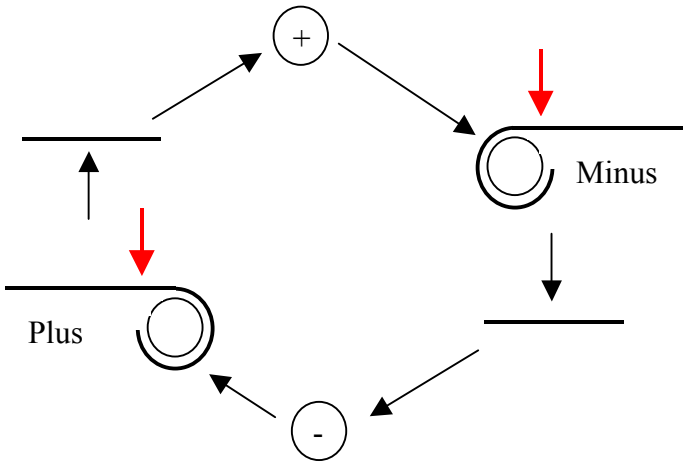

Figure 1-6: Representation of the rolling circle virus replication. The plus and minus strands are created by RNA polymerase encoded from either the virus or the host. The red arrows indicate sites of self-cleavage performed by ribozyme sequence to create single stranded RNA. The single strand is then circularized to create of copy of the genome. Adapted from Symons.[29]

truncated motif that originates from the plus strand of a satellite of the tobacco ringspot virus (sTRSV) (Figure 1-7). All though it has been extensively studied there is much still unknown about exactly how the hammerhead ribozyme functions.

The hammerhead ribozyme motif of Figure 1-8 is separated into an enzyme and substrate strand, which together forms a three-way helix junction structure. The center of the junction contains several non-Watson Crick residues referred as the conserved core, which has been shown to be essential for catalytic activity (Figure 1-8).[30-32] Even slight modifications of the nucleotides inside the conserved core can reduce or even completely abolish catalytic activity. One site that is very sensitive to alterations is the A9/G10.1 site where placing a phosphorothioate modification 5' to A9 greatly reduces the Mg^{2+} dependent catalytic activity[33] and the removal of the guanine base also has an inhibitory

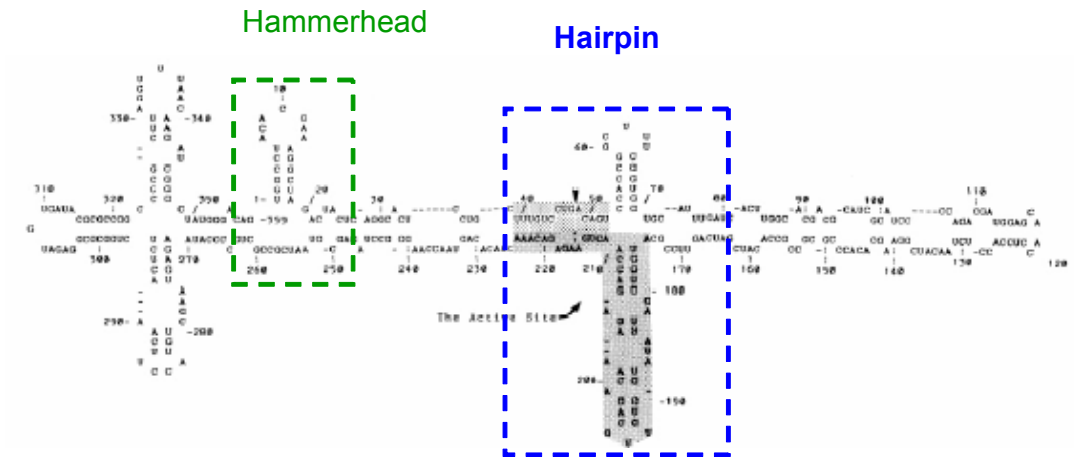

Figure 1-7: Location of the hammerhead in the genome sequence of the sTRSV. The green box shows the location of the hammerhead motif and the blue box shows the location of the hairpin motif.

effect.[34] Replacing the cleavage site C17 with a G residue greatly decreases activity.[35] The hammerhead has been shown to be active under moderate concentrations of divalent ions (mM range), such as Mg^{2+}, Mn^{2+}, and Cd^{2+}, as well as high concentrations of monovalent ions (M range), including Li^{+} and NH_4^{+}.[36,37] Similar effect on the catalytic activity in both monovalents ions and divalent ions was observed for as series of modifications to the hammerhead. This implies that the role both types of ions have on facilitating catalytic activity is mainly charge neutralization of the phosphate backbone.[38]

Early crystal structures showed the hammerhead ribozyme to have a unique folded structure that resembles a Y shape.[39] In the crystal structure stems II and III are coaxially stacked with stem I nearly parallel to stem II (see Figure 1-9). The conserved core shows two distinctive H-bonding networks called domain 1 and domain 2. Domain 1 consists of residues C3U4G5A6 and forms a uridine turn of the form UNR, which creates a sharp turn in the backbone. Domain 2 consists of U7G8A9 forming mismatches

with G12A13A14 and includes two sheared G-A mismatches and a non-canonical A-U pairing. The coaxial alignment between stems II and III is formed by the residues A13 and A14 of the core stacking on A15 of stem III.

The early crystal structures of the hammerhead were obtained using a DNA substrate strand or a 2'-methoxy modification and hence were not active, leading to concern if the hammerhead was in the correct folded form.[40,41] The crystal structure of an unmodified hammerhead ribozyme with an RNA substrate strand was similar to that

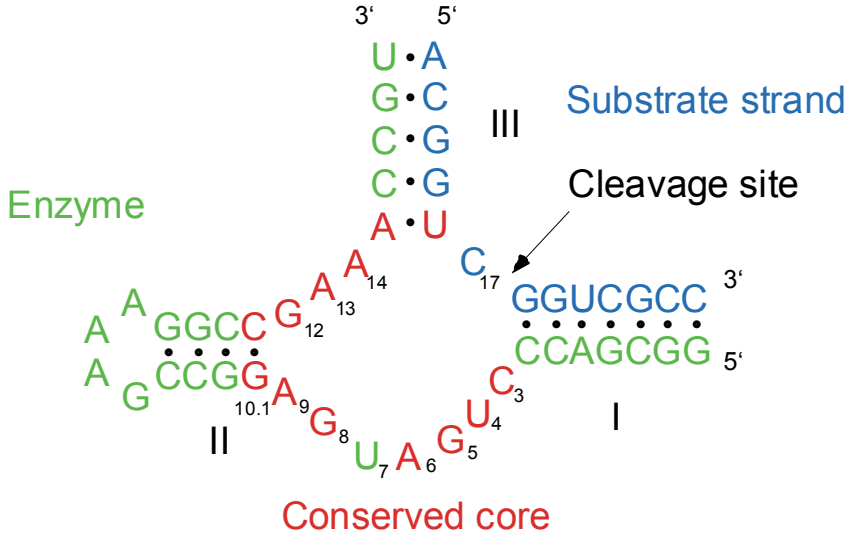

Figure 1-8: Secondary structure of the hammerhead ribozyme. The green strand is the enzyme strand, the blue strand is the substrate strand, and the nucleotides in red are part of the conserved core, which is essential for activity. The arrow denotes the site of site-specific cleavage.

observed of the modified sequences. This structure, however, did not have the 2'-OH of the cleavage site positioned correctly for an in-line attack of the scissile phosphate group in the ground state.[42] Soaking the crystal in divalent ions led to cleavage of the substrate strand and a freeze quenched intermediate of this crystal showed rearrangement around the cleavage site bringing it closer to the in-line attack geometry.[42,43]

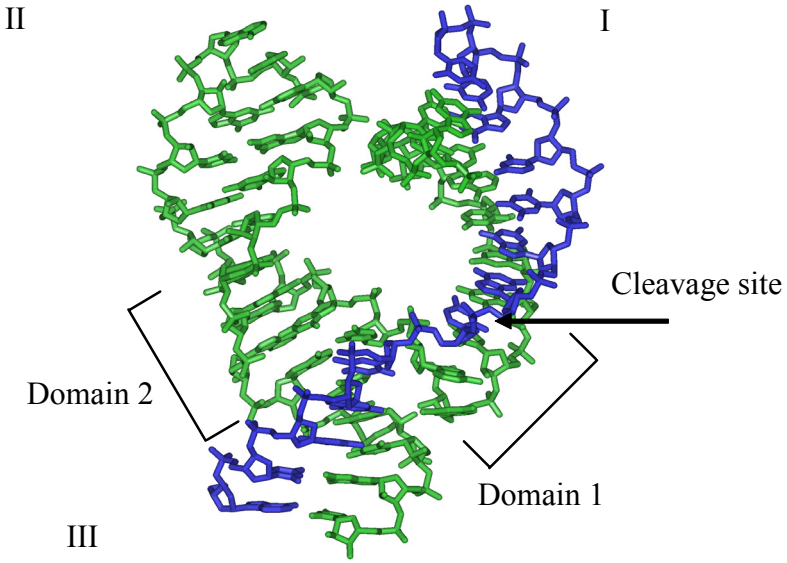

Figure 1-9: Crystal structure of the hammerhead ribozyme. The green is the enzyme strand, and the blue is the substrate strand. The arrow indicates the cleavage site and domain 1 and 2 are noted. PDB 1HMH.

Crystal structures of the hammerhead soaked in solutions containing various divalent metal ions have shown evidence for several potential metal ion-binding sites. Several areas where metal ions have been located in multiple X-ray structures are at the A9/G10.1 site, near the cleavage site, and at the G5 position. The A9/G10.1 binding site contains a metal ion coordinated to the N7 position of G10.1 and the Rp oxygen of the phosphate group from A9.[44]

Under solution conditions it has been found that the tertiary structure of the hammerhead is highly dependent on the ionic conditions. Pardi and co-workers have used residual dipolar couplings to determine that under low salt concentrations (100 mM Na^+) the hammerhead is in an extended conformation that is not observed in the crystal structure.[45] Lilley and coworkers have used fluorescence resonance energy transfer (FRET) and ^{19}F NMR spectroscopy to examine the folding pathway of the hammerhead upon addition of divalent Mg^{2+} ions.[30, 31, 46-48] A two state folding pathway was

predicted, starting from the extended conformation with the three stems far apart from each other as depicted in Figure 1-10. The first folding step occurs with the addition of low Mg^{2+} (less than 500 μM) where domain 2 of the conserved core forms and stems II and III are coaxially stacked. The second transition occurs at a higher Mg^{2+} concentrations of 1-15 mM where stem I lines up with stem II and domain 1 forms resulting in a tertiary structure consistent with that observed in the crystal structure. The metal ions observed at the A9 and G5 sites in the crystal structures may be involved in the formation of domain 2 and domain 1, respectively, during the folding pathway.

Probably the most important metal ion site in the hammerhead is the A9/G10.1 location. Phosphorothioate modifications at the A9 site reduce activity in the presence of

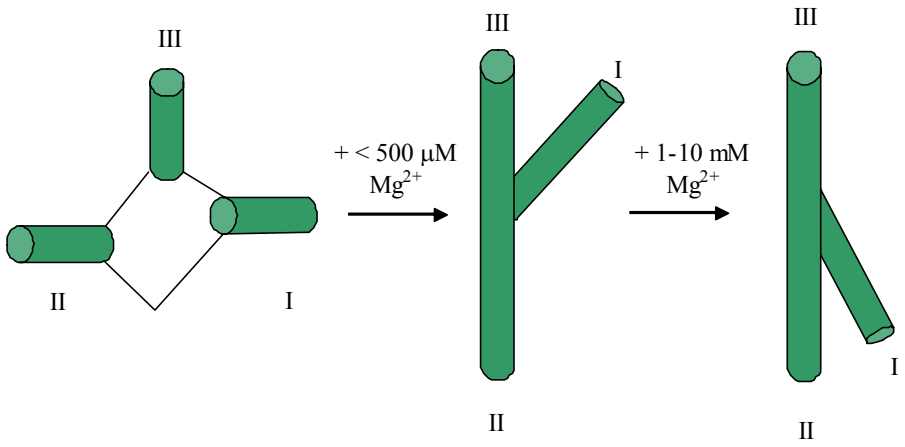

Figure 1-10: Folding pathway of the hammerhead ribozyme. Upon addition of less than 500 μM Mg^{2+} ions stems II and III become coaxially stacked and domain 2 is formed. When 1-10 mM Mg^{2+} ions are added domain 1 is formed and the hammerhead is fully folded.

Mg^{2+} ions, but activity can be rescued with the addition of thiophilic Cd^{2+} ions.[49] The disturbance in activity from changes at this site is remarkable considering it is nearly 20

Å from the cleavage site based on the crystal structures. Herschlag and co-workers have proposed the direct involvement of the A9/G10.1 metal ion in the cleavage reaction.[49] In this model the hammerhead undergoes a significant structural rearrangement and the metal ion at the A9/G10.1 site also binds to the scissile phosphate. From examination of the crystal structure, however, modeling of this conformational change produces a severe disruption to the conserved core and the helices as well making this model controversial.[50]

Room temperature Mn^{2+} EPR (electron paramagnetic resonance) studies have been performed to understand the metal ion coordination properties of the hammerhead ribozyme and their link to catalytic activity.[19,51] The binding isotherms obtained showed two classes of metal binding sites, in 0.1 M NaCl: a tight set of 3-4 metal ions with an apparent K_d of 3.3 ± 2.7 μM and a set of weaker sites with ~ 7 metal ions at a much higher K_d of 122 ± 48 μM.[52] Correlation of the activity to the number of ions bound showed that maximal cleavage was obtained at a concentration of Mn^{2+} ions where all the metal sites are populated. Elevated Na^+ ion concentrations compete for metal binding sites and at 1 M NaCl it was observed that a single Mn^{2+} ion binds to the hammerhead with an apparent K_d of less than 10 μM.[19,22] At concentrations of ~ 300 μM, a weaker class of sites is evident with the Mn^{2+} ions effectively compete away the high Na^+ concentration.

The relative affinities for a series of metal ions to the hammerhead, in comparison with Mn^{2+} ions, have been obtained by a binding competition study.[51] Increasing the concentration of the competing ion at a fixed amount of Mn^{2+} will allow a relative affinity to be measured through observing the displacement of Mn^{2+} ions. It was found

that the relative affinities for metal ions to the hammerhead are $Mn^{2+} \sim Co^{2+} \sim Zn^{2+} > Cd^{2+} >> Mg^{2+}$, which follows a similar trend for maximum rate of cleavage of $Mn^{2+} > Co^{2+} > Cd^{2+} > Mg^{2+}$.

To further explore the high affinity Mn^{2+} site in the hammerhead at 1 M NaCl, low temperature EPR spectroscopy has been used.[21] The EPR spectrum for a 1:1 Mn^{2+} to hammerhead sample shows a slight, but reproducible, difference in the lineshape when compared to Mn^{2+} in buffer. This difference is most noticeable on the 6th and 5th lines of the spectrum and has been linked to a specific coordination environment for the Mn^{2+} ion in the presence of the hammerhead ribozyme. Further examination of this EPR signal is described in Chapter V of this thesis. The high affinity Mn^{2+} site has also been investigated by advanced EPR techniques, such as ENDOR (electron nuclear double resonance) and ESEEM (electron spin echo envelope modulation) spectroscopy. These techniques are useful in identifying and characterizing metal ligands that have a nuclear spin and that are not observed by conventional EPR techniques. Results from these studies showed ^{1}H interactions from H_2O ligands, coordination to a phosphate group, and the presence of a nitrogen ligand from a guanine residue.[20,21] These data suggested a possible coordination site at the A9/G10.1 site in the hammerhead but were inconclusive in determining the exact location of the high affinity metal ion site.

Pardi and co-workers using ^{31}P NMR spectroscopy have determined a location of a metal ion-binding site in the hammerhead at the A13 residue with an apparent K_d of 250-750 μM.[23] Titrating Mg^{2+} ions into the sample, they monitored the chemical shift of the A13 phosphorous atom and fit the data to obtain a K_d value. A metal ion has not been previously observed bound at this site in any of the crystal structures. Direct

identification and quantification of aqua ligands by ESEEM spectroscopy are described in Chapter III of this thesis.

^{31}P NMR has also been used to study metal ion binding to phosphorothioate modifications at the A9 and the scissile phosphate of the hammerhead.[53] Studying both the Rp and Sp isomers of the sulfur modification at the A9 site, the chemical shift of the modified phosphate was monitored with the addition of Cd^{2+} ions and it was found that the Cd^{2+} ion binds to the sulfur of both isomers. By contrast, when the sulfur modification was placed at the cleavage site, only a slight change in the chemical shift was observed. To further understand metal coordination at the A9 site EXAFS of the hammerhead and model complexes are described in Chapter VI.

Metal ion interactions with RNA molecules are of great importance to correctly fold an RNA molecule. Characterizing the difference between site-specific and non-specific metal-RNA interactions can provide an understanding of the exact role a metal ion has when coordinated to an RNA molecule. To achieve this goal, extensive spectroscopic studies have been conducted in order to characterize metal ion coordination properties to RNA molecules and appropriate model complexes.

CHAPTER II

MATERIALS AND METHODS

Preparation of RNA strands

All RNA strands used in these experiments were obtained commercially and were chemically synthesized using phosphoroamidite methods from either Dharmacon, Inc. (Lafayette, CO) or Xeragon, Inc. (Qiagen). The hammerhead ribozyme construct used in these studies is in Figure 1-8 and consisted of two RNA strands, a 34nt RNA enzyme strand (ε = 331,300) and a 13nt RNA substrate strand (ε = 119,900). The substrate contained a 2'-OCH_3 at the C17 position (13nt OMet) to prevent cleavage during metal ion binding studies, while the substrate strand with a hydroxy group was used for cleavage assays. The deoxy-modified hammerhead contained a single dG base at the 10.1 position of the enzyme strand. For site-specific ^{15}N guanine labeled studies, ^{15}N labeled dG phosphoroamidites from Spectra Stable Isotopes were purchased and used by Xeragon during the phosphoroamidite synthesis reaction of the RNA.

The RNA pellets received from Dharmacon were chemically protected at the 2'-OH with an acid labile orthoester protecting group (2' ACE®), and deprotected following the manufacturer's instructions by dissolving the RNA pellet in 400 μL of acetic acid buffer, followed by incubating at 60ºC for 30 minutes. An equal volume of formamide was added to the RNA solution, which was loaded onto 20% polyacrylamide gels for purification. The RNA bands were excised from the gel under visualization by UV shadowing, electroeluted and dialyzed against 5 mM TEA, 100 mM NaCl, pH 7.8 buffer at 4ºC for at least 48 hours with 5 buffer changes. Samples were then concentrated using YM-3000 centricon tubes (Millipore), ethanol precipitated by 1 mL ethanol and 20-30 μL

of 3 M sodium acetate was added to aid in precipitation and stored at –30ºC overnight. The RNA pellet was then spun down for 30 minutes, the supernatant was collected and the pellet was dried under vacuum. The RNA pellets were then resuspended in 5 mM TEA, pH 7.8 autoclaved buffers containing the desired concentration of NaCl or $NaNO_3$. Depending on the experiment, typical salt concentrations used were 100 mM NaCl, 1 M NaCl, or 1 M $NaNO_3$. Concentrations were determined by monitoring the UV/Vis absorbance at 260 nm on a Cary 300 Bio UV/Vis spectrometer (Varian).

Phosphorothioate substituted RNA

A phosphorothioate substitution replaces one of the non-bridging oxygen atoms of the phosphate backbone with a sulfur atom. This modification was done during a chemical synthesis stage where elemental sulfur is used to oxidize the phosphoroamidite and yield a mixture of diastereomers (see Figure 2-1). A phosphorothioate substitution

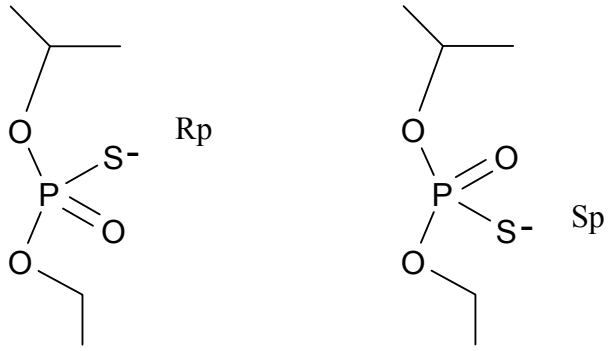

Figure 2-1: Phosphorothioate substitution of non-bridging oxygen atom. During chemical synthesis of the RNA strand a mixture of Rp and Sp sulfur substitutions are produced.

was placed at the A9 phosphate to study Cd^{2+} and Mn^{2+} ion binding. The isomers were separated by HPLC with a reverse phase C-18 column (Amersham Bioscience) with an 0.1 M ammonium acetate (Buffer A) and 80 % acetonitrile/20 % Buffer A (Buffer B). A

3-part gradient was used, 0-5 % B over 8 column volumes (CV), 5-12 % over 90 CV, 12-50 % over 1 CV. The RNA separates into two peaks, with the Rp isomer eluting first[53] at ~ 7 % B and Sp isomer at ~ 7.3 % B, and the RNA was collected in 3-4 mL fractions. The collected RNA was combined and the acetonitrile was removed by rotavaping and washed repeatedly with autoclave H_2O, extensively dialyzed, and ethanol precipitated.

RNA sample preparation for low temperature EPR

Equal concentrations of 34nt enzyme strand and 13nt OMet substrate strand were added together and heated for 90 seconds at 90 ºC, then cooled on ice for 30 minutes. $MnCl_2$ was added from a freshly made stock solution prepared in deionized H_2O from a 1 M $MnCl_2$ source (Sigma). To prevent the formation of ice crystals and solute aggregation during freezing, a cryoprotectant was added to the solution. The majority of low temperature samples contained 20 % (vol/vol) ethylene glycol as the cryoprotectant which has shown not to alter the activity of the hammerhead or Mn^{2+} binding behavior.[54] Certain samples were also prepared using 0.4 M sucrose as the cryoprotectant. Samples were transferred to quartz capillary tubes (i.d. = 2.0 mm, o.d. = 2.4 mm Vitrocom) and frozen in liquid N_2. The room temperature EPR samples contained 0 - 1 mM Mn^{2+}, 10 μM RNA, in a volume of 75 μL prepared in quartz capillary tubes (1.5 i.d., 1.8 o.d. Kimble, Vineland, NJ) then placed into standard 4 mm EPR tubes.

X band EPR spectroscopy

Electron paramagnetic resonance (EPR) spectroscopy observes the absorption of microwave energy by unpaired electrons in the presence of an external magnetic field. The EPR spectrum is explained by the spin Hamiltonian shown in equation 2.1.

$$\mathcal{H} = \beta_e H \bullet g \bullet S - \beta_n H \bullet g_n \bullet I + S \bullet A \bullet I + S \bullet D \bullet S \qquad (2.1)$$

The first term is the electron Zeeman term and describes the interaction of S, the spin vector, with H, the magnetic field vector, β_e is the Bohr magnetron. For a simple spin system of S = ½, the electrons have either a spin of M_s = –½ or +½ depending on whether they are aligned with the magnetic field or against it, respectively. The second term, the nuclear Zeeman, describes the interaction of I, the nuclear spin, with the magnetic field. β_n is the nuclear Bohr magnetron. The third term is the hyperfine interaction and describes the interaction of the electron spin with the nuclear spin via A, the hyperfine coupling tensor. For ions with an S value greater than ½ (such as Mn^{2+} S = 5/2) the last term is the zero field splitting (zfs) which describes the interaction of the different spin values through D, the axial zero field splitting parameter. For an EPR spectrum with rhombic symmetry, an additional term, E, is include with the zfs parameters and has maximum value of 1/3 for E / D indicating a fully rhombic spectrum. The Hamiltonian describing the zfs term for a rhombic system is shown in equation 2.2:

$$\mathcal{H}_{zfs} = D\{S^2_z - 1/3S(S + 1)\} + E\{S^2_x - S^2_y\} \qquad (2.2)$$

The electron spin energy diagram for a Mn^{2+} ion in two different types of environment is shown in Figure 2-2. In a symmetrical environment the high spin d^5 Mn^{2+} ion has ^6A symmetry with an EPR spectrum centered at g ~ 2 with a six-line hyperfine pattern separated by 90 gauss from the interaction of the electron spin with the nuclear spin of I = 5/2 from the Mn^{2+} ion. The observed EPR signal is a superposition of all 30 allowed transitions as seen in Figure 2-2. At room temperature, an average signal is observed for all free Mn^{2+} ions while at low temperatures (4 - 20 K) the EPR spectrum can become more complicated due to the presence of forbidden transitions. The forbidden transitions come in pairs offset from the allowed EPR lines and are directly

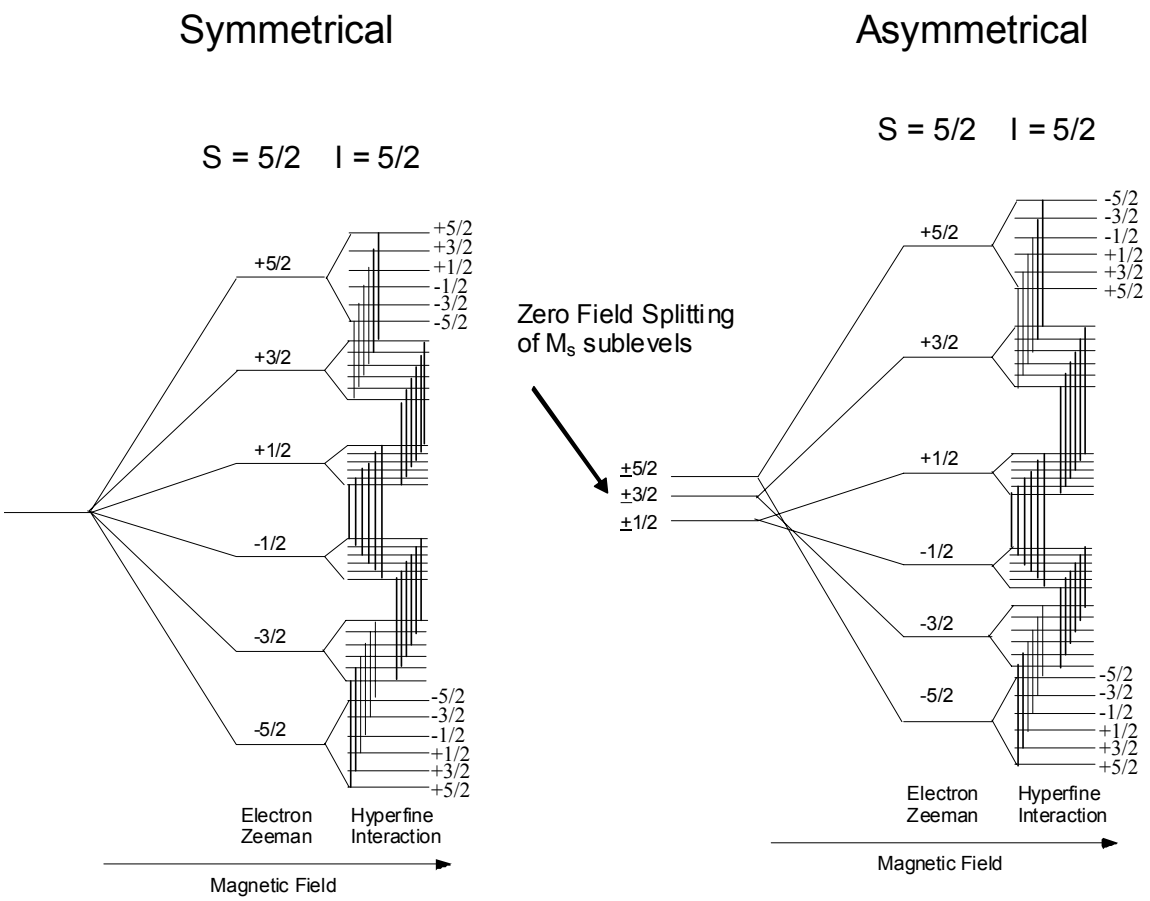

Figure 2-2: EPR energy-level splitting diagram for a Mn^{2+} ion. The left shows a Mn^{2+} ion in a symmetrical environment, the right shows the effect of Zero Field Splitting on the Mn^{2+} M_s levels when the Mn^{2+} is placed in an asymmetrical environment.

dependent on the zfs value of the Mn^{2+} ion. Changes in D and E change the positions of the forbidden transitions.[55]

EPR spectra were obtained using a Bruker EMX X-band EPR spectrometer operating at a frequency of 9.4 GHz with a standard TE_{102} rectangular cavity. Typical acquisition parameters were 100 kHz modulation frequency, 15 G to 25 G modulation amplitude, and a microwave power of 0.2 mW. Data shown are an average of 1-5 scans. Low temperature EPR studies were performed with an Oxford continuous flow liquid

helium cryostat, and EPR spectra were manipulated using the WinEPR program software suite from Bruker.

EPR spectral simulation

X-band EPR spectral simulations were performed using the toolbox "EasySpin" of MatLab (MathWorks Inc.) which is capable of simulating EPR/ENDOR spectra of transition metal ions.[56] A program using EasySpin was written to solve the full spin Hamiltonian of a Mn^{2+} ion and several critical parameters (D, E and strain) were added to more accurately simulate the EPR spectra. Typical simulation parameters include a lineshape of 15 G, a D value of 520 MHz, and a range of E values from 0 to 173 MHz. All simulations were performed on a Dell PC running Windows XP Professional with 256 MB RAM and a 2.20 GHz processor. The simulations took approximately 10 seconds to 3 minutes depending on the parameters.

Room temperature Mn^{2+} binding isotherms

Mn^{2+} EPR signal intensities of RNA-containing samples were measured in comparison with standards of known concentrations to determine the amount of free Mn^{2+}. Since the binding of a Mn^{2+} ion to a biomolecule induces a zero field splitting due to the lower symmetry of a bound metal, an increase in the rotational correlation time, and changes in possible electron relaxation pathways, the EPR signal for bound Mn^{2+} at room temperature broadens beyond detection.[19] The loss of the room temperature EPR signal intensity is proportional to the Mn^{2+} bound to the biomolecule, allowing the number of Mn^{2+} bound per RNA molecule to be calculated (see Figure 2-3).[57,58] The resulting binding isotherms were fit with equation 2.3 using KaleidaGraph (Synergy Software) with a sum of *j* sets of n identical, non-interacting sites:

$$[Mn^{2+}{}_{bound}]/[hybrid] = \sum_{j=1}^{j} \{(n_i * [Mn^{2+}{}_{free}])/(K_d + [Mn^{2+}{}_{free}])\} \qquad (2.3)$$

The terms [$Mn^{2+}{}_{bound}$] and [$Mn^{2+}{}_{free}$] are the concentrations of bound and free Mn^{2+} ions in the sample, respectively, and K_d is the apparent dissociation constant. The RNA

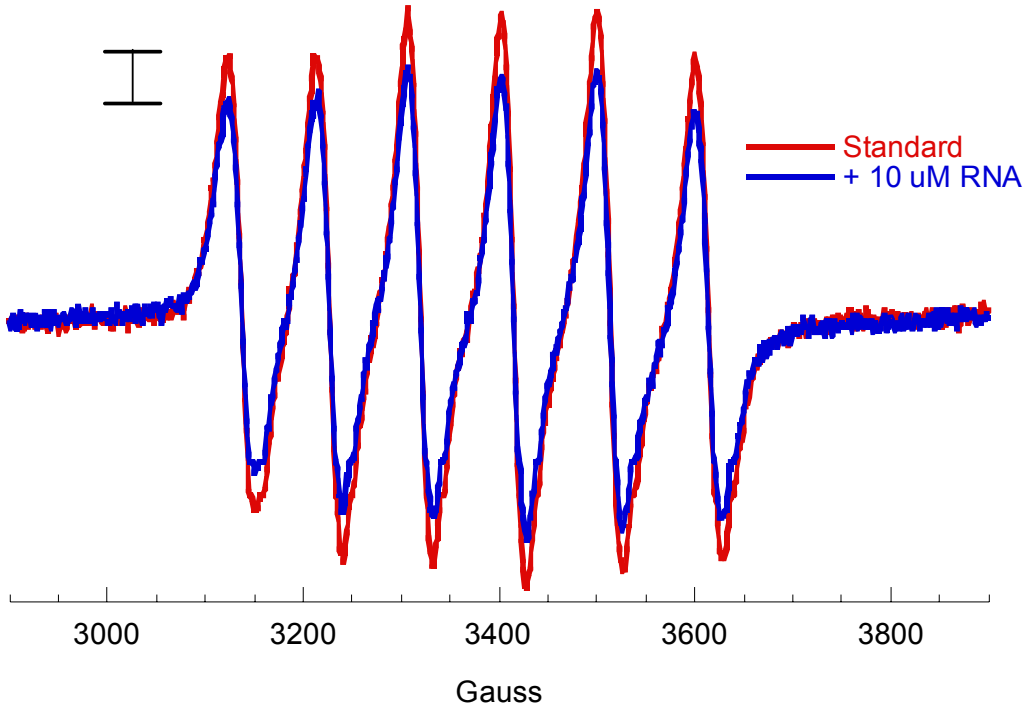

Figure 2-3: Room temperature Mn^{2+} EPR spectra comparison. The red spectrum is 100 μM Mn^{2+} standard sample and the blue is the same Mn^{2+} concentration with the addition of 10 μM RNA. The addition of the RNA causes a decrease in the signal intensity proportional to the amount of Mn^{2+} ions interacting with the RNA molecule.

model systems were generally fit using a single set of sites (j = 1) indicating that only one type of site could be resolved in the binding isotherms.

Power saturation studies

Information on T_1 and T_2, or the relaxation lifetimes, of a paramagnetic center can be acquired using an EPR power saturation technique at low temperatures. In this

experiment, the incident microwave power is progressively increased and the intensity of the EPR signal is monitored to determine the power required to saturate the signal. This phenomenon is governed by the Boltzmann distribution (equation 2.4), where N_i and N_o are the populations in the excited and the ground state respectively, E is the energy difference between the two states, k is the Boltzmann constant and T is temperature.

$$\frac{N_i}{N_o} = e^{-\Delta E/(kT)} \qquad (2.4)$$

At low levels of microwave power, the EPR signal is directly proportional to the square root of the incident power. At sufficiently high microwave powers the relaxation processes no longer allow the electrons to return to the ground state during the measurement and the two populations become equalized, thus reducing the signal intensity. The greater or more efficient the relaxation processes are, the higher the power that is needed to saturate the EPR signal.

By plotting the signal area versus the square root of power and fitting the curve using KaleidaGraph (Synergy) with equation 2.5, effects on the saturation behavior of the Mn^{2+} ions in the presence of the RNA were determined. For equation 2.5, A is the

$$A = I\, P^{1/2}[1 + (2^{1/\varepsilon}-1)\, P/P_{½}]^{-\varepsilon} \qquad (2.5)$$

peak-to-peak amplitude of the EPR spectra, I is a scaling factor, P is the incident power, ε is the measure of the homogeneity of saturation (values range from 0.5 for inhomogeneous saturation to 1.5 for homogeneous saturation), and $P_{½}$ is the microwave power needed to reduce the signal to half the maximum amplitude of the unsaturated value.[59] Since $P_{½}$ is related to the spin-lattice and spin-spin relaxation times, it can be used to detect changes in the relaxation characteristics due to interactions between Mn^{2+} ions.[59,60] The effect of the homogeneity factor, ε, measures the extent and type of

interaction responsible for the line broadening of the EPR signal. For experiments performed here EPR spectra were obtained with a microwave power range of 0.02 to 63 mW at a temperature of 20 K.

ESEEM spectroscopy

Electron spin echo envelope modulation (ESEEM) is a pulsed EPR technique able to obtain information on weak hyperfine interactions that are usually unresolved in conventional EPR methods due to inhomogeneous broadening of the EPR lineshape. The most common types of ESEEM spectra are obtained by using either a series of 2 or 3 high power microwave pulses. The 2-pulse method consists of a 90º–τ–180º where τ is the time between the pulses and the electron spin echo (ESE) detected EPR signal is obtained by plotting the integrated intensity of the resulting echoes as a function of τ. The 3-pulse experiment consists of a 90º–τ–90º–T–90º series of pulses where ESE signal amplitude is monitored as a function of T (see Figure 2-4).[61]

The 3-pulse sequence allows for only modulations at the fundamental hyperfine frequencies to be observed and typically has better frequency resolution than the 2-pulse sequence.[61] The value of τ can affect the modulation amplitude that allows for enhancement or suppression of a particular spin manifold when it is varied over a range of values determined by the period of the complementary hyperfine frequency. The resulting modulations of the echo are a series of overlapping sine waves that contribute to the overall echo decay. Fourier transformation takes the time domain data and converts it into the frequency domain. The data in this form can then be interpreted using the Larmor frequency and other information to identify the interacting nuclei as well as the A value. An advantage of ESEEM spectroscopy is the amplitude of the frequency

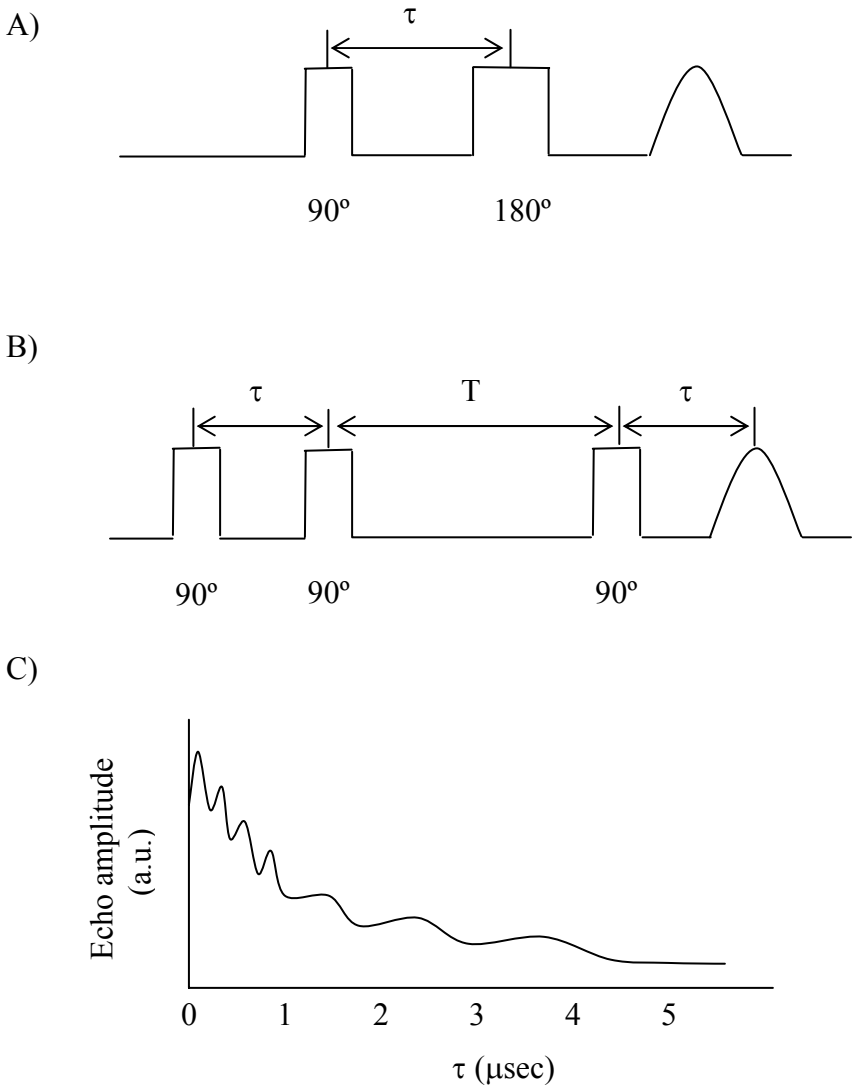

Figure 2-4: ESEEM pulse sequence and time-domain data. A) Two-pulse experiment, B) the three-pulse experiment, and C) the diagram of resulting spin echo produced. Fourier transform of the time domain data yields a frequency plot.

component can be used to quantitate the number of nuclei interacting with the electron spin. Useful nuclei that have been observed in metal RNA systems include ^{1}H, ^{14}N, ^{15}N and ^{2}D.[62]

Pulsed EPR spectroscopy was performed on a laboratory built 8-18 GHz spectrometer in Dr. R. David Britt's lab at the University of California, Davis.[63,64] Three-

pulse ESEEM experiments were performed using standard methods.[65,66] The RNA samples were transferred to 4 mm quartz EPR tubes (Wilmad) and frozen in liquid N_2 and shipped to for analysis and all spectra were obtained at a temperature of 4.2 K and a frequency of 9.3 GHz.

For the water counting experiments of Chapter III data were taken at three magnetic fields and the hydration level was determined by processing the H_2O and D_2O hammerhead samples to isolate modulations due to exchangeable aqua ligands in the first coordination sphere of the Mn^{2+}. Dividing the signal obtained from the D_2O sample by the signal of the H_2O sample effectively isolates the contribution of the coordinated D_2O molecules to the Mn^{2+} ion. The depth of the deuterium modulation is then compared to a reference sample with a know hydration level as described by Hoogstraten and Britt.[67]

Thermal denaturation of RNA

Denaturation occurs when the RNA molecule loses its secondary structure and adopts a random coil configuration. Thermal denaturation occurs when the temperature of the RNA is raised to a sufficient degree that the base paired region dissociates or melts. The temperature this phenomenon occurs at is commonly referred to as the melting temperature or the T_m value. The melting temperature reflects a cooperative transition where the entire helix will denature at once and not as a step-by-step dissociation process. Monitoring the UV region of 260 nm and 280 nm when the RNA strand melts, there is a noticeable increase in the absorbance due to the unstacking of the nucleobases, which results from the hyperchromicity effect.[1] Illuminating a stacked base with UV light produces an electronic transition in the base that induces an electric dipole in a neighboring base. The induced dipole will be opposite in direction to the excited

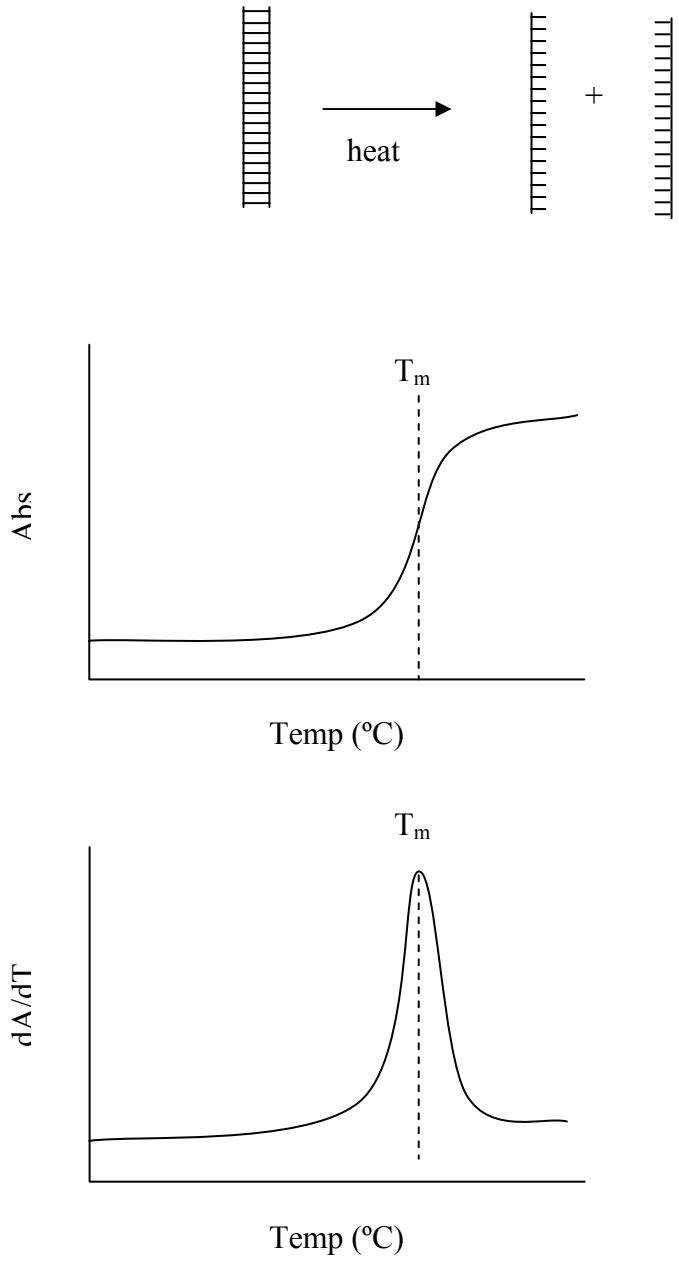

Figure 2-5: Thermal denaturation of a RNA duplex strand. A) Representation of the dissociation of an RNA duplex into two single strands, B) the change in absorbance at 260 nm upon increasing temperature, C) the derivative plot of absorbance as a function of temperature. The dotted line indicates the T_m or melting temperature of the RNA strand where the RNA is half paired and half unpaired.

transition dipole of the base producing a net decrease in the absorption. Denaturing the RNA breaks up the base stacking and causes an increase in the intensity of the amount of

light absorbed similar to a mixture of free nucleotides in solution. Melting of a simple RNA duplex can be treated as a two-state model where the RNA goes from paired to single strand without any intermediates (Figure 2-5). The 260 nm region monitors mostly the breaking of A-U base pairs while the 280 nm region monitors the breaking of the C-G base pairs. The midpoint of the transition between fully base paired and fully single stranded RNA is the T_m where ΔG is equal to zero as shown in equation 2-6.

$$0 = \Delta H - T_m \Delta S \qquad (2.6)$$

The T_m is directly related to several factors among them include the C-G/A-U content, the presence of unpaired regions, salt conditions, and the presence of divalent metal ions. The area of the curve is related to the van't Hoff enthalpy (ΔH) for the transition and was determined by fitting the derivative plot using the program Tmelt developed by Dr. Christopher running on a Unix based system.[68] The ΔS value was calculated at the T_m value, and ΔG was then calculated at 37ºC using the obtained ΔH and ΔS values.

Thermal denaturation studies of all the RNA complexes were carried out on a Cary Bio 300 UV/Vis Spectrometer equipped with a temperature controlled cell-block. All RNAs were annealed in the same manner as for the EPR binding studies, being heated for 90 seconds at 90ºC then cooled on ice for 30 minutes. Typical samples contained 2 μM RNA and 0-5 mM Mn^{2+} concentration in 100 mM NaCl, 5 mM TEA, pH 7.8 buffer. Melting profiles of higher RNA concentrations were also obtained in a range of 10 to 40 μM to check for the possibility of dimer formation. Absorbance at both 260 and 280 nm wavelengths were monitored as a function of temperature. The reciprocal of

the melting temperature (T_m) versus the log of metal concentration was fitted (KaleidaGraph, Synergy Software) to equation 2.7:

$$\frac{1}{T_m} = \frac{1}{T_o} - \left(R/\Delta H_o\right)\ln\left(\frac{0.5 + 0.5(1 + K_f L)^{0.5}}{0.5 + 0.5(1 + K_u L)^{0.5}}\right)^m \qquad (2.7)$$

where T_o is the melting temperature in the absence of added divalent metal, R is the gas constant, H_o is the van't Hoff enthalpy, K_f and K_u are the equilibrium affinities of a Mn^{2+} ion for the folded and unfolding RNAs, respectively, L is the free metal concentration, and m is the number of phosphates participating in the unfolding transition.[69]

CD spectroscopy

Circular dichroism measures the difference in absorption by a chiral molecule left- and right-handed circulary polarized light. The instrument produces two light waves that are polarized at 90º to each other and 90º out of phase with each other. This results in an electric field vector rotating in a circular manner at a fixed intensity and is called right circular polarized light. Using a second set of light waves that is -90º out of phase produces a wave vector rotating in the opposite direction creating left circular polarized light waves. When the right- and left-handed waves have equal intensity and wavelength, they add in a vector manner yielding plane-polarized light waves. Transmitting the plane-polarized light wave through an optically active medium that absorbs one of the circular polarized light waves more, drastically affects the intensity of that light wave, and thus the outgoing light wave is no longer plane-polarized and the resulting wave vector oscillates along an ellipsoid path. This light wave is referred to elliptically polarized light where the degree of ellipticity is related to how strongly the medium preferentially absorbs the incoming light waves.[70]

CD spectra were obtained using an Aviv 202SF CD spectrometer with sample containing 10 μM of RNA in a volume of 400 μL in a 0.1 cm pathlength cuvette at constant temperature of 25ºC. The measured ellipticity θ in mdegree was converted to molar residue ellipticity (Δε) values to correct for the length of the sequences by using equation 2.8:

$$\Delta\varepsilon = \theta/(33Cnb) \qquad (2.8)$$

where θ is the ellipticity value in degrees, C is the molar RNA concentration, n is the number of nucleotides, and b is the cuvette path length.[71]

Molecular modeling of the A9/G10.1 site

A simple molecular mechanics approach was used to model a metal ion bound at the A9/G10.1 site in the hammerhead ribozyme. The models were constructed from the Pley crystal structure[40] by deleting all bases except G8, A9, and G10.1. The Mn^{2+} ion was modeled coordinated to the N7 position of G10.1 and the pro-R oxygen of the A9 phosphate with four water molecules filling out the coordination sphere. To make coordination to the A9 phosphorothioate samples, a single sulfur atom was substituted for one of the non-bridging oxygen atoms of A9 phosphate in either in the Rp or Sp position. Experiments were also performed with a Cd^{2+} ion replacing the Mn^{2+} ion in the non-sulfur and sulfur substituted A9/G10.1 models.

The potential of each atom was assigned with the universal forcefield parameters. The energy of the structure was minimized using the Smart Minimizer energy minimization method in the program Cerius^2 (Accelrys) operating under Unix.

EXAFS spectroscopy

Extended X-ray absorption fine structure (EXAFS) is useful technique to study the coordination sphere of metal ions in biological systems. This technique uses a synchrotron radiation source due to its high intensity, brightness and broadband spectral

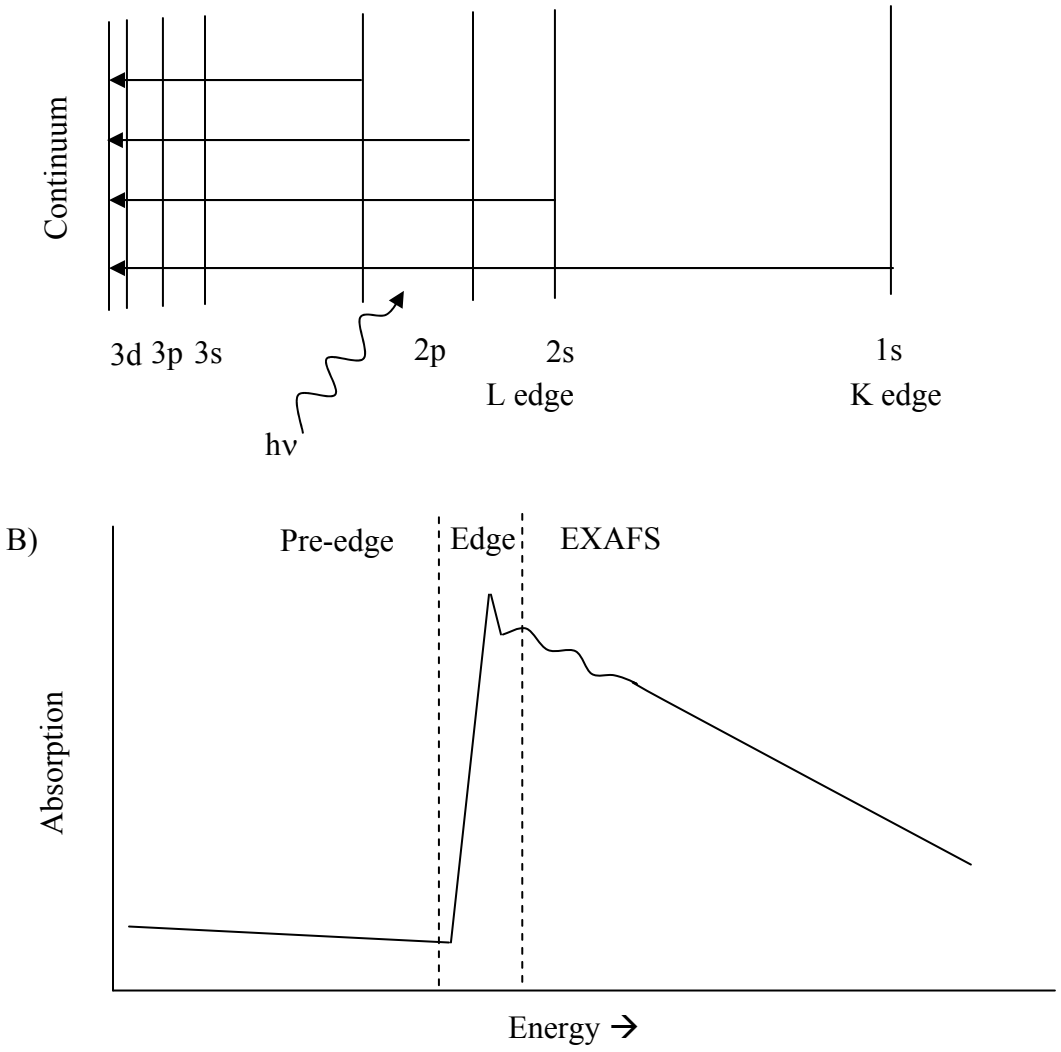

Figure 2-6: The X-ray absorption edge. A) The energy diagram of the K and L edges in X-ray absorption spectroscopy. The electrons are excited into the continuum when sufficient X-ray energy (hν) is applied. B) The X-ray absorption spectrum denoting the edge and EXAFS areas.

distribution.[72] The energy that at which an element's X-ray absorption occurs is dependent on the atomic number of that element. Due to instrumental limitations, it is difficult to observe atoms below Z = 17; this however allows for a transition metal ion to be the primary focus of an EXAFS study. EXAFS also sees an average environment for all metal ions in the system making studies of multiple metal sites difficult.

As the X-ray energy increases, the electrons of the metal ion are dissociated from the atom giving rise to a sharp absorption or discontinuities of the X-ray absorption. The energy photodissociation occurs at is directly related to the atomic number of the metal, which allows for selectively targeting a specific metal ion. Dissociation of the 1s core electrons gives rise to a discontinuity termed the K-absorption edge, while the dissociation of the 2s or 2p electrons give rise to the L-absorption edges (see Figure 2-6). Beyond the edge is the EXAFS region characterized by oscillations superimposed over a smoothly varying background. To isolate the EXAFS data, the background is subtracted and normalized yielding only the oscillations. The EXAFS phenomenon occurs when an absorber atom (a) has an electron dissociate from the core and thereby produces a de Broglie wave. A nearby atom (s) then reflects the wave back towards the absorber atom (or backscatters) with a phase and amplitude that varies with the applied X-ray energy. A series of periodic outgoing and backscattered waves is produced that reaches a maximum intensity when the waves constructively interfere and a minimum when destructively interference occurs. The resulting interference patterns are the EXAFS signal (see Figure 2-7).

Each atom produces a periodic oscillation of the backscattering wave that is a sum of phase-shifted sine waves arising from each backscattering atom or shell of scatters. A

shell is defined as a set of atoms (or backscatters) that are roughly equidistance from the absorber atom. The resulting sine waves are analyzed in three ways: the frequency, which provides distance information, the amplitude, which provides number of scatters, and the phase, which yields type of scattering atom. The data can then be analyzed using equation 2.9:

$$\chi(k) = k^{-1} \sum_{s} N_s \frac{|f_s(\pi,k)|}{R_{as}^2} \exp\left(-2\sigma_{as}^2 k^2\right) * \sin\left[2kR_{as} + \alpha_{as}(k)\right] \qquad (2.9)$$

where k is the wave vector, R_{as} is the distance between atoms a and s, N_s is the number of atoms in the shell, σ_{as} is the relative mean square deviation of the distance, and α_{as} is the

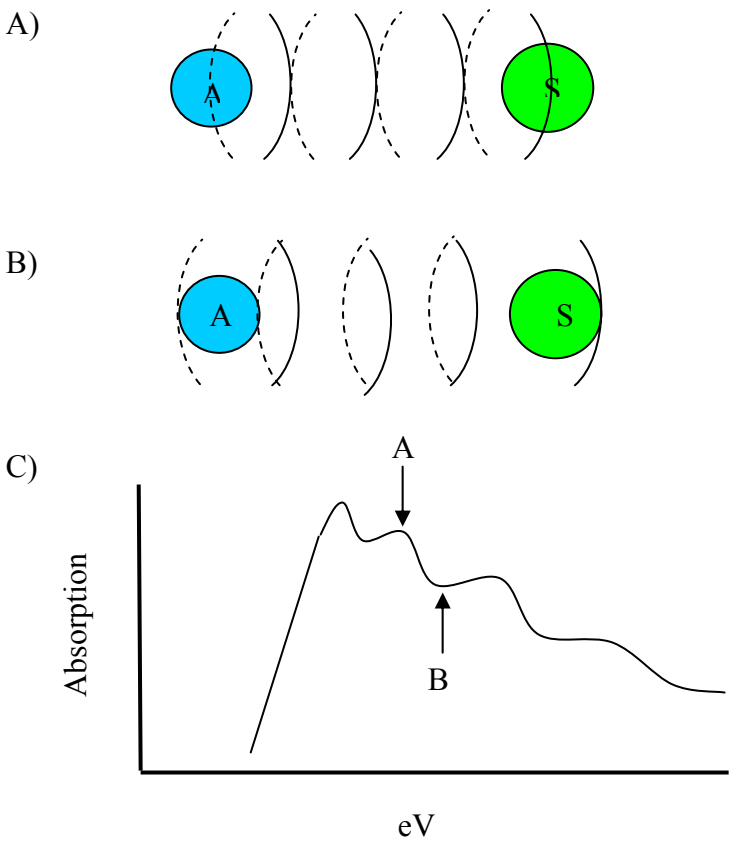

Figure 2-7: Backscattering of electron producing the EXAFS signal. A) Constructive interference pattern producing a maximum of the X-ray absorption coefficient. B) Destructive interference producing a minimum of X-ray absorption coefficient. C) EXAFS signal with the corresponding interference patterns indicated by the arrows.

phase that is dependent on the types of atom involved in scattering. The exponential term $\exp(-2\sigma^2_{as}k^2)$ is the Debye-Waller factor that describes the dampening in k space of χ arising from slight deviations of the distances of the scattering atoms.

Samples containing RNA were prepared in a manner similar to that of the EPR samples except in a volume of 65 μL with the addition of either Mn^{2+} or Cd^{2+} ions and then transferred to special transparent cuvettes, frozen in liquid N_2 and shipped in dry ice to our collaborators in Dr. Robert Scott's group at the University of Georgia at Athens. Data were collected at the Stanford Synchrotron Radiation Lab (SSRL) on beamline 9-3 running in fluorescence mode for frozen aqueous samples and transmission mode for crystalline samples. The Stanford Positron Electron Accelerating Ring (SPEAR) produced the synchrotron radiation used for the data collection.

Crystals of small model complexes

Crystals of small model complexes were prepared and characterized by X-ray crystallography for further study by EXAFS. A Mn-GMP crystal was prepared from 0.072 g of manganese(II) acetate (Aldrich) and 0.1 g of guanosine monophosphate (Sigma) following a procedure similar to that described by de Meester et al.[73] The Mn and GMP were added to autoclaved H_2O and the pH adjusted to ~ 5 with dilute HCl then heated for 2 minutes at 50ºC and allowed to cool undisturbed overnight. A Mn-phosphate crystal was prepared from a solution containing 0.05 g manganese(II) carbonate (Aldrich) in 1 mL of autoclaved water with the addition of 6 mL of 85% phosphoric acid.[74] The solution turned a light pink and was allowed to stand for 2-3 hours. The volume was reduced by blowing N_2 gas over the solution and small light pink crystals were formed. Dr. Joseph Reibenspies at the X-ray Diffraction Laboratory,

Center for Chemical Characterization and Analysis, obtained the X-ray crystal structures and provided analysis of the structures. The detailed reports are shown in the Appendix.

CHAPTER III

THE LOCATION AND COORDINATION SPHERE OF A HIGH AFFINITY MN^{2+} ION BINDING SITE IN THE HAMMERHEAD RIBOZYME

Introduction

Essential for their activity in biological systems, RNA molecules must be folded into their proper compact conformations. As a negatively charged polyelectrolyte, RNA molecules require the presence of cations for screening the negative charge of the phosphate backbone, and binding at specific sites to aid in folding into the correct tertiary structure.[8] The correct folded form is critical for the correct function of catalytic RNA's, or ribozymes.[7,75] Divalent metal ions have been observed bound to specific sites in X-ray crystal structures of several ribozyme molecules.[44,76,77] One metal site that has been extensively studied is the A9/G10.1 site found in the hammerhead ribozyme (Figures 3-1 and 3-2). According to the crystal structures, both Mg^{2+} and Mn^{2+} ions may populate this position.[40,42]

Although the hammerhead ribozyme is active in the presence of exchange-inert metal ion complexes, monovalent ions or divalent cations, the latter requires lower concentrations for catalysis of the cleavage reaction of the phosphodiester bond.[36-38] The A9/G10.1 residues are located in the conserved core of nucleotides, which are essential for catalytic activity.[30,32] Modification at the A9 site has been shown to have a profound effect on the catalytic activity despite the ~ 20 Å distance from the cleavage site that is predicted by the crystal structure (Figure 3-2).[49,78] The implications of a metal ion bound at this site on catalytic activity have been debated.[49,50]

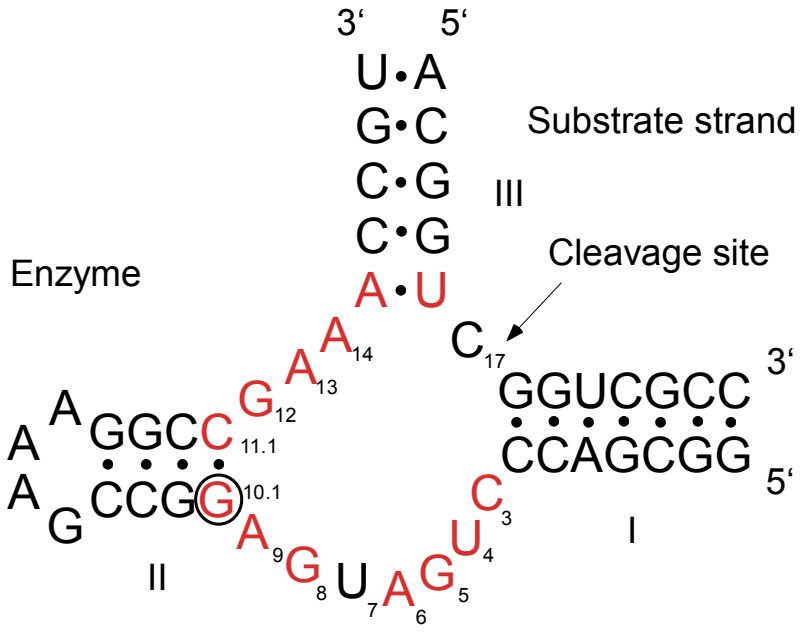

Figure 3-1: Hammerhead ribozyme construct. The circle denotes the location of the deoxy modification and the placement of the ^{15}N labeled guanine residue.

Herschlag and co-workers removed the guanine base at the G10.1 site and measured the relative activity of the abasic construct versus the wild type and found a value of 0.04, suggesting an important role for this position.[34] Replacement of the N7 of the G10.1 residue with a carbon results in a 30-fold decrease in the rate of the hammerhead reaction, while a deoxy modification of the guanine at G10.1 has only a < 3-fold reduction on the activity (circled residue in Figure 3-1).[49]

Utilizing the inherent physical properties of Mn^{2+} as a paramagnetic spectroscopic probe and a functional substitute for Mg^{2+}, EPR (Electron Paramagnetic Resonance) studies have been performed to investigate the binding characteristics of Mn^{2+} ions with structured RNA's.[19-22,62,67,79] Room temperature EPR studies in 1 M NaCl were able to isolate a single high affinity Mn^{2+} ion bound to the HH with a K_d of less than 10 μM.[19] Low temperature EPR studies, also under high salt concentration, yielded a distinct EPR

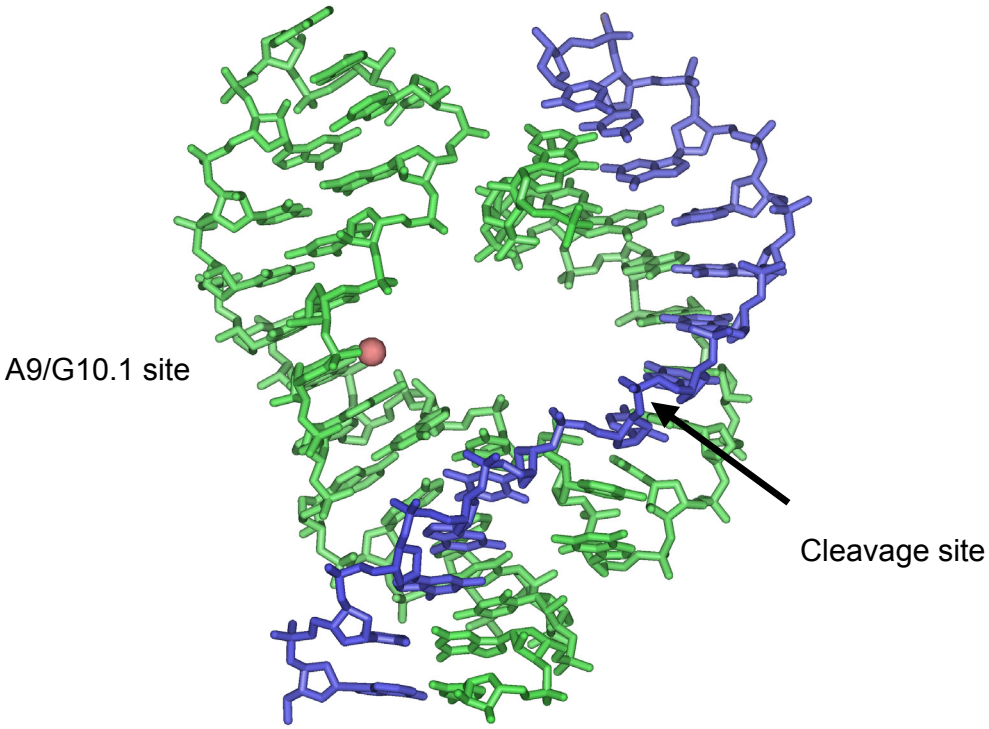

Figure 3-2: Crystal structure of the hammerhead ribozyme with a Mn ion at the A9/G10.1 site. The green is the enzyme strand, the blue is the substrate strand, and the arrow denotes the cleavage site. PDB 1HMH.

spectrum implying a specific environment for the Mn^{2+} ion bound to the hammerhead. Further studies using ^{31}P ENDOR (Electron Nuclear Double Resonance) spectroscopy on this site revealed the presence of phosphate coordination to the Mn^{2+} ion.[21] The high affinity site has also been explored using ESEEM (Electron Spin Echo Envelope Modulation) spectroscopy which was used to determine the type of nucleotide involved in the coordination sphere.[20,22] The WT HH sample in a 1 to 1 ratio of Mn^{2+} to RNA showed signals due to coordination to a ^{14}N ligand. An all ^{15}N guanine labeled enzyme strand was prepared by *in vitro* transcription using ^{15}N labeled GTP.[20] Results from those experiments indicated that nitrogen from a guanine residue was also coordinated to the

high affinity metal site in the hammerhead. However, the exact position of this residue remained unclear.

Here, site-specific ^{15}N labeling has been used to unambiguously identify the high-affinity Mn^{2+} site in the hammerhead ribozyme as the A9/G10.1 site. ESEEM H_2O counting experiments have been shown useful in quantitating the number of bound water molecules to a paramagnetic metal ion in RNA systems,[67] and are performed here in order to determine the hydration level of Mn^{2+} in the hammerhead high affinity site. The characterization of the high affinity Mn^{2+} site in the hammerhead ribozyme under solution conditions is consistent with the A9/G10.1 site observed in the crystal structure. This site is especially sensitive to alterations that have a dramatic effect on the cleavage reaction.

Results and discussion

Characterization of G10.1 deoxy modified hammerhead

In order to specifically place a single ^{15}N labeled guanine residue in the enzyme strand of the hammerhead, a chemical synthesis approach was taken. Commercially available ^{15}N labeled deoxy guanine containing a phosphoroamidite linkage was used in chemical synthesis of hammerhead enzyme strand allowing a single ^{15}N deoxy guanine residue to be placed at the G10.1 site. Placement of a deoxy modification in the conserved core of the hammerhead may cause misfolding or alter the activity of the construct. A series of control experiments were performed in order to determine the effect, if any, the deoxy modification has on the activity when compared to the WT hammerhead sequence.

Activity studies were performed with the dG10.1 enzyme strand and 13nt substrate strand similar to previously described work by Horton et al.[19] Activity studies were performed in 100 mM NaCl, 5 mM TEA, and pH 7.8 with excess enzyme concentration under single turnover conditions with an enzyme concentration of 3 μM. The Mn^{2+} concentration was varied from 1 to 10 mM and the reaction was quenched by addition of 50 mM EDTA and 8 M urea buffer.

The deoxy-modified hammerhead at the G10.1 residue has a k_{obs} of approximately 10 /min at a concentration of 5 mM Mn^{2+} while the rate of the wild type hammerhead is approximately 12 /min at the same concentration of manganese (see Figure A-1). These results are indicative of very little effect on the activity and are similar to what was previously reported.[49]

EPR spectra

Since the high affinity Mn^{2+} ion in the hammerhead has a unique EPR signature on the 6th line, comparison of spectra of the WT and dG10.1 in a 1:1 ratio of Mn^{2+} to RNA was performed. The dG10.1 ^{14}N sample had a concentration of 360 μM, the wild type hammerhead containing natural abundance of ^{14}N a concentration of 400 μM. The low temperature EPR spectrum of Mn^{2+} in the wild type hammerhead sample shows the typical six-line hyperfine pattern caused by the I = 5/2 value of the Mn^{2+} ion centered at g ~ 2.0 as seen in Figure 3-3. Compared to Mn^{2+} in a buffer sample, the WT HH sample has a distinct lineshape that is most noticeable on the sixth line of the EPR signal. The change is due to a difference in the zero field splitting (zfs) of the M_s levels altering the positions of the forbidden transitions resulting in more pronounced allowed lines when the Mn^{2+} ion is bound to the hammerhead ribozyme. This feature has been previously

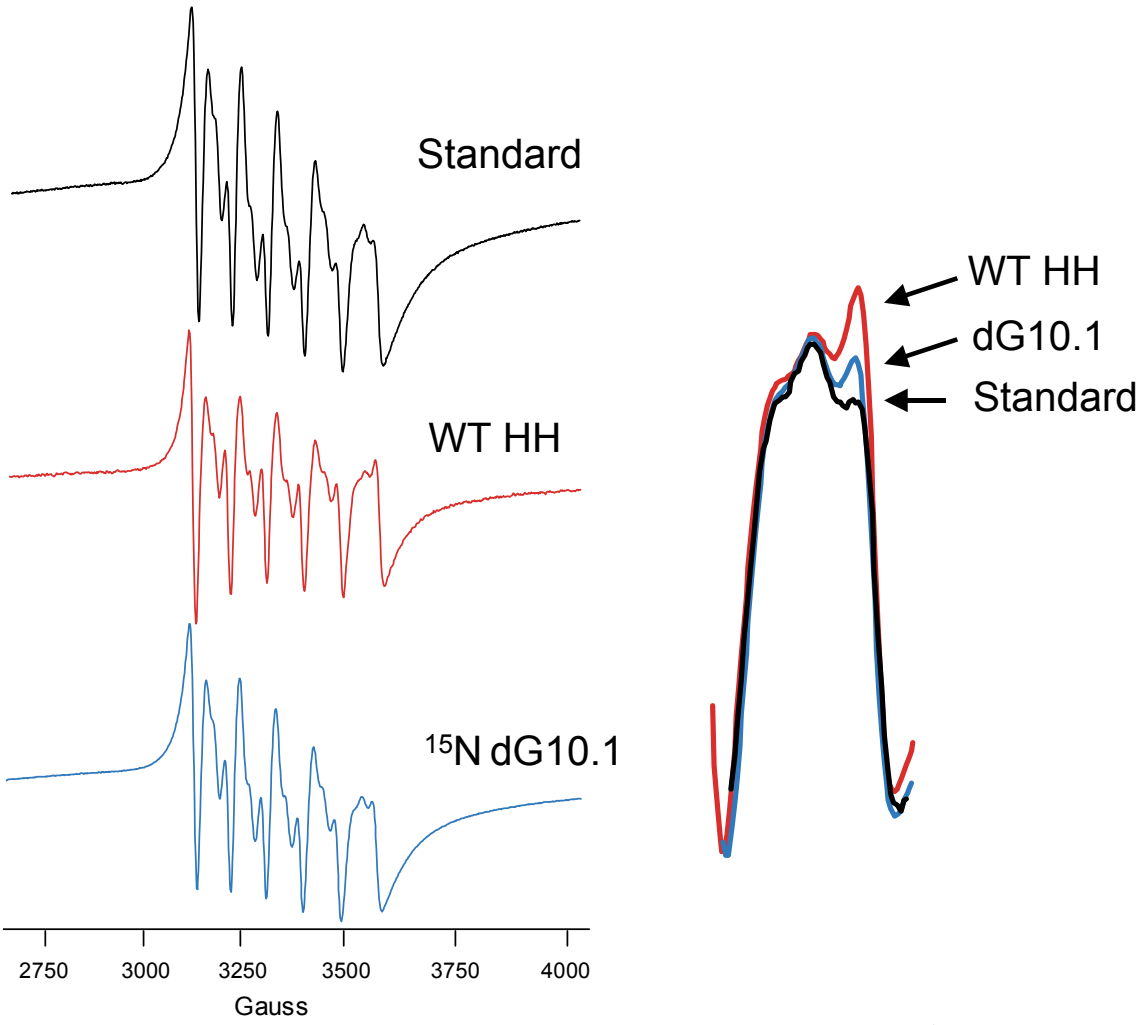

Figure 3-3: Mn EPR spectra comparison. The insert shows a blowup and overlay of the 6th line feature of the EPR spectra. The WT hammerhead spectrum (400 μM RNA) shows a distinctive feature on the 6th line that differs from the standard. The dG10.1 sample has a similar, although less intense feature on the 6th line.

observed for the Mn^{2+} ion bound to the WT HH and attributed to a high affinity metal ion binding site.[21] The source of this signature is an increase in the rhombic zfs parameter, E, compared to the standard sample as determined from simulations of the EPR spectrum and is discussed in more detail in Chapter V.

Sub-stoichiometric concentrations of Mn^{2+} to the dG10.1 HH were investigated to observe the effect on the EPR lineshape. The spectrum of the 0.9 equivalents of Mn^{2+}

had more defined features, while that of the 0.7 equivalents was even better resolved. Sub-stoichiometric concentrations of 0.8 Mn^{2+} ions to the RNA hybrid was used is subsequent ESEEM studies to ensure that the majority of the Mn^{2+} ions were bound and not free in solution for the dG10.1 sample. An EPR sample of the dG10.1 ^{15}N labeled hammerhead with 0.8 equivalents of Mn^{2+} to RNA in 1 M NaCl, 5 mM TEA, at a pH of 7.8 containing 20% ethylene glycol was prepared. The EPR spectrum for the dG10.1 HH shows a similar, although weaker, feature to that observed for the WT HH sample (Figure 3-3 inset). This difference may arise from slight changes in the RNA structure with the presence of the deoxy modification around the A9 site. This change in the EPR spectrum is consistent with the effect the presence of the dG10.1 base has of slightly decreasing the cleavage activity.[49]

ESEEM spectroscopy

ESEEM spectroscopy is useful in observing weak hyperfine coupling that is not detected in conventional EPR, and has been previously used to observe such nuclei as ^{14}N[20,22,62] and ^{15}N[20,62] and ^{2}D[67] in RNA systems. The 3–pulse ESEEM spectrum of Mn^{2+} in the WT HH shown in Figure 3-4 displays a pattern consistent with the Mn^{2+} ion coordinated to ^{14}N. The features appearing at 0.6, 1.9, and 2.5 MHz are attributed to ν_0, ν_-, and ν_+ sublevels with the feature at 5.2 MHz from ν_{dq} of the ^{14}N quadropole splitting parameters.[20] Mn^{2+} bound to the natural abundance dG10.1 sample shows the identical ESEEM pattern, indicating that the deoxy modification has a minor effect on the metal binding site. The intensity of the ESEEM signal, however, was 70% of the WT sample indicating a lowered amount of bound Mn^{2+} ions. ESEEM spectra were also obtained on the ^{15}N dG10.1 HH sample, and contained only a single broad feature at 3.5 MHz from

the I = ½ of the ^{15}N nuclei (Figure 3-4). The ESEEM spectrum does not show any additional features of ^{14}N coordination ruling out multiple binding sites of the high affinity Mn^{2+} ion. This is conclusive proof of the homogeneity of the Mn^{2+} ion binding to the hammerhead at the G10.1 site.

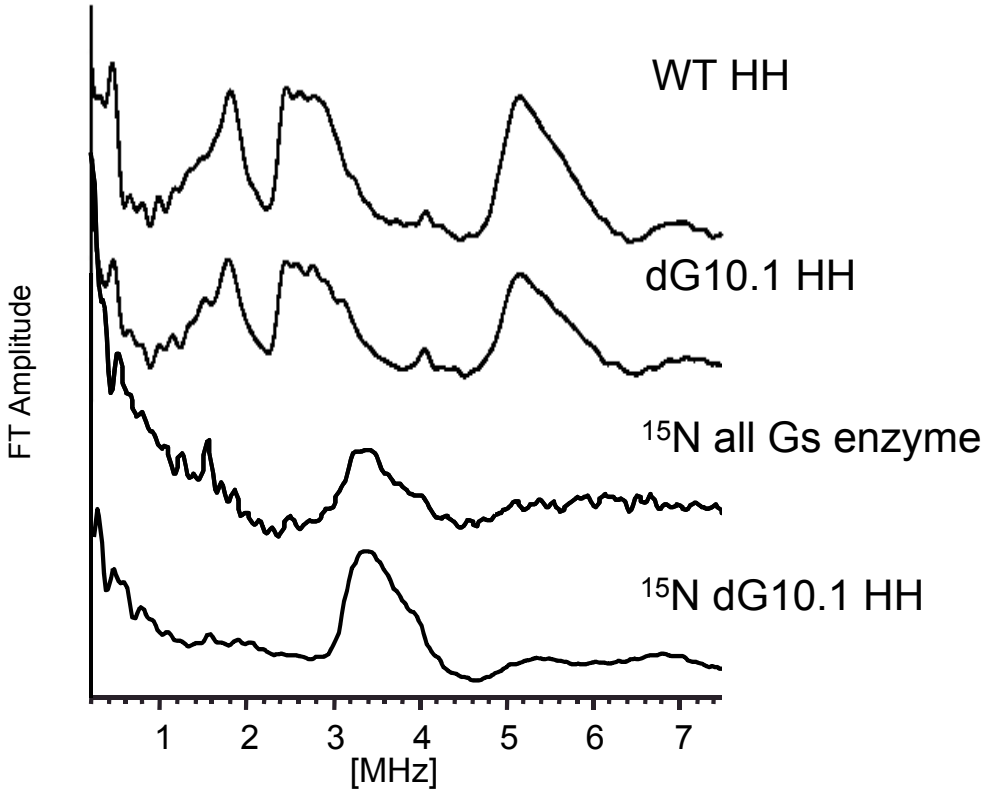

Figure 3-4: Comparison of ESEEM results obtained for the hammerhead ribozyme. The WT and dG10.1 HH samples both show signals typical of the Mn coordinated to ^{14}N ligand. The all ^{15}N guanine labeled enzyme strand[20] and the ^{15}N dG10.1 show a single feature consistent with Mn coordination to ^{15}N ligand.

ESEEM H_2O counting

The ESEEM H_2O counting experiments require two samples, one prepared in a buffer with H_2O and the other sample in a buffer with D_2O. The RNA for the H_2O sample was prepared in the same fashion as previous samples and is described in Chapter II. For the RNA in D_2O, the preparation procedure was slightly altered. After ethanol

precipitation, both the enzyme and substrate RNA strands were dried by speed vacuum and then brought up in D_2O, and lyophilized. Additional D_2O was added to the pellet and the sample was lyophilized again, and this procedure was repeated 3 times. The final RNA pellets were then brought up in 1 M NaCl, 5 mM TEA, pH = 7.53 (pD = 7.93) buffer in D_2O. The EPR samples were prepared with 350 μM of RNA hybrid and 250 μM of Mn^{2+}, and 0.4 M sucrose as the cryoprotectant in either H_2O or D_2O. Samples were then transferred to quartz EPR tubes and frozen in liquid N_2. Figure 3-5 shows the echo detected EPR spectrum for the Mn^{2+} hammerhead ribozyme in D_2O and the arrows indicate the magnetic field positions where data were collected.

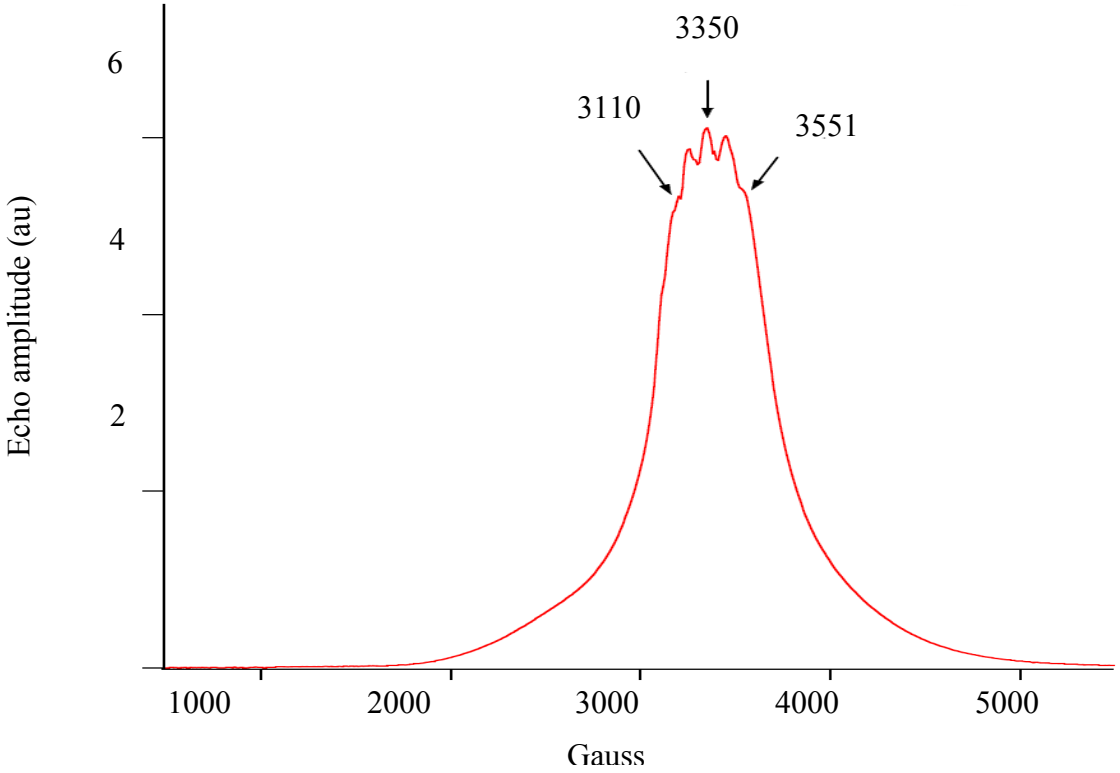

Figure 3-5: Field swept echo-detected EPR spectrum of Mn-hammerhead in D_2O. Arrows indicate the magnetic field positions where ESEEM data were collected.

Previous ENDOR results showed the presence of coordinated H_2O molecules; however, these results lacked the ability to quantitate the number of H_2O bound to the manganese ion.[21] To determine the exact number of H_2O molecules coordinated to the high affinity Mn^{2+} site, hammerhead samples were prepared in D_2O and ^2H ESEEM was used to determine the number of bound D_2O molecules. The technique involves the comparison of RNA samples in H_2O and D_2O to isolate the inner-sphere coordination to the Mn^{2+} ion and Hoogstraten and Britt cover in detail the method for obtaining these data and their analysis.[67] The depth of the ^2H ESEEM modulation is directly proportional to the number of D_2O molecules coordinated to the Mn^{2+} ion. The relative hydration level is obtained by direct comparison of the ESEEM results of the processed data for the H_2O and D_2O samples to expected hydration level curves obtained from a $Mn(H_2O)_6^{2+}$ reference sample. Figure 3-6 shows the comparison of the ^2H ESEEM spectrum of the hammerhead to a set of relative hydration levels calculated from a standard. The data were obtained at 3 different magnetic fields in order to verify the reproducibility of the results show an average of 4.08 ± 0.12 H_2O molecules coordinating to the high affinity Mn^{2+} ion in the hammerhead.

Model of high affinity Mn^{2+} site

Figure 3-7 shows a model of the high affinity Mn^{2+} site in the hammerhead that is based on the EPR results. The ligands coordinated to the Mn^{2+} ion are the Rp O from the phosphate of A9 and the N7 from G10.1 with four H_2O molecules as determined by the H_2O counting results. The results and procedure for the molecular modeling are described later in Chapter VI. The starting distance between the Mn^{2+} ion and the phosphorus is approximately 3.9 Å when Mn^{2+} is placed at this site according to

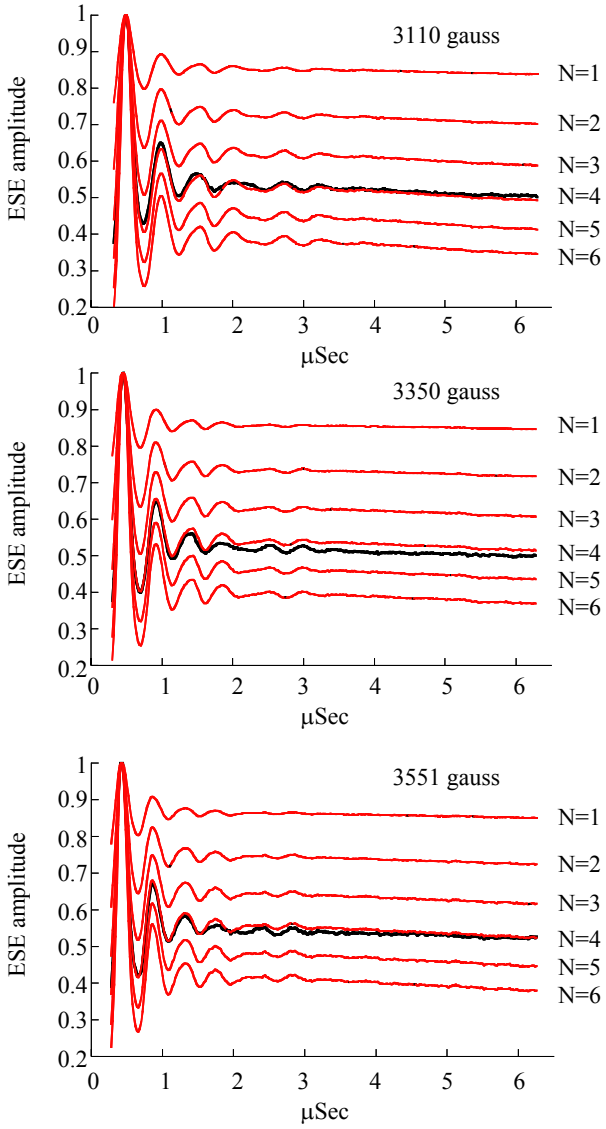

Figure 3-6: Hydration determination for Mn^{2+} in the hammerhead high affinity site. Red lines are calculated for relative hydration levels; black lines are the results for the hammerhead. Conditions were 1 M NaCl, 5 mM TEA, pH 7.5 in D_2O, with 0.4 M sucrose as a cryoprotectant.

coordination from the Pley crystal structure (1HMH). After energy minimization, the Mn-P distance reduced to 3.2 Å, which is consistent with the 3.3 Å value observed in the Mn-ATP crystal structure.[80] The remaining RNA structure had only slight rearrangements of the sugar and bases from the crystal structure. The symmetry around

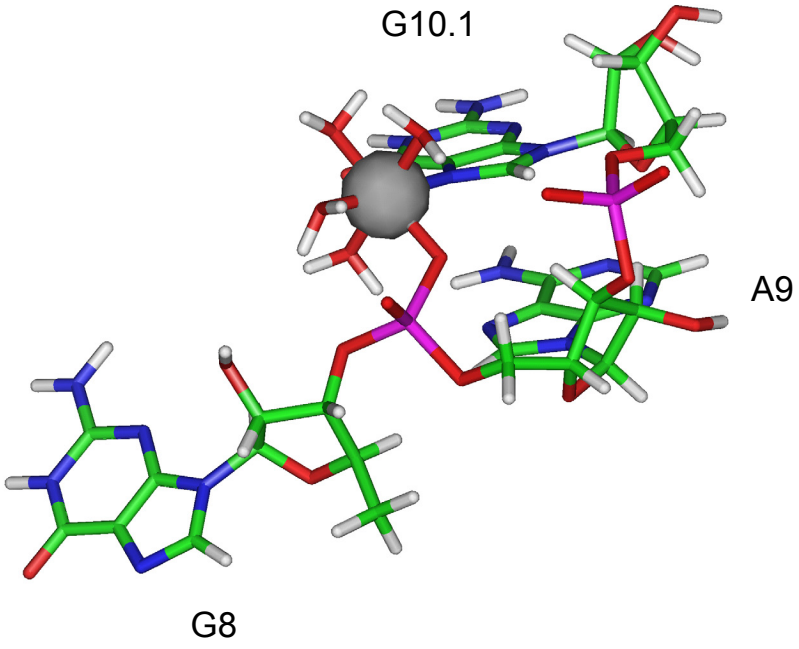

Figure 3-7: Model of the A9/G10.1 site based on EPR results and X-ray crystallography. The Mn^{2+} ion is coordinated to the N7 of G10.1 and the pro-R O of the A9 phosphate.

the Mn^{2+} ion deviates from pure octahedral symmetry and this may be partly the reason the high affinity manganese ion has a unique feature in the EPR spectrum compared to that of a standard in buffer or simple model complexes.

Conclusion

To fold the hammerhead ribozyme into its tertiary structure, the negative phosphate backbone must be neutralized by either diffuse or chelated cations to allow the phosphate groups to come in close proximity. While Mg^{2+}, Mn^{2+}, Na^{+} or K^{+} can stabilize RNA tertiary structure, divalent metal ions are more effective due to their higher charge to radius ratio.[10] Monovalant and divalent metal ions can be either diffusely bound or directly coordinated to the RNA molecule, with Mn^{2+} and other transition metal ions more readily forming stronger interactions to RNA compared to Mg^{2+} or Na^{+} ions. A major factor in determining if a metal ion binds to RNA in a diffuse or chelated manner is

the energetic cost of dehydration.[10] Sites in RNA that favor chelated metal ions have high negative potential to compensate for any energetic penalties of direct metal ion coordination.

The crystal structures of the hammerhead under all the different conditions that were studied showed that the folded structure of the ribozyme is a compact gamma shape. Crystals soaked in Mg^{2+}, Mn^{2+} and Cd^{2+} ions show several potential metal ion binding sites in the hammerhead at A9/G10.1, at G5 and near the scissile phosphate. Although in the crystal the hammerhead is fully folded, under solution conditions the tertiary form and the folding pathway of the hammerhead ribozyme are dependent on the ionic conditions. Pardi and coworkers, using residual dipolar coupling, have demonstrated that in the presence of 100 mM Na^{+} ions the hammerhead is in an extended conformation with the stems fully separated.[81]

Lilley and coworkers, using FRET and ^{19}F NMR, also showed that under low salt concentrations the hammerhead ribozyme is in an extended conformation that undergoes a two-step folding transition to a more compact structure upon the addition of Mg^{2+} ions.[30,47,48] The first folding transition occurs within domain II upon the addition of $\leq$ 500 μM Mg^{2+} with a very high binding affinity, while the second folding transition of domain I occurs in the presence of 1-25 mM Mg^{2+} ions.[47] These studies have demonstrated the ability of low concentrations of divalent metal ions to fold the hammerhead into its compact tertiary structure that is observed in the crystal structures.

The electrostatic surface plot of the hammerhead crystal structure shows an area of high negative potential at the A9/G10.1 site.[53] All the EPR results taken together for the high affinity Mn^{2+} ion-binding site show coordination to the N7 of G10.1, the

phosphate oxygen of A9 and four H_2O molecules as shown in Figure 3-7. This coordination confirms the metal ion at the A9/G10.1 site observed in the crystal structure as the high affinity metal ion site in the hammerhead under solution conditions. These results suggest that the N7 of G10.1 and the Rp phosphate oxygen of A9 are positioned in a specific orientation to form a binding pocket for a metal ion to coordinate at this site. The significance of a metal ion bound at this site is essential in neutralizing the high negative potential of this pocket to allow the hammerhead to fold into its tertiary structure. The EPR results show that the high affinity Mn^{2+} ion remains quite hydrated, having four water molecules while coordinated in this pocket. The fact that the Mn^{2+} ion retains a high level of hydration is consistent with the high energetic cost of direct coordination of a metal ion to an RNA molecule.

The small differences between the EPR and ESEEM results for the Mn^{2+} ion bound at the A9/G10.1 site of the WT and dG10.1 hammerhead sequences must solely arise from the change of the 2' position of the sugar. The ribose sugar has 3'endo puckering while the deoxyribose has 2'endo puckering. The change in puckering must affect either the coordination of the metal ion at the A9/G10.1 site or the folding of the conserved core. The change in the lineshape of the EPR spectrum and the lower amplitude of the ESEEM results compared to the WT hammerhead are consistent with a slight change in the coordination of the metal ion to the A9/10.1 site.

Although X-ray crystal structures show potential metal binding sites, they do not reveal any information on the affinity for metal ions at these sites or their importance on the activity or folding of the RNA. Solution studies, however, can provide this information and relate the effect metal ions have on the function of the ribozyme. The

determination that the high affinity Mn^{2+} site under solution conditions is the A9/G10.1 site observed in the crystal structure is a major step in understanding the relationship between divalent metal ions and the structural roles they play in RNA molecules. Although the exact function the A9/G10.1 metal site in the hammerhead ribozyme plays in activity is still uncertain, it is important to note that this high affinity metal ion-binding site is very sensitive to any slight modification of the bases or phosphate group in this location that directly affects the catalytic activity. This is surprising that since from the crystal structure it is 20 Å away from the cleavage site and appears to have no direct role on the reaction. Isolation of this site may allow for further studies of the importance of the A9/G10.1 site on the hammerhead structure and function.

CHAPTER IV

INTERACTIONS OF MULTIPLE METAL IONS IN THE HAMMERHEAD RIBOZYME

Introduction

Crystal structures of the hammerhead ribozyme have been obtained in the presence of various divalent metal ions, showing areas for potential metal ion-binding sites. These potential metal sites include the A9/G10.1 site (site A in Figure 4-1), adjacent to the cleavage site (sites B, C)[82], in stem I near nucleotide 2.2 (site D)[83], and near G5 in the uridine turn (site E).[38,40,42,84,85] It is of interest to determine whether, under solution conditions, metal ions occupy the sites observed in the crystal structure. Previously, it was shown under solution conditions that a single high affinity site can be populated in 1 M NaCl, and this was conclusively proven to be the A9/G10.1 as described in Chapter III. The crystal structure also shows three Mg^{2+} ions near stem I and the cleavage site, approximately 10 Å away from the A9/G10.1 metal ion site. The farthest metal ion is the ion at the G5 site with a distance of 19 Å. The goal of this study is to find spectral signatures for these other core metal ion sites.

Under solution conditions it has been demonstrated by Mn^{2+} room temperature EPR binding isotherms that the hammerhead ribozyme contains two types of binding sites. In 0.1 M NaCl, the first type of site contains approximately 3-4 Mn^{2+} ions with a low K_d value of 3.3 ± 2.7 μM. The second type of site contains approximately 7 ions with a higher K_d of 122 ± 48 μM.[52] One of the high affinity Mn^{2+} ion binding sites has been determined to be at the A9/G10.1 site; the locations of the remaining sites have yet to be determined. To explore the possibility of metal ions populating the sites in the core

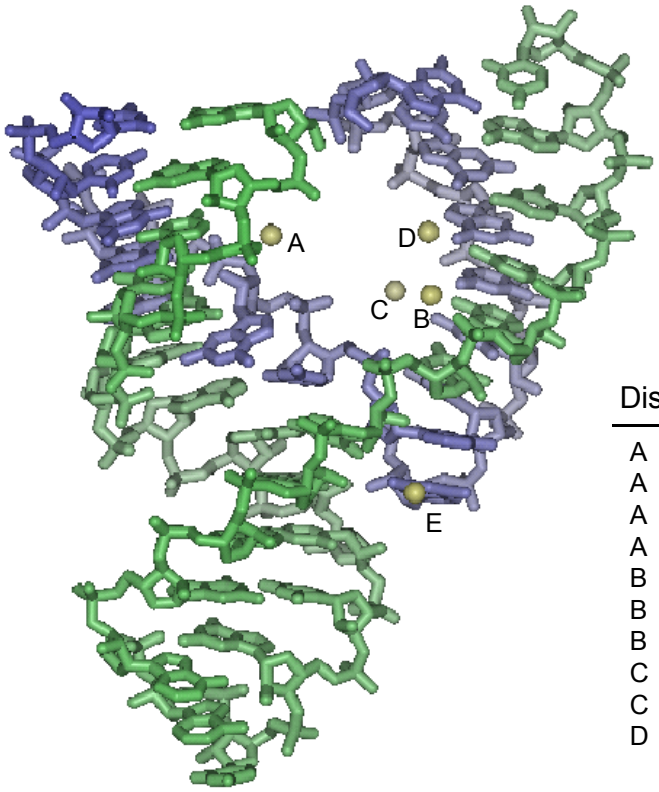

Distances (Å)

A	B	10.9
A	C	10.5
A	D	9.8
A	E	18.9
B	C	8.6
B	D	4.5
B	E	12.5
C	D	7.6
C	E	16.1
D	E	16.8

Figure 4-1: Crystal structure of the hammerhead ribozyme with Mg ions. Five Mg ions have been observed coordinating at A the A9/G10.1 site, B-D near the cleavage site and stem I, and E near G5. Distances between these ions are given in the inserted table. PDB 300D.

of the hammerhead and to develop a spectroscopic signature for this interaction, Mn^{2+} EPR power saturation techniques were employed to probe for interactions between Mn ions in close proximity to each other.

EPR power saturation is a technique where the applied microwave power is increased to while observing the effect on the EPR signal. Before excitation, the Boltzmann distribution describes a higher concentration of spins in the lower energy level. The applied microwave energy is absorbed by the electron spins and raises them to the excited state. Through various relaxation pathways, the excited spins return back to

the ground state. At low microwave powers below the point of saturation the EPR signal intensity is linearly related to the square root of the incident power. At very high microwave powers, the relaxation pathways may be too slow to dissipate the extra energy of the excited electrons and the upper energy level remains populated during the measurement time. This causes a reduction in the signal intensity due to the equalizing of the different spin populations, resulting in saturation of the EPR signal. If the paramagnetic Mn^{2+} ions are in close proximity to each other, they can provide additional relaxation processes and thus reduce the extent of saturation at a given microwave power.

EPR power saturation methods provide information on the relaxation properties of the paramagnetic species. The two relaxation processes that dissipate the energy of the excited state are spin-lattice (T_1) and the spin-spin (T_2) mechanisms. Spin-lattice relaxation exchanges the energy of the spin system and the lattice vibrations. Spin-spin relaxation occurs when two or more spin centers are close enough in proximity to create sizable magnetic fields at each center. This produces an exchange of energy between the spins of both centers that dissipates the energy.

A series of RNA complexes was used in this study to illustrate the differences between the wild type hammerhead RNA with specific metal ion binding sites and different RNA molecules without these sites (Figure 4-2). The Poly U hammerhead construct replaced all of the nucleotides of the conserved core with all uridine residues, which renders this complex inactive and most likely misfolded. A 13-nucleotide duplex was used as a control sample for studying the behavior of Mn^{2+} ions in a small RNA duplex with only A-form geometry and no specific metal ion-binding sites. A comparison of the Mn^{2+} ion-binding properties was performed as well as power

saturation experiments to determine the proximity of the ions to each other in the hammerhead samples.

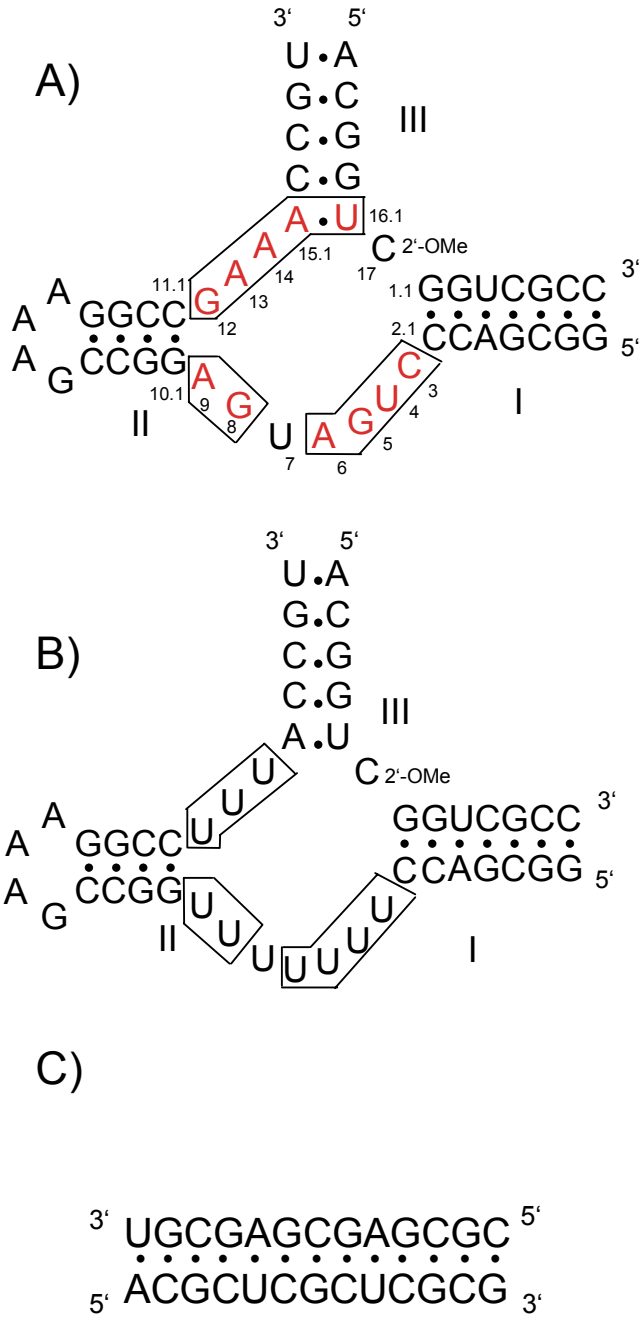

Figure 4-2: RNA strands used for EPR power saturation study. A) WT hammerhead, B) Poly U hammerhead mutant, C) 13mer RNA duplex.

Results and discussion

Specific vs. non-specific metal-RNA interactions

Divalent metal ions interact with RNA molecules in specific and non-specific manners. Specific interactions occur when the metal ion is coordinated at a certain site and has exchanged one or more H_2O ligand with a ligand from the RNA molecule. Non-specific metal interactions are purely electrostatic influence due to the negative charge of the phosphate backbone, and the metal ion remains fully hydrated.

The Mn^{2+} EPR binding isotherm for the hammerhead ribozyme shows a tight set of sites binding 2.5 ± 0.9 Mn^{2+} ions binding with an apparent K_d of 3.3 ± 2.7 μM for the, and a weaker set binding 7.1 ± 0.7 Mn^{2+} ions binding with an apparent K_d of 122 ± 48 μM (see Figure 4-3).[52] To determine if the weak metal ion binding sites observed for the hammerhead are from non-specific metal-RNA interactions, comparison of the EPR binding isotherms of a 13nt RNA duplex was performed. Results for the duplex fits to one type of site that binds 3.5 ± 0.3 Mn^{2+} ions with an apparent K_d of 147 ± 47 μM. Since the 13mer RNA duplex has A-form helical structure and no specific metal ion-binding sites, the number of ions bound and the K_d values would be typical for a set of weakly non-specific Mn^{2+} interaction with the RNA. The weak metal ion sites observed for the hammerhead have similar apparent K_d value that likely arise from non-specific ions interaction with the hammerhead.

The 13mer RNA duplex was also examined by metal dependent UV thermal denaturation experiments. The purpose of experiment is to compare apparent affinities measured by EPR with those measured via changes in stability. The duplex RNA melts as a single transition with a T_m value of 75.6ºC. The addition of Mn^{2+} ions stabilizes the

RNA molecule and increases the T_m value with an approximately overall 4ºC change at the highest Mn^{2+} concentration. These data are shown as a plot of $1/T_m$ (K^{-1}) versus log concentration of Mn^{2+} ions (Figure 4-4). Fitting these data yields values for K_f and K_u the constants for the metal ion association with the folded and unfolded forms of the RNA, respectively. The reciprocal of the K_f is an apparent K_d for the metal ion association with the RNA that causes a stabilization effect. The apparent K_d from the thermal denaturation experiment was determined to be 166 ± 72 μM, which compares quite closely with the 147 ± 47 μM value obtained from the RT EPR binding isotherm. The EPR method provides direct information on the number and affinity of Mn^{2+} ions

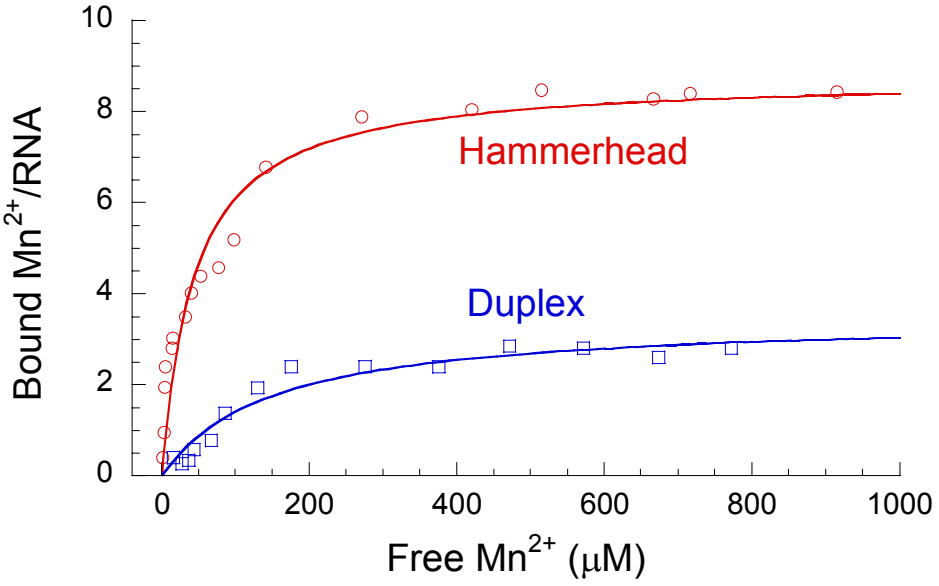

Figure 4-3: Room temperature Mn^{2+} EPR binding isotherms. Number of metals per RNA and an apparent K_d value are compared for the WT hammerhead (red) and the 13mer RNA duplex (blue). Conditions were 10 μM RNA concentration, 100 mM NaCl, 5 mM TEA, pH 7.8. Data for the hammerhead were taken from Horton and DeRose Biochemistry.

associated with the RNA duplex while, the UV melt method provides information on the Mn^{2+} ions ability to the stabilize the RNA strand. These results are expected for a simple RNA duplex without any specific metal ion-binding sites and are typical of non-specific association of the Mn^{2+} ions with the RNA molecule.

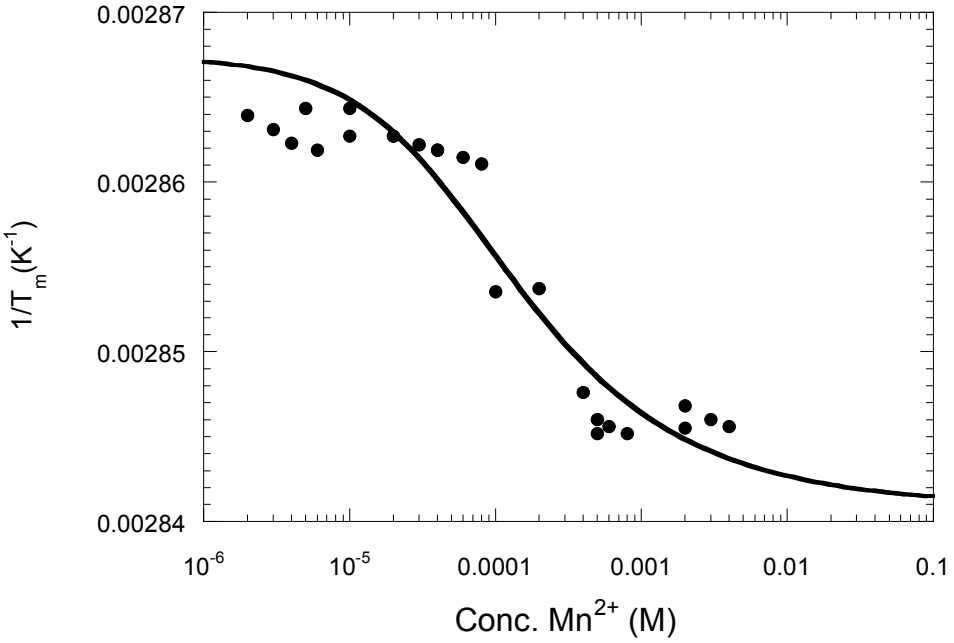

Figure 4-4: Mn concentration dependence on the melting temperature of the 13mer duplex. Apparent K_d values obtained by the UV melt method and the RT EPR titration method were compared. Conditions were 2 μM RNA, 100 mM NaCl, 5 mM TEA, pH 7.8

Low temperature EPR

The low temperature Mn^{2+} EPR spectra for the 1:1 Mn^{2+} to RNA complex are shown in Figure 4-5. For these samples the RNA and Mn^{2+} ion concentration was held constant at 250 μM in a buffer containing 100 mM NaCl, 5 mM TEA, pH 7.8 with 20% ethylene glycol as a cryoprotectant. The EPR spectrum for the WT hammerhead sample

shows a more pronounced feature on the 6th line compared to the standard, the Poly U, or the duplex (insert of Figure 4-5). This feature has previously been attributed to a signature of the Mn^{2+} ion coordinated at the high affinity site of the hammerhead and arises from slight changes in the zero field splitting parameters,[21] and is discussed in further detail in Chapter V.

To study the EPR signals for the interactions of multiple metal ions with the RNA molecules, the RNA concentration was held constant and samples were prepared with increased concentration of Mn^{2+} ions to achieve a 2:1, 3:1 and 4:1 Mn^{2+} to RNA ratio. Increasing the ratio of the equivalents of Mn^{2+} ions to RNA resulted in a broadening of the low temperature EPR spectrum for the hammerhead samples. This broadening is due to the Mn^{2+} ions being in multiple coordination sites each with their own unique spectrum super imposing on top of each other. A similar trend, although not as pronounced as observed for the hammerhead samples, is also seen for the Poly U and RNA duplex samples. The low temperature EPR spectra of the RNA samples containing multiple equivalents of Mn^{2+} ions, however, show no direct evidence for dipolar interactions between the Mn^{2+} ions and no evidence for the formation of a coupled dinuclear site in the RNA molecules.

Power saturation

From the crystal structure several Mg^{2+} ions have been observed coordinated in the conserved core of the hammerhead ribozyme and the results from the RT EPR binding isotherm shows evidence of approximately three tight Mn^{2+} ions coordinated to the hammerhead in 0.1 M NaCl. In order to determine if the sites populated under solution conditions are the same as those observed in the crystal structure, microwave

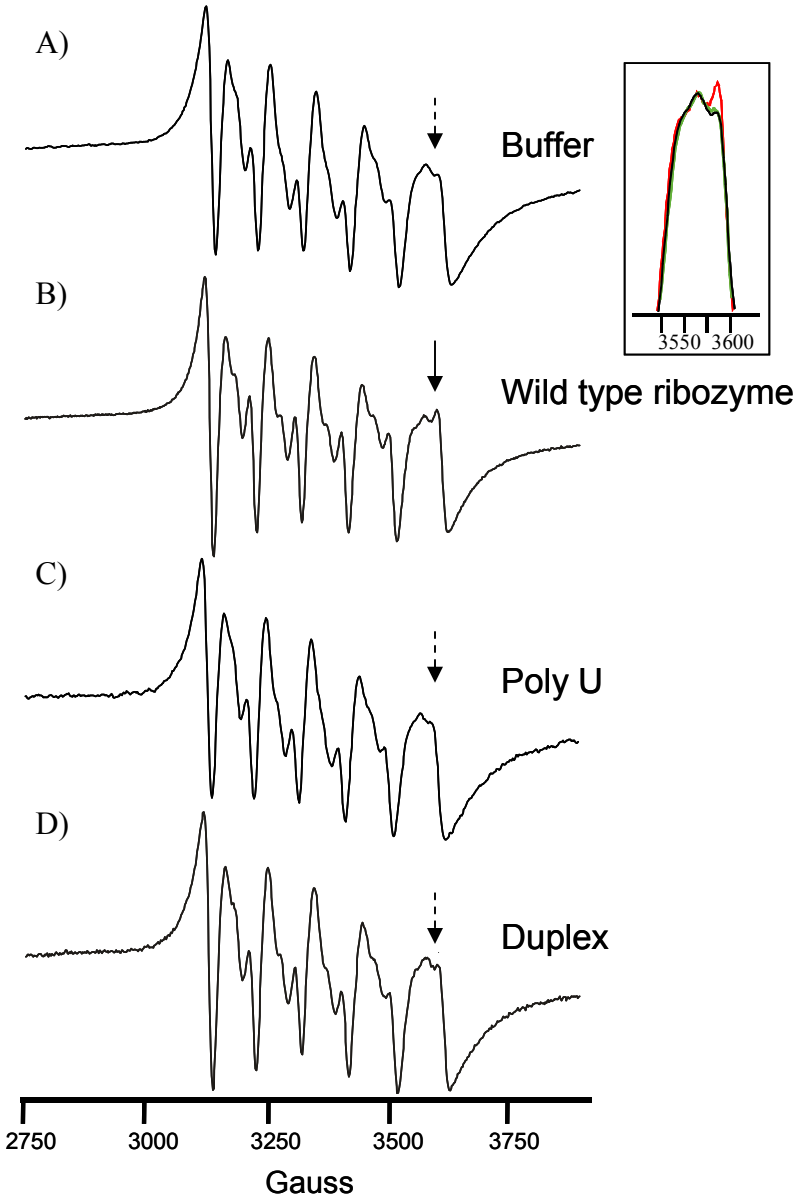

Figure 4-5: Mn EPR spectra of 1:1 metal:RNA complexes. The insert shows an overlay of the 6th line of WT hammerhead (red), standard (black) and duplex (green). Conditions were 250 μM RNA and Mn^{2+} concentrations in 100 mM NaCl, 5 mM TEA, pH 7.8, 20 % ethylene glycol, 0.2 mW microwave power at 10 K.

power saturation studies were performed. The incident power was incrementally increased from 0.02 mW to 63 mW for the 1:1, 2:1, 3:1 and 4:1 Mn^{2+} to RNA samples in order to observe any effects on the relaxation properties of the ions. The signal amplitude at each power is plotted as a function of the square root of the microwave power and is

shown in Figure 4-6. The power saturation studies of Mn^{2+} added to a solution containing only buffer were performed as a control to ensure that there was no Mn^{2+} concentration effects on the $P_{1/2}$ value.

The power saturation plots for the hammerhead show a dramatic change of the saturation behavior between the 1:1 and the 2:1 Mn^{2+}: HH samples. The hammerhead power saturation plot with only a single Mn^{2+} ion equivalent has a 34% reduction in the signal intensity between the maximum signal amplitude to the value obtained at the highest microwave power. The observed curve clearly changes shape for the 2:1 sample, which has a 20% reduction of the maximum signal intensity at the highest microwave power. The power saturation plots for the 3 and 4 equivalents samples of added Mn^{2+} ions are very similar, and have only a slight reduction of ~7% of the maximum signal intensity at the highest microwave power making the curves practically level after saturation. Comparing the results from the duplex and hammerhead samples clearly show a change in the saturation behavior of the Mn^{2+} ions at 3 and 4 equivalents of metal ions in the presence of only the hammerhead RNA and suggests additional relaxation processes between the ions. Fits of these data yielded the $P_{1/2}$ values and ε values for each sample. Increasing the number of Mn^{2+} equivalents to hammerhead results in an increase in the $P_{1/2}$ values with the 1:1 sample having a value of 1.4 mW and the 4:1 sample having a value of 5.1 mW (see Table 4-1).

The results for the Poly U hammerhead samples are different from those observed for the WT hammerhead samples. The 1:1 and 2:1 samples showed an approximately 25% reduction of the maximum signal intensity at the highest microwave power and little to no change in the $P_{1/2}$ value of roughly 3.0 mW for both samples. The 3:1 and 4:1

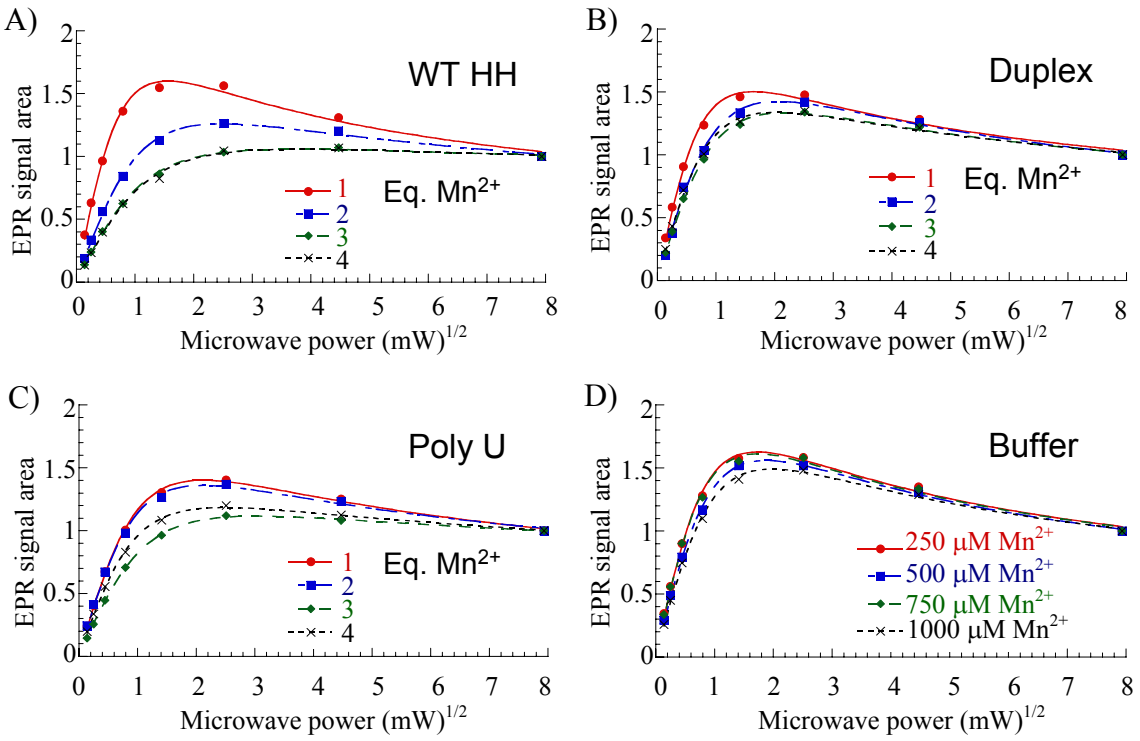

Figure 4-6: Mn^{2+} EPR power saturation plots for the RNA molecules and buffer. The results for the hammerhead show a less reduction of the signal amplitude for the 3:1 and 4:1 Mn:RNA samples. Conditions were 250 mM RNA concentration, 100 mM NaCl, 5 mM TEA, pH 7.8, 20% ethylene glycol at 20 K.

samples had a reduction of 17% and 15% of the maximum signal intensity to the highest microwave power, respectively. The $P_{1/2}$ value for the 3:1 Mn^{2+} to RNA was 4.3 mW, while the $P_{1/2}$ for the 4:1 was 3.0 mW. There is no apparent trend for the $P_{1/2}$ values obtained for the Poly U hammerhead and they were not as high as the values obtained for the wild type hammerhead. There seems to be some accumulation of Mn^{2+} ions in the Poly U, but these ions are not close enough to produce a significant relaxation effect between each other and can be attributed to this hammerhead mutant not being correctly folded.

The power saturation results for the duplex RNA shows very little change in the amount of signal reduction for all four concentrations of Mn^{2+} ions studied with a value

Table 4-1: Mn^{2+} power saturation values.

	$P_{1/2}$ (mW)			
Mn:RNA	Wild Type	Poly U hybrid	Duplex RNA	Buffer
1:1	1.4 ± 0.1	3.1 ± 0.2	1.7 ± 0.2	2.2 ± 0.2
2:1	3.2 ± 0.2	2.9 ± 0.2	3.0 ± 0.3	2.7 ± 0.1
3:1	4.8 ± 0.3	4.3 ± 0.1	3.0 ± 0.1	2.2 ± 0.2
4:1	5.1 ± 0.6	3.0 ± 0.2	2.4 ± 0.2	2.8 ± 0.2

	ε			
Mn:RNA	Wild Type	Poly U hybrid	Duplex	Buffer
1:1	0.70 ± 0.02	0.71 ± 0.02	0.68 ± 0.02	0.74 ± 0.02
2:1	0.66 ± 0.02	0.68 ± 0.03	0.71 ± 0.02	0.75 ± 0.02
3:1	0.57 ± 0.01	0.61 ± 0.02	0.68 ± 0.01	0.73 ± 0.03
4:1	0.57 ± 0.03	0.62 ± 0.02	0.66 ± 0.01	0.73 ± 0.02

of 32% for the 1:1 and a value of 25% for the 4:1 Mn:RNA samples. Compared to the results for the samples prepared of the same Mn^{2+} ion concentrations in just buffer, the overall shapes of the curves and the obtained $P_{1/2}$ values are quite similar for Mn2+ added to the RNA duplex. The amount of signal reduction was nearly constant at an average value of 35% ± 2% for all four concentrations of Mn^{2+} ions. The power saturation plots for the buffer samples showed a range of $P_{1/2}$ values of 2.2 to 2.8 mW while the RNA duplex had a similar range of 1.7 to 3.0 mW, without any specific trend. These results lead to the conclusion that changes observed in the power saturation behavior of the hammerhead system must solely arise from the Mn^{2+} ions directly interacting with the RNA molecule.

Line broadening

The value of the homogeneity factor, ε, reflects the extent and type of interaction responsible for the line broadening of the EPR signal. The degree of inhomogeneity is

influenced by a number of factors including hyperfine interactions, anisotropy of the spin level splittings, dipolar interactions with spins of different Larmor frequencies, inhomogeneities in the applied magnetic field, and the population of multiple sites.[86,87] Values for ε range from 1.5 for homogeneous broadening to 0.5 for inhomogeneous broadening.

The ε value for the 1:1 hammerhead was 0.70 indicating the presence of inhomogeneous line-broadening effects. As the ratio of the Mn^{2+} ions to RNA increased to 3 and 4 equivalents the ε value decreased to 0.56 indicating stronger inhomogeneous line broadening effects on the EPR signal. This decrease in the ε value may arise from the EPR signals for the three and four Mn^{2+} ions in different coordination environments when bound in the hammerhead that are averaged in the resulting spectrum. This notion is supported by the nearly constant ε value, within error, of 0.74 for the four concentrations of Mn^{2+} in buffer without RNA present. The ε values for the RNA duplex had a value of approximately 0.68 for all four samples indicative of a nearly uniform coordination environment for each of the interacting Mn^{2+} ions, which are most likely fully hydrated ions not associating specifically with the RNA molecule. The Poly U hammerhead mutant had a ε value of 0.71 for the 1st added Mn^{2+} ion, which is similar to that of the wild type hammerhead. At the highest Mn^{2+} ion concentrations the Poly U sample had a lower ε value of 0.62, which is a decrease but is not as low as the value seen for the wild type hammerhead sample at the same concentration.

Conclusion

Changes in the relaxation properties observed by the power saturation of multiple Mn^{2+} ions coordinated in the hammerhead can be used to determine the relative

proximity of the ions in the RNA. In order for the Mn^{2+} ions to provide relaxation effects between each other they must be close enough to each other to allow energy exchange between the spins. The EPR microwave power saturation technique provides information on the relaxation times (T_1 and T_2) of the Mn^{2+} ions. Having several metal ions of the same type in different coordination sites makes it extremely difficult to obtain an exact distance measurement between the Mn^{2+} ions from the power saturation method. Success in distance determination using power saturation techniques has been achieved between the Cu and Fe ions found in cytochrome oxidase.[88]

The power saturation results for the hammerhead samples show an increase in the $P_{1/2}$ value as the Mn^{2+} to RNA ratio increases. The highest $P_{1/2}$ value is obtained when there are four equivalents of Mn^{2+} ions to the RNA. This increase in the $P_{1/2}$ value is consistent with the four Mn^{2+} ions being in close proximity providing additional relaxation pathways for each other. These results can be interpreted with the hammerhead creating specific metal ion- binding sites and suggests that these sites are similar to those observed in the crystal structure. It has been previously determined that under 1 M NaCl the A9/G10.1 site binds a Mn^{2+} ion with high affinity and has a unique EPR spectrum. The 1:1 Mn^{2+} EPR spectrum for the lower salt conditions used in these experiments (100 mM NaCl) has the same unique features, which shows that the A9/G10.1 site is the first metal ion site populated in the hammerhead even at low salt concentrations. The addition of a second equivalent of Mn^{2+} to the hammerhead incurs only a modest increase in the $P_{1/2}$ value indicating the metal ions are still quite distant from each other. The biggest change in the $P_{1/2}$ value is observed with the addition of the 3^{rd} equivalent of Mn^{2+} ions indicating that on average, the bound metal ions are relatively

close. The addition of the 4th equivalent of Mn^{2+} ions has only a slightly greater $P_{1/2}$ value that may arise from a slightly farther interaction. The crystal structure of the hammerhead shows several metal ion-binding sites that are roughly 10 Å and one that is nearly 20 Å away from the A9/G10.1 site. The results here may be interpreted as the A9 site being occupied first, followed by a second site farther away, perhaps near the cleavage site or stem I. The third site is relatively close to the second ion near stem I, causes the sudden increase in the $P_{1/2}$ value with the fourth metal ion site a little farther away and perhaps at the G5 location. The exact coordination sites of the second, third and fourth Mn^{2+} ions in the hammerhead, however, are not obvious and may in fact be inconsistent and not populate the same site or bind in a specific order making assignment of the metal ion binding sites difficult.

Although EPR methods can determine the properties of the Mn^{2+} ions directly associated with the hammerhead, it proves difficult in determining the roles of non-specific binding or the electrostatic roles the metal ions may have. This made a comparison of an RNA system with a complex structure like the hammerhead with a simple RNA duplex a necessity. The duplex RNA sequence does not contain any specific coordination sites for Mn^{2+} ions based on the RT EPR binding isotherms and this is reflected by the minimal effect of adding Mn^{2+} ions on the power saturation results. The interactions of Mn^{2+} ions with the duplex RNA, which has a higher apparent K_d value compared to the tight sites in the hammerhead, is mainly electrostatic in nature and the ions are expected to be mostly hydrated. This higher K_d value for the RNA duplex is consistent with the K_d value obtained for the set of weaker metal ion binding sites observed in the hammerhead. This suggests that this class of site in the hammerhead

arises from the non-specific interaction of Mn^{2+} ions with the helical parts of stem I and III. The apparent K_d value for the duplex is comparable to a value obtained for a single Mn^{2+} ion coordinated to $tRNA^{phe}$ with a 170 μM K_d value (in 0.17 M NaCl) that was determined to have only one direct bond with the RNA molecule.[18] The closeness in the apparent K_d values obtained for the RNA duplex by EPR binding isotherms and UV melt profiles show that the Mn^{2+} ions associating with the duplex are having only a slight stabilizing effect on the molecule.

Determination of whether a metal ion interacts with RNA in a specific or non-specific interaction is fundamental to determining the roles that cations play in RNA function. The hammerhead crystal structure shows several potential metal ion-binding sites but it has not been clear if these sites are also occupied under solution conditions. Here, low temperature EPR studies, especially the power saturation technique, were able to provide confirmation that multiple Mn^{2+} ions in close proximity are coordinated to the hammerhead under solution conditions and this is consistent with the sites observed in the X-ray crystal structure. These results, however, have not determined the exact location of the metal sites and further mutational studies would be needed to probe the identity of potential metal ion binding sites besides the A9/G10.1 position.

CHAPTER V

SPECTROSCOPIC STUDIES OF MODELS FOR METAL-RNA INTERACTIONS

Introduction

The use of spectroscopic techniques to study metal-RNA interactions provides a useful avenue to probe the types of interactions that can be achieved in large RNA biomolecules. The two general approaches available to study metal-RNA interactions are either to observe changes in the RNA that occur when a metal ion interacts, or to use spectroscopically active metal ions to probe local RNA structure. As a mimic for interactions of Mg^{2+} ions, Mn^{2+} has been used in numerous EPR studies to measure its interaction with RNA molecules.[19-21,62] Mn^{2+}-protein interactions have been extensively studied by EPR techniques and this provides a solid foundation for their application to RNA systems.

Many simple small Mn^{2+} complexes with nucleotides and phosphate containing groups as well as other ligands have been extensively studied by EPR techniques. The understanding of how Mn^{2+} ions interact with large RNA molecules, however, is not as advanced and observed spectroscopic signatures or trends are not well defined for these systems. The EPR spectral lineshape[89] and zero field splitting (zfs) parameters of a Mn^{2+} ion can play a crucial role in identifying the geometry of the bound ion as well as providing other information about the coordination site.[57] Changes in the ligands or geometry around the Mn^{2+} ion will affect the zfs of the metal and the EPR spectrum is altered by changes in the splitting pattern of the M_s levels.

Simulations can provide information on the various parameters contributing to the overall shape of an EPR spectrum. Manganese EPR spectra are difficult to simulate due to the S = 5/2 and the I = 5/2 values of the Mn^{2+} ion. To complicate this even further is the presence of forbidden transitions of $|M,m> \leftrightarrow |M-1, m \pm 1>$ that occur in pairs between the allowed hyperfine lines and that are commonly observed at X-band frequencies. The intensity and positioning of these forbidden transitions are directly related to the magnitude of the zfs value D, and can be used to determine the degree of distortion of the Mn^{2+} ion.[55,90]

Various methods have been used to simulate EPR spectra by either using perturbation theory or solving the complete Hamiltonian. Spectra of simple S = ½ spin systems can be readily simulated by using perturbation theory such as implemented in the Bruker SimFonia program. Perturbation theory uses approximation of the energy eigenvalues and eigenvectors to solve the spin Hamiltonian. This calculation is relatively quick and straightforward and most accurate when the electronic Zeeman interaction is dominant and is at least 10 times greater than the hyperfine interaction. Perturbation theory breaks down when these values are too close, but can still yield a relatively good understanding of the EPR spectrum. Another drawback in using perturbation theory is the lack of accurately reproducing higher order effects as well as forbidden transitions. Solving the complete Hamiltonian is more calculation intensive, but more accurately reproduces complex EPR spectra.

Previously, several simulations have been performed of Mn^{2+} aqua samples in order to determine the D value. Tan *et al*.[91] have performed simulations and have determined that the central six-line pattern arises primarily from the $| -½ > \rightarrow | +½ >$ EPR

transitions. The presence of zero-field splitting broadens the EPR spectrum with the wings of the spectrum containing a significant contribution from the ± 3/2 and ± 5/2 spin manifolds. These simulations used a D value of –198 G and yielded a reasonably accurate portrayal of the experimental ESE-EPR spectrum.

Coffino and Peisach used a full spin-Hamiltonian approach to simulate a CW Mn^{2+} EPR spectrum.[92] This method is an improvement over perturbation theory and more effective at fitting the zfs term. Coffino and Peisach simulated the EPR spectrum of a Mn^{2+} aqua sample using the D value of 198 G used by Tan[91] and also used a D value of 155 G that included an E/D ratio of 1/3 to account for the nonaxial system of the Mn^{2+} aqua complex. The inclusion of the E value in the simulation more accurately resembled the observed EPR spectrum and the results implied that the higher order contributions from the ± 3/2, 5/2 spin levels have less of an effect than that determined by Tan.

In this Chapter the origin of the unique Mn^{2+} EPR spectrum found for the high affinity hammerhead site is explored using model complexes and EPR simulations. Understanding how the coordination site in the RNA produces the Mn^{2+} EPR spectrum of the high affinity site in the hammerhead ribozyme will provide information on how this site affects the coordination of metal ions as well as an understanding how Mn^{2+} ions are interacting with other RNA molecules. The interactions of Mn^{2+} ions with nucleotide ligands consisting of single nucleotides with a monophosphate group, GMP or a triphosphate group, GTP also were studied. The effect of changes in the geometry of the Mn^{2+} ion were also studied using high Cl^- ion concentrations. Simulations of the hammerhead and buffer EPR spectra were also performed to determine the zfs parameters of the Mn^{2+} ion. The results of these EPR studies involving the hammerhead ribozyme

and the model complexes can be used as a paradigm for application to other Mn-RNA systems.

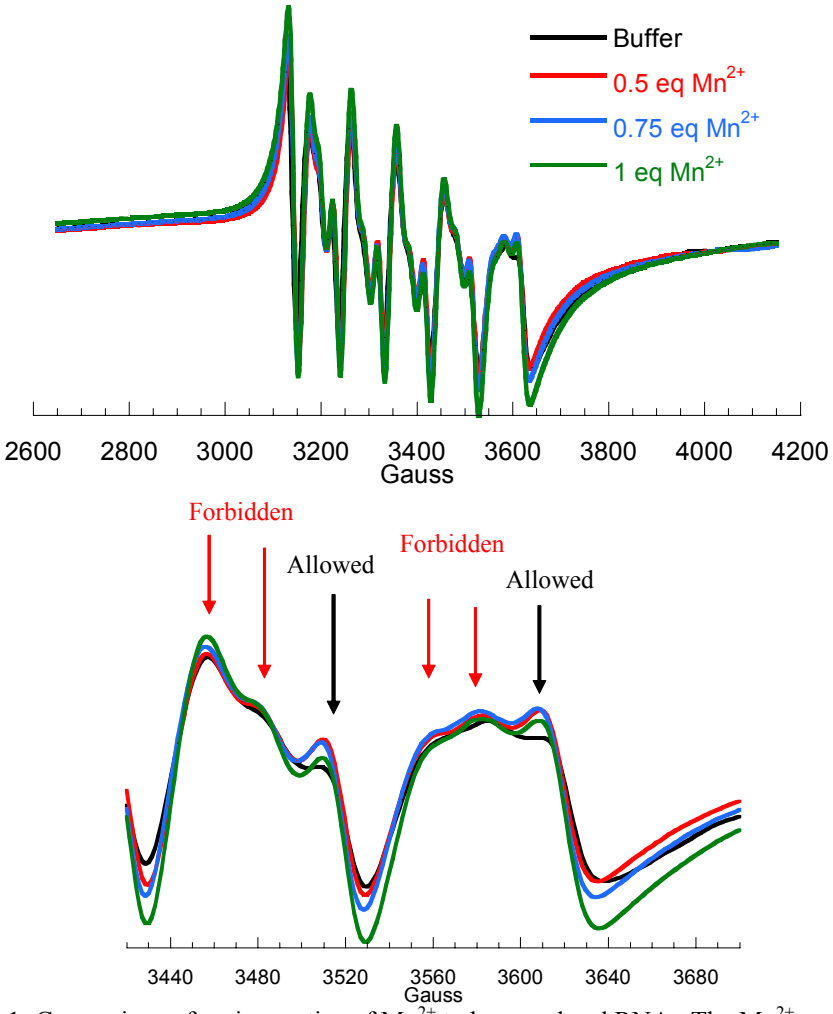

Figure 5-1: Comparison of various ratios of Mn^{2+} to hammerhead RNA. The Mn^{2+} concentration remained constant at 250 μM as the RNA concentration was increased to make the desired ratio. The bottom panel shows an overlay of the 5th and 6th line and the black arrows denote the changes in the allowed line as the Mn to RNA ratio is varied. Red arrows are forbidden transitions. Conditions were 1 M NaCl, 5 mM TEA, pH 7.8 at 10 K.

Results and discussion

Homogeneity of the Mn^{2+} high affinity site in the hammerhead

To determine the homogeneity of the high affinity site in the hammerhead ribozyme EPR spectra were obtained at sub-stoichiometric equivalents of Mn^{2+} ions to

ribozyme EPR spectra were obtained at sub-stoichiometric equivalents of Mn^{2+} ions to RNA. Samples with Mn^{2+} to hammerhead ratios of 0.5, 0.75, and 1 Mn^{2+} equivalents to RNA were prepared and the resulting EPR spectra are overlayed in Figure 5-1 along with a Mn^{2+} standard of the same concentration. The allowed and forbidden transitions are denoted in the EPR spectrum where the forbidden lines arise in pairs between the allowed transitions. The allowed lines are more defined in all the hammerhead samples compared

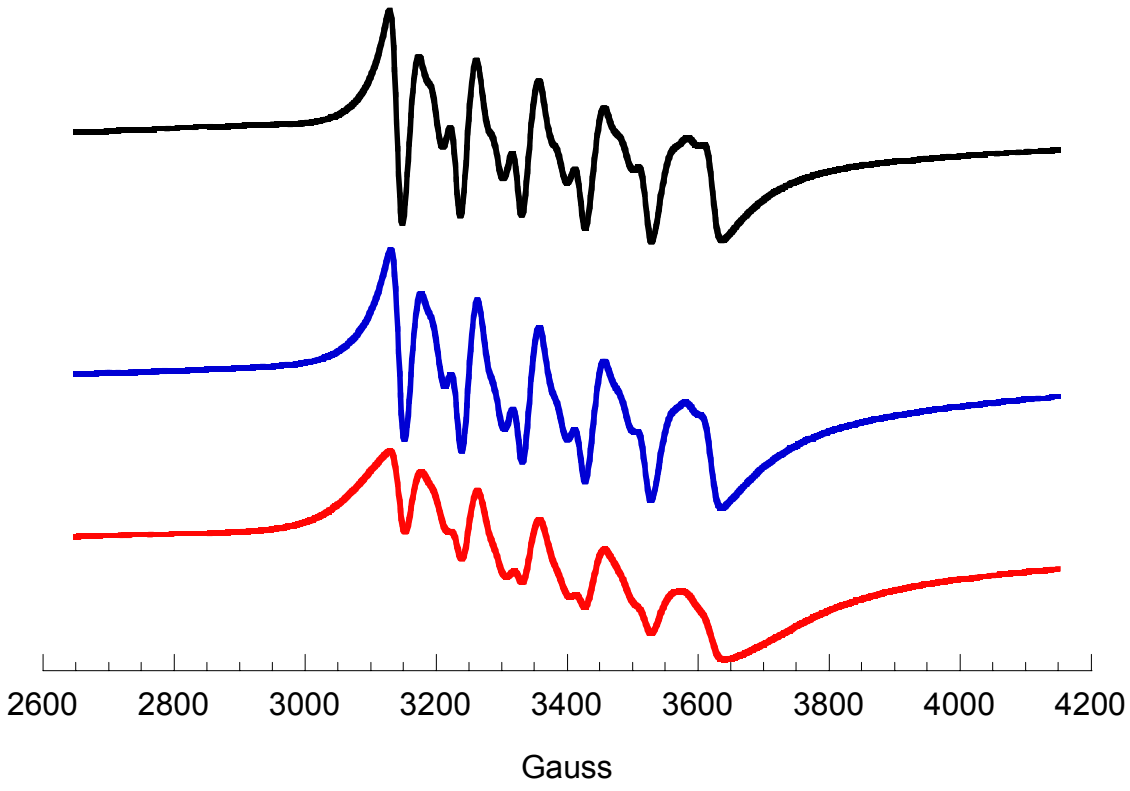

Figure 5-2: Mn^{2+} EPR spectrum of a series of mimics for metal-RNA interactions. The EPR spectra show an increase in signal broadening down the series of molecules. Conditions were 500 mM Mn^{2+}, 20 % ethylene glycol, X-band, 10 K.

to the standard, and the enlargement of the 5^{th} and 6^{th} lines shows this difference more clearly. The 6^{th} line feature is most prominent for the 0.75 and 0.5 equivalents of Mn^{2+} to

hammerhead samples. The sharper lines obtained for the lower ratios of Mn^{2+} ions to RNA suggest that a greater population of the metal ions are coordinated at the high affinity site. These results may be due to a small population of misfolded conformations of the hammerhead that are not active, which is consistent with the maximum percent activity of ~ 70% that is typically observed.

EPR of small model complexes

In an attempt to understand the effect that different coordination environments have on the Mn^{2+} EPR spectra, a series of different model complexes was studied. Several small Mn-complexes were prepared containing 0.5 mM Mn^{2+} in just H_2O, 2.5 mM 5'-GMP or 2.5 mM 5'-GTP with 20% ethylene glycol as the cryoprotectant (Figure 5-2). The EPR spectra show a dramatic broadening of the lineshape along this series of complexes, which is consistent with the Mn^{2+} ion coordinating these molecules. The Mn-GMP crystal structure shows the Mn^{2+} ion to be directly coordinated to the N7 position of the guanine with 5 water molecules and to have a through-H_2O interaction with the phosphate group.[73] Compared to the standard there is only a minor change in the lineshape of the EPR spectrum, consistent with a single type of coordination site for the Mn^{2+} ion to the GMP molecule. The lineshape of the EPR spectrum for the Mn-GTP complex shows the most broadening and is consistent with a multiply coordinated Mn^{2+} ion with lower symmetry. The EPR spectrum for a Mn-EDTA complex should be noted as being extremely distorted at X-band frequencies.

A)

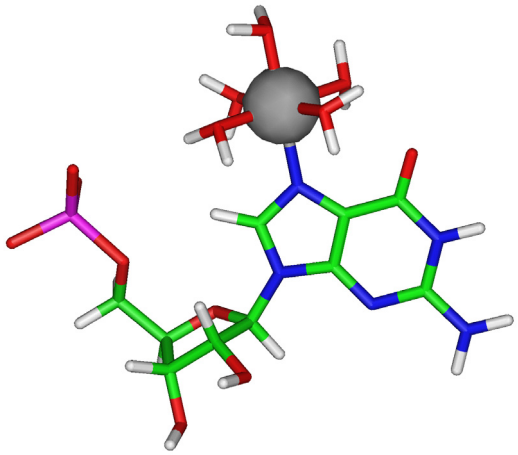

B)

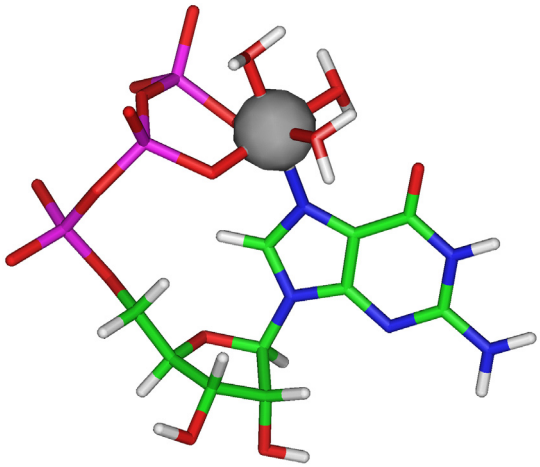

Figure 5-3: Coordination of Mn^{2+} to small complexes. A) Mn-GMP B) possible coordination of Mn-GTP. Models were constructed and energy minimized in Cerius2.

Proposed coordination models for these complexes are shown in Figure 5-3 and are based on the EPR results as well as results from a combination of other experiments. Although none of these complexes reproduces the EPR spectrum observed for the hammerhead ribozyme high affinity metal site, they do show a general trend. The line broadening of the Mn^{2+} EPR spectra can be explained as a combination of several factors.

As the number of ligands coordinating to the metal ion increases the symmetry of the complex decreases. The standard, or hexaqua Mn^{2+} complex, has virtually O_h symmetry and an overall uniform ligand environment. The Mn 5'-GMP complex has the addition of a nitrogen ligand that changes the symmetry to C_{4v} as well as the electronic structure around the Mn^{2+} ion. For the 5'-GTP complex, the Mn^{2+} ion has the most distorted EPR spectrum with virtually no symmetry elements having C_s symmetry. The exact Mn^{2+} coordination in the Mn-GTP complex is not clear and the Mn^{2+} ion most likely has multiple coordination modes between the different phosphate groups. The broadened EPR spectrum is a result of strains of the g and D values arising from what are essentially small deviations in the geometry, bond lengths and angles of the Mn^{2+} ions that yield a range, although small, of values that are superimposed in the spectrum.

Another avenue towards understanding the effect that the geometry around the Mn^{2+} ion has on the EPR spectrum was pursued by adding high levels of chloride ligands to a methanol solution. At high concentrations Cl^- ions will replace bound solvent molecules around the Mn^{2+} ions. In aqueous solution the Mn^{2+} ion will maintain a six-coordinate environment, but in non-aqueous solvents like acetonitrile and methanol the geometry around the Mn^{2+} ion will become four-coordinate.[93] To determine the concentration of Cl^- ions needed to change the EPR signal and produce T_d symmetry around the Mn^{2+} ion, the RT EPR spectra were monitored as the concentration of LiCl was increased. The initial addition of LiCl yielded a decrease in the EPR signal intensity in comparison with a standard sample, which is consistent with a mixed coordination sphere of $[Mn(Cl^-)_x(MeOH)_{6-x}]^{2-x}$ causing the EPR signal to broaden and lose apparent intensity (Figure 5-4). At higher LiCl concentrations, the EPR signal intensity begins to

increase and broadens. This effect has been previously observed and attributed to the formation of a tetrahedral Mn^{2+} species.[94] The low intensity of the room temperature Mn^{2+} signal of the 3 M LiCl sample compared to the standard indicates that a small portion of the Mn^{2+} ions are in T_d symmetry and the rest are in a mixed coordination with Cl^- and MeOH ligands.

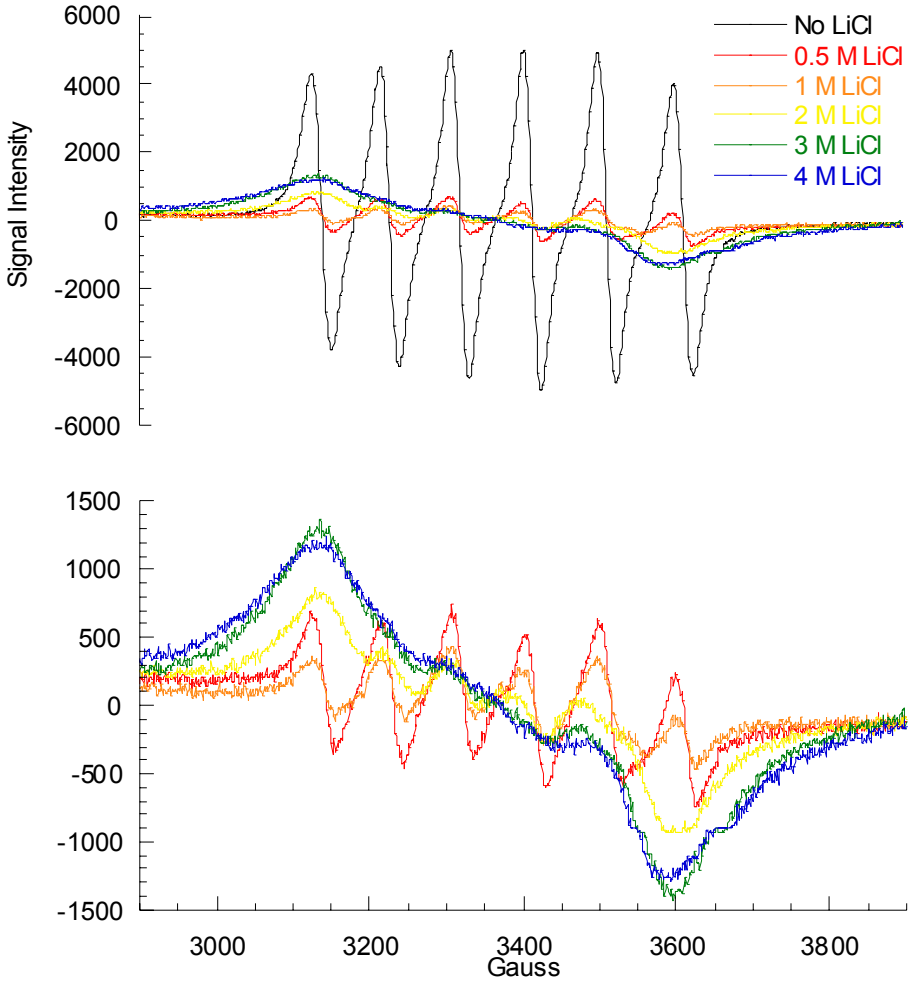

Figure 5-4: RT Mn^{2+} EPR titration of LiCl in methanol. Increasing the Cl- concentration replaces coordinated MeOH groups and produces mixed coordinate species that decrease the EPR signal intensity. When all MeOH is replaced, the signal intensity increases and broadens indicative of a new complex forming. Conditions were room temperature solution of 500 μM Mn^{2+} in methanol, X-band, 25 G modulation amplitude, 0.2 mW microwave power.

The low temperature Mn^{2+} EPR spectrum for 3 M LiCl in methanol shows very sharp and well defined allowed transitions when compared to the standard in methanol (Figure 5-5), has also been previously observed.[90,95] These features are more prominent on the 5th and 6th lines of EPR spectrum and are quite similar to those observed in the hammerhead ribozyme high affinity Mn^{2+} site.

The changes in the EPR lineshape for the Mn-complexes studied here can be explained by changes in the coordination sphere of the Mn^{2+} ion. The electron density around the Mn^{2+} ion is affected by the interactions of the d e^- with the e^- from the ligands. Even a slight change in the electrostatics by having more than one type of ligand causes the six-fold degeneracy of the ^6S Mn^{2+} ion to split the spin levels by the addition of the

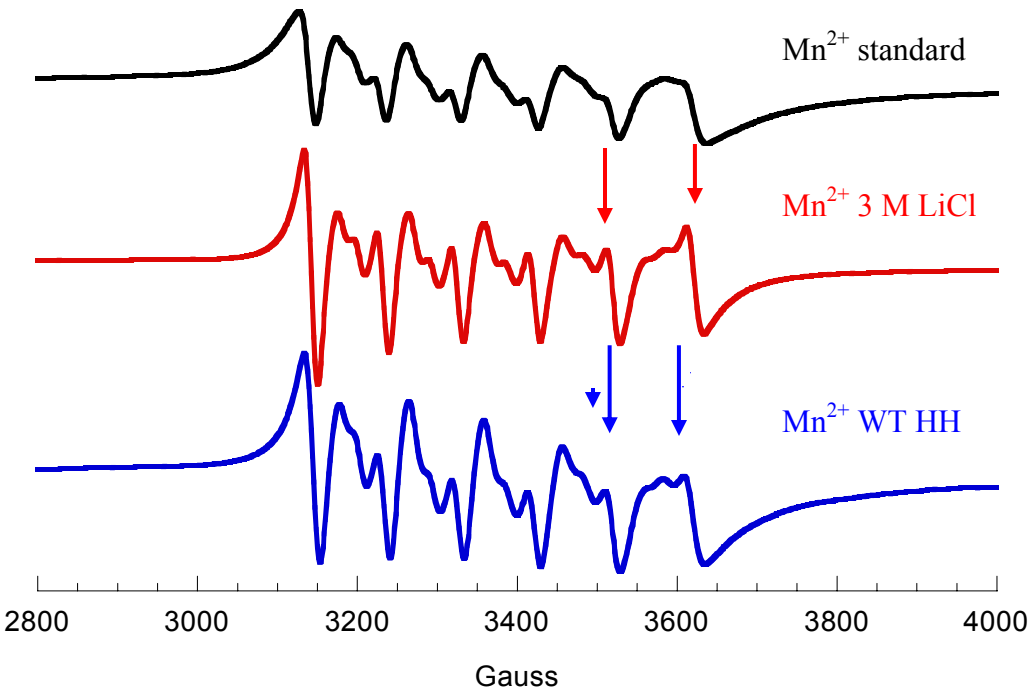

Figure 5-5: Mn^{2+} EPR spectra comparison. The black spectrum is a Mn^{2+} standard in methanol, red Mn^{2+} in 3 M LiCl and blue is Mn^{2+} WT hammerhead. The arrows indicate changes of the allowed lines of the 5th and 6th EPR line. Conditions were 500 μM Mn^{2+}, MeOH, 10 K, X-band, 0.2 mW microwave power.

zfs parameter D and affects the EPR spectrum.[57]

Estimates of the D value for Mn^{2+} complexes with Cl^- ligands in methanol have a range of 80 to 150 gauss depending on the site and the sharpness of the spectrum.[96] The observed changes in the Mn^{2+} EPR spectra of the high Cl^- and hammerhead samples are due to a change in the coordination environment of the Mn^{2+} ion that alters the D value. This symmetry change is evident by the forbidden transitions either changing relative position or intensities and results in the allowed lines being better resolved in the EPR spectrum.

A literature search for Mn^{2+} EPR spectra obtained with various complexes shows examples of complexes that are similar to what has been observed for the hammerhead high affinity site. One such example is a seven coordinate Mn^{2+} species that also has an EPR spectrum with a sharpening in the allowed lines.[97]

The D value can be estimated directly from the EPR spectrum by various methods. Misra has developed a method using the separation of the forbidden transitions to calculate the D value.[98] Allen has used a different method to calculate D from the relative intensity of the hyperfine lines.[90] Both techniques are useful, but may be hindered by either the forbidden lines or the allowed lines being unresolved in the EPR spectrum. For the EPR spectra obtained in this study an attempt to use the separation of the forbidden lines was first made. This method, however, gave inconsistent results due to the poor resolution of the forbidden lines. The method developed by Allen was used and a ratio of the intensity of the 6^{th} and 5^{th} allowed lines was calculated.

The Mn^{2+} EPR spectra for the hammerhead high affinity site show the most pronounced change in the lineshape of the 6^{th} and 5^{th} lines making the use of this

comparison ideal. Several EPR spectra were analyzed by this method for samples containing Mn^{2+} in buffer, in the presence of various ratios of hammerhead RNA, GMP and in the presence of 3 M LiCl. The ratios obtained are plotted in Figure 5-6 and show a significant trend in the results. The buffer samples have an average value of 1.27, and all the hammerhead samples yielded a value between 1.10 and 1.20, lower than the buffer value. The GMP sample, which showed slight broadening of the EPR spectrum compared to the buffer sample, had a higher ratio value of 1.33. Interestingly, the 3 M

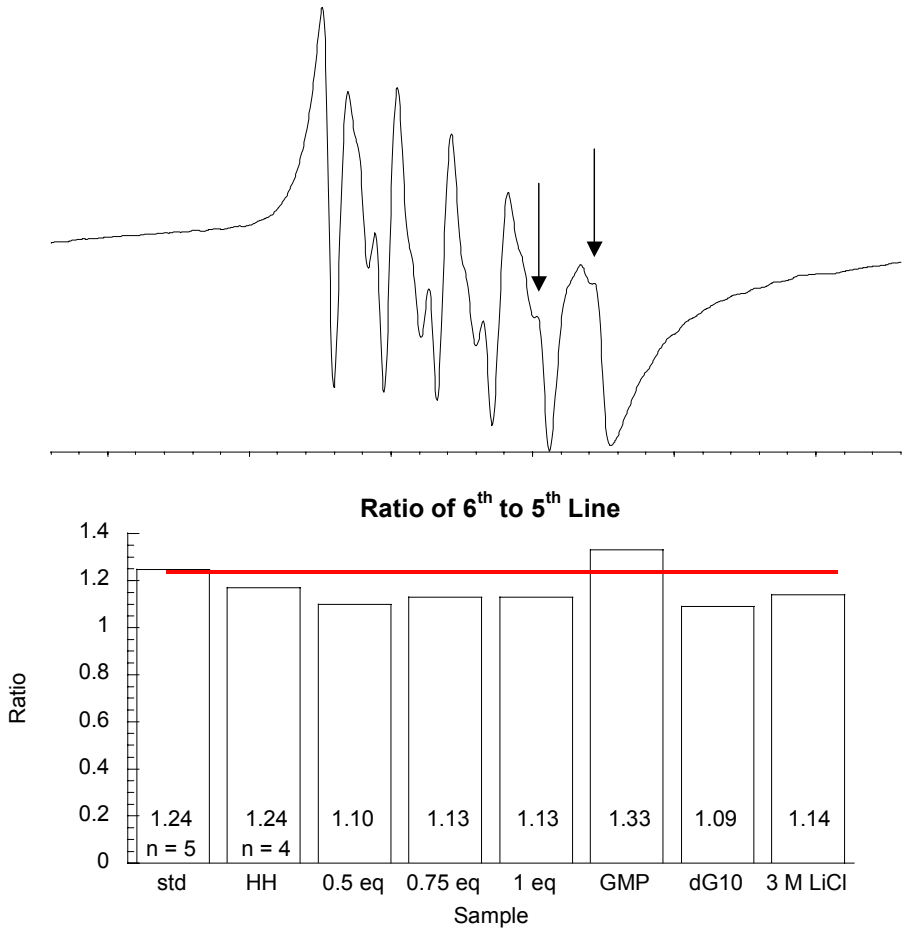

Figure 5-6: Ratios of allowed hyperfine lines from various Mn^{2+} samples. The intensity of the 6th to the 5th lines is compared as shown in the arrows on the EPR spectrum. The red line indicates the average value for Mn^{2+} standard and the number of spectra is 1 except as noted for the n value. Conditions were 250 μM Mn, 1 M NaCl, 5 mM TEA, pH 7.8, 20% ethylene glycol, spectra taken at 10 K and 9.4 GHz.

LiCl sample had a ratio of 1.14, similar to that obtained for the hammerhead samples which suggests a similar value for the zfs.

EPR simulations

To determine the theoretical origin of the distinctive lineshape for the observed EPR spectra of the high affinity Mn^{2+} ion-binding site in the hammerhead ribozyme, EPR simulations were performed using the MatLab based program EasySpin. The program solves the full spin Hamiltonian and can be used to simulate forbidden transitions as well as include higher order effects that appear in experimental spectra. EasySpin also allows for the inclusion of strains for various parameters, such as A, g and D, which better simulates slight broadening of the EPR spectra arising from small sight-to-sight variations in the coordination sphere of the Mn^{2+} ions.

All EPR experimental and simulated spectra were normalized to the highest peak intensity and superimposed for comparison purposes. Particularly of interest was matching the relative intensities of the allowed and forbidden transitions of the 6^{th} line of the EPR spectrum for the hammerhead high affinity site and buffer samples. Comparisons were also made to ensure that the intensities of the forbidden and allowed transitions of the other lines also matched reasonably well.

The EPR spectral simulations were initially started with parameters used by Coffino and Peisach.[92] The main parameters of interest were a D value of 465 MHz and an E value of 155 MHz that were used to simulate EPR spectrum of a Mn^{2+} aqua complex. Although the simulated spectrum using these parameters was in general agreement with the experimental spectrum for the hammerhead high affinity site, the relative intensities of the 6^{th} line did not match well. Since the positions of the forbidden

transitions are dependent on the D value, EPR spectra with a range of D values from 400 to 600 MHz with E/D equal to 1/3 were simulated and some examples are shown in the Appendix Figure A-2. At low D values below 400 MHz the allowed transitions of the 6^{th} line is too intense compared to the hammerhead spectrum. Conversely, at a high D value of 600 MHz the forbidden and allowed transitions become too distorted and begin to broaden the spectrum too much. Simulated spectra with a D values in the range of 500 – 530 MHz had relative intensities that gave the closest match to the hammerhead spectrum. The best match between the simulated and experimental spectra of the relative intensities of the allowed and forbidden transitions of the 6^{th} line was determined to be with the D value of 520 MHz and the E value of 173 MHz (E/D = 1/3) (Figure 5-7).

The simulations of the Mn^{2+} buffer spectrum held all parameters the same and varied the E value. As the E parameter became lower, indicating less rhombic distortion of the EPR spectrum, the relative intensities of the 6^{th} line were altered and matched the buffer spectrum at a value of 90 MHz. The inclusion of a slight A strain broadened the simulated spectrum and matched the experimental spectrum.

Lowering the E value decreased the relative intensities of the forbidden and allowed transitions of the 6^{th} line of the Mn^{2+} EPR spectrum. The Mn^{2+} buffer spectrum compared best with an E value of 90 MHz (E/D ~ 1/5), roughly half the E value obtained for the hammerhead (Figure 5-8). The simulation parameters for both spectra are shown in Table 5-1. The inclusion of a very slight A strain in the simulation broadens the spectrum slightly and better replicates the 6^{th} line of the observed spectrum for the buffer. Including the same A strain value for the hammerhead simulations has a slight broadening effect on the 6^{th} line feature and matches closely with the spectrum observed

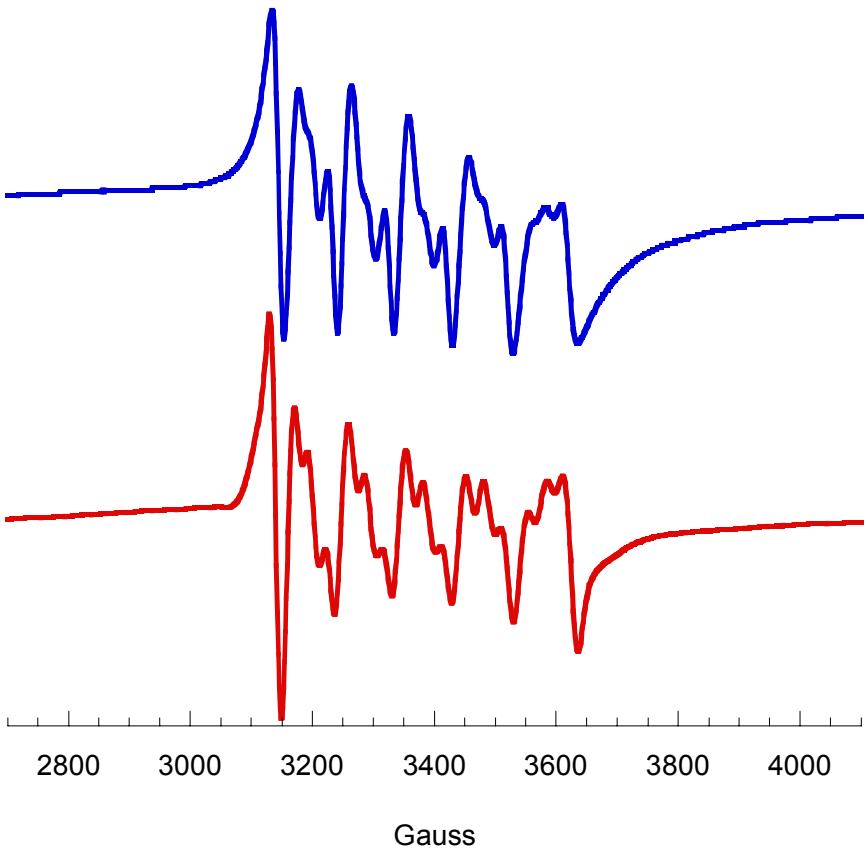

Figure 5-7: Simulation of the Mn^{2+} high affinity hammerhead EPR spectrum. The top spectrum is the 0.5 equivalent Mn^{2+} to hammerhead sample and the bottom is the simulated spectrum. Simulation were performed with EasySpin with the parameters of D = 520 MHz, E = 173 MHz, linewidth 15 G.

for the 1:1 Mn to hammerhead and the dG10.1 hammerhead samples. Simulations of the GMP and GTP samples were only partially attempted due to the broad EPR lines indicating the possible presence of multiple coordination modes.

Conclusion

The subtle changes in the EPR spectra for the sub-stoiciometric ratios of Mn to hammerhead investigated here show that with careful observations of the lineshape a more accurate understanding of the Mn ion coordination site can be achieved. Since

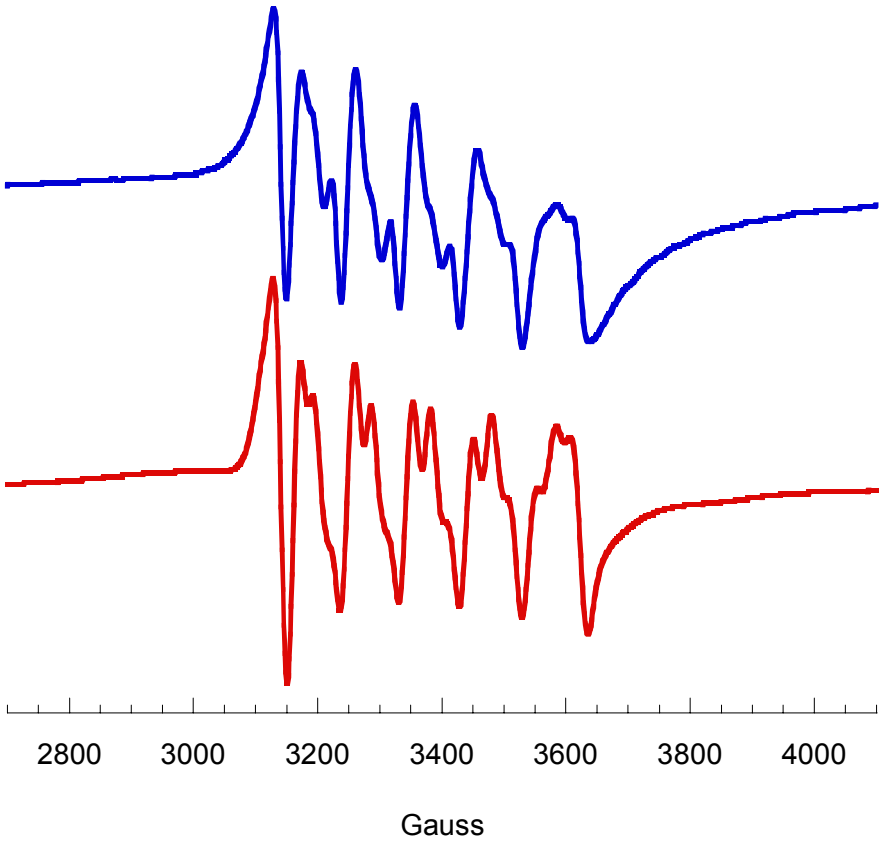

Figure 5-8: Simulation of the Mn^{2+} buffer EPR spectrum. The top spectrum is Mn^{2+} in buffer sample and the bottom is the simulated spectrum. Simulation were performed with EasySpin with the parameters of D = 520 MHz, E = 90 MHz, linewidth 15 G, A strain of 0.05.

many spectroscopic techniques detect all of the observable metal ions it is a good precaution to ensure a homogeneous population for the desired site of study. The Mn^{2+} EPR spectra of the model complexes show definite changes in the linewidths as the coordination sites increase. The spectra for the Mn-GMP and Mn-GTP complexes do not mimic the spectrum observed for the high affinity site in the hammerhead, but provide information on possible other coordination sites in RNA molecules.

EPR spectral simulations are a useful technique to determine the parameters of the Mn^{2+} ion producing an EPR spectrum. Comparison of the determined parameters for the

Table 5-1: EPR simulation parameters of the hammerhead and buffer spectra.

	Hammerhead	Buffer
g	2	2
A	270 MHz	270 MHz
D	520 MHz	520 MHz
E	173 MHz	90 MHz
D strain	1	1
A strain	0	0.05

simulations of the hammerhead spectrum and buffer spectrum indicated a higher E value for the hammerhead sample. The unique EPR spectral signature observed for the high affinity hammerhead site arises from a greater rhombic distortion of the Mn^{2+} ion compared to the buffer sample and is consistent with the modeled site, which includes coordination to the N7 of a guanine residue, a phosphate oxygen and four water molecules. This bidentate type of coordination found in the hammerhead causes more rhombic (E) distortion of the geometry of the Mn^{2+} ion than the buffer sample surrounded by six water molecules.

The EPR simulations have provided a definitive answer to the exact role that Mn^{2+} ion coordination to the hammerhead has to in producing the observed signature EPR spectrum characteristic of the high affinity site. Changes in the relative intensities of the allowed and forbidden transitions of the 6^{th} and 5^{th} lines for different samples of the hammerhead high affinity site may arise from at least two possibilities. One is that there is a superposition of signals from bound and free Mn^{2+} ions as is the case for the 1:1 Mn:hammerhead sample. The other possibility is that there are slight differences in the specific coordination environment of the metal, reflected by the inclusion of A strain that

slightly broadens the spectrum. The A strain arises from slight variations in the coordination environment of the Mn^{2+} ion as in the case of the dG10.1 modified hammerhead sample or a mixture of free and bound metal ions.

Understanding what factors produce the unique EPR spectrum when a Mn^{2+} ion is bound at the A9/G10.1 site in the hammerhead provides information on the structural effect the RNA molecule has on the binding of the metal ion. The characterization of small model complexes provides the opportunity to isolate specific areas or features of interest that have been observed in the spectra obtained for various RNA systems. The use of EPR simulations is a powerful method to determine the precise effects the coordination environment has on the geometry of a metal ion. Knowing explicitly the cause of the unique EPR spectral signatures of the interactions Mn^{2+} ions have with the hammerhead sample provides insight into the study for Mn^{2+} ion interactions in other RNA systems.

CHAPTER VI

EXAFS STUDIES OF METAL-RNA INTERACTIONS

Introduction

X-ray absorption techniques are useful in characterizing the coordination sphere of a metal ion bound to a biomolecule. EXAFS spectroscopy has been widely used in the study of proteins and has provided insight into the coordination sphere of many metal ions in proteins.[72,99] Some examples where EXAFS has proven useful include studies of the nitrogenase enzyme that is involved with nitrogen fixation and has a molybdenum-iron protein (MoFe)[100,101] and the iron protein. EXAFS was used as a complementary technique to study the metal centers and determine the coordination environment that was not observed due to the low resolution of the crystal structure. The photosynthetic Mn oxygen-evolving complex of photosystem II has also been studied by various X-ray techniques including EXAFS providing information on the coordination environment of the four Mn atoms.[102]

X-ray absorption spectroscopy has had very limited application to structural studies of nucleic acids. Investigations of the C, O and N edges at low power X-rays to understand the electronic character of the nucleobases themselves have been performed.[103] The application of EXAFS spectroscopy to the study of metal-RNA interactions to understand their coordination environment, however, has been non-existent. A major factor in the use of EXAFS is its dependence on the homogeneity of the metal ion in a sample, since this X-ray technique detects all metal ions present in a sample it makes a single binding site essential to eliminate any ambiguity of the results obtained. Metal ions bound to RNA molecules tend to remain fairly hydrated and their

interactions are generally through long-range electrostatic interactions and normally do not have a specific or single coordination site, while metal ions coordinated to proteins generally are less hydrated and have a more defined coordination sphere.[104] The most reliable EXAFS interpretations for metal-RNA interactions can only be made for metal ions at a single coordination site.

The high affinity metal site of the hammerhead ribozyme and some simple model complexes were previously studied by the laboratory using EXAFS techniques to determine the coordination sphere of the metal site in the ribozyme (see Figure 6-1).[105] The results for the WT hammerhead showed a shell of backscatters at 2.2 Å containing N/O ligands as well as a distant scatterer(s) modeled as a P atom at a distance of 3.2 Å.[105] These results are consistent with the hammerhead crystal structure as well as the EPR results described in Chapter III. A phosphorothioate modification at the A9 site, which is known to affect catalytic activity of the hammerhead, was also studied using EXAFS to determine if the Mn^{2+} ion coordinates to the sulfur atom. Previous EPR and ESEEM data showed the Mn^{2+} ion was coordinated at the A9/G10.1 site even with the phosphorothioate substitution. EXAFS spectra were obtained for the Rp and Sp isomers of an A9 phosphorothioate modified hammerhead and did not show evidence of the Mn^{2+} ion directly coordinated to the sulfur atom. The results for the Sp sample had only minor changes in the overall spectrum at 3.2 Å, while the Rp sample had a large broad feature present at 3.4 Å. This new feature has been attributed to the presence of the sulfur atom in the second shell causing a backscattering effect. For the A9 Rp sample, the data for Mn^{2+} ion coordinated to A9/G10.1 site, it was proposed that there must be a distortion in the local RNA structure (see Figure 6-2). The Mn^{2+} ion is still coordinated at the G10.1

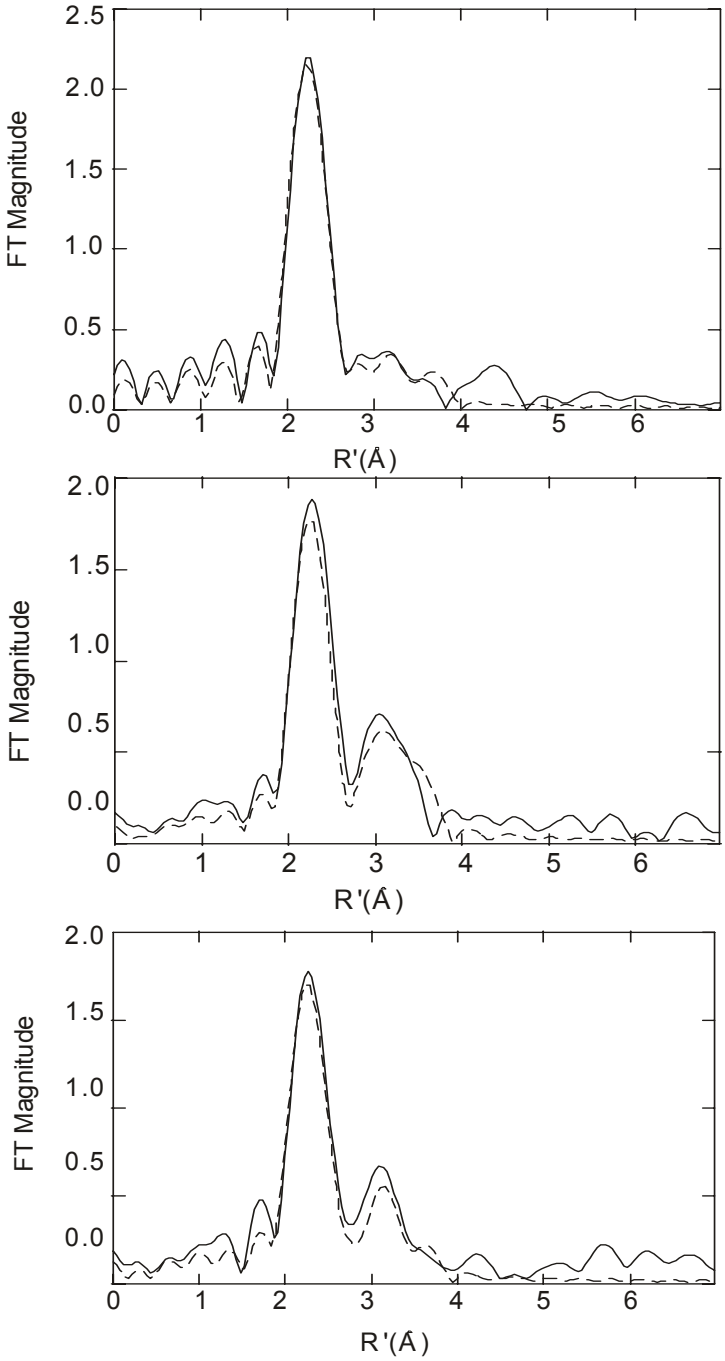

Figure 6-1: Mn EXAFS data and fits for the hammerhead ribozyme high affinity site. A) the results for the WT hammerhead, B) the RpS A9, and C) the SpS A9. Data taken from reference 105.

site and now coordinates to the Sp O, not the sulfur of the A9 phosphorothioate. This is proposed to causes a twist of the A9 phosphate that distorts part of the conserved core of

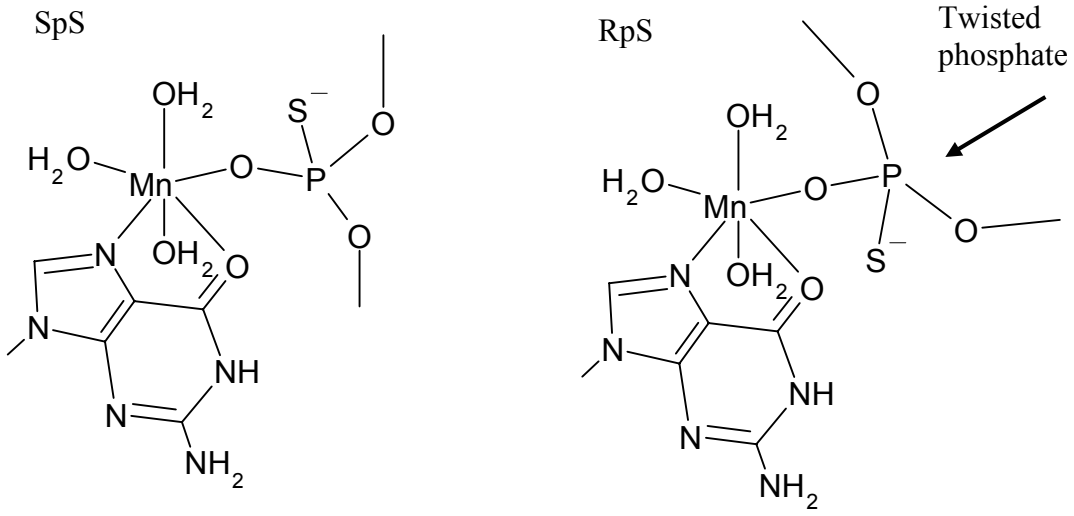

Figure 6-2: Proposed models for the Mn-A9 sulfur interaction based on previous EXAFS results.[105] The Sp isomer has Mn-O coordination, and the Rp isomer has Mn-O with a twisted phosphate group denoted by the arrow.

the hammerhead.

To fully characterize the Mn^{2+} EXAFS spectrum obtained for the WT hammerhead ribozyme samples, studies were performed with model complexes to address specific questions. The first question deals with the characterization of the type of scattering from a Mn^{2+} phosphate group interaction and determining number and distance and a comparison with a known coordination sphere. Also of interest are scattering effects arising from the rigid ring system of a Mn-guanine interaction that may produce long distance scattering. Providing this type of information will aid in correct assignment and fits of the observed spectra of large RNA complexes.

Three types of model complexes were prepared to isolate the cause of the individual features observed in the spectra for the hammerhead samples. EXAFS spectra for small model complex containing Mn^{2+} and GMP (guanosine monophosphate), phosphate ligands, and ATP(γ)S (adenosine gamma-thiotriphosphate) were obtained.

The results from these samples were used to compare to the previous results of the Mn^{2+} EXAFS hammerhead samples. To further understand the role the A9 phosphorothioate substitution has on the hammerhead high affinity metal site, samples with the separated Rp and Sp isomers with Cd^{2+} were also prepared. Since Cd^{2+} rescues the activity of the Rp A9 phosphorothioate modified hammerhead and has previously been suggested from ^{31}P NMR studies to coordinate to the sulfur atom in both the Rp and Sp isomers, EXAFS was used to confirm the Cd-S interactions. Using these results obtained by EXAFS, simple molecular modeling was performed to understand the coordination environment of the Cd^{2+} and Mn^{2+} ions bound to the hammerhead.

Results and discussion

EXAFS model complexes

Mn^{2+} model complexes were prepared and characterized and EXAFS spectra were obtained and analyzed in order to distinguish features that have been previously observed for the high affinity metal site in the hammerhead ribozyme. The EXAFS results for the hammerhead high affinity Mn^{2+} site predict 6 N/O ligands at approximately 2.2 Å in the first shell and an additional feature at 3.2 Å consistent with a distance P atom. Based on the ESEEM results from Chapter III, the 2.2 Å shell for the hammerhead is expected to partly arise from coordination of a guanosine. To obtain a model for a Mn-guanosine interaction, a Mn-GMP crystal was prepared as previously described[73] and verified by X-ray crystallography with the aid of Dr. Joseph Reibenspies at the X-ray Diffraction Laboratory, Center for Chemical Characterization and Analysis. The resulting structure is shown in Figure 6-3. The complex crystallizes in a monoclinic system with the space group C2 and the detailed analysis is given in Tables A-1 to A-5. The Mn^{2+} ion is

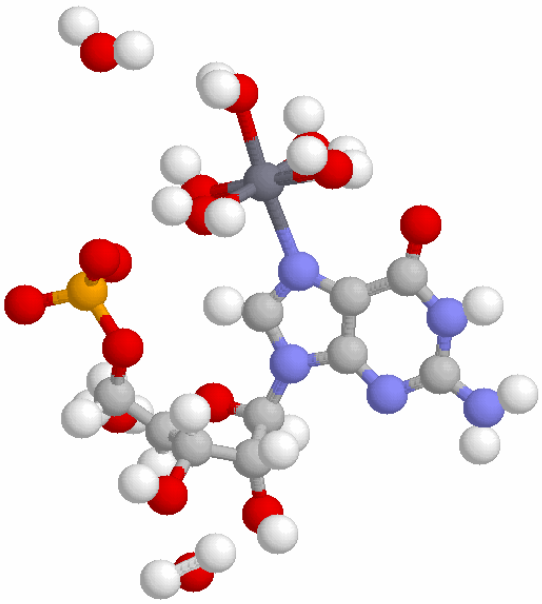

Figure 6-3: Crystal structure of [MnGMP]. The Mn ion (grey) coordination sphere consists of 5 H_2O and the N7 of the guanine. The H_2O groups have H bonding to the O6 position and phosphate oxygen. Mn^{2+} N7 distance of 2.250 (8) Å.

surrounded by five H_2O molecules at an average Mn-O distance of 2.2 Å and is coordinated to the N7 position of the guanine residue with a Mn-N distance of 2.250(8) Å.

The FT of the EXAFS results obtained on powered Mn-GMP complex show mainly a single peak that is modeled as a first shell coordination sphere of 6 N/O backscatters at an average distance of 2.19 Å (see Table 6-1 and Figure 6-4). These data are consistent with the results expected from the crystal structure. The results for the Mn-GMP and WT Mn-hammerhead samples both show a 6 N/O shell at distance of 2.2 Å thus confirming the similar coordination sphere for a Mn-guanosine interaction. The EXAFS results for the Mn-GMP sample do not show any features at a distance of 3.4 Å as was observed in the hammerhead samples. This result supports assignment of the > 3 Å scatterers in the hammerhead sample to Mn-phosphate coordination, and not to

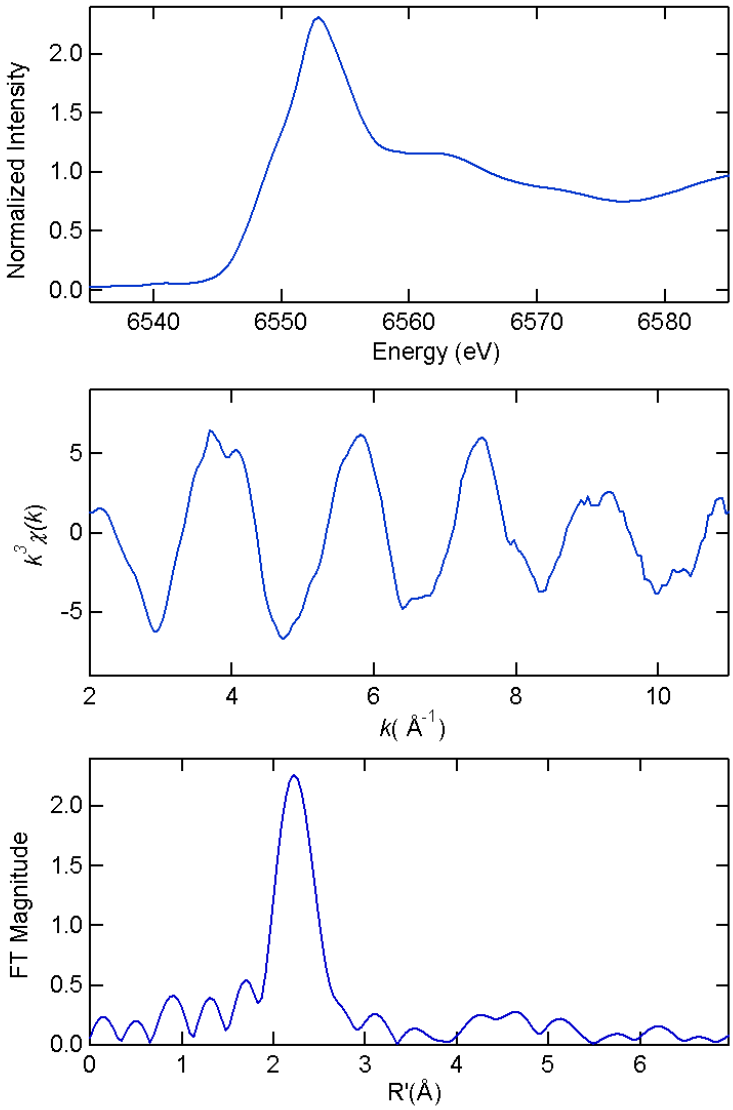

Figure 6-4: Mn EXAFS results for GMP complex. Top is the K-edge, middle k-space, and bottom is the Fourier transform of the data.

multiple scattering effects from the guanosine ring. The Mn-GMP crystal structure does have a through H_2O interaction to the phosphate group with a distance of 4.9 Å and would be expected to have only long-range scattering from P.

To model the contribution of the phosphate group to the EXAFS spectrum of the hammerhead Mn^{2+} site, a Mn^{2+} phosphate crystal was prepared and verified by X-ray

crystallography with the structure shown in Figure 6-5. This complex crystallizes in a triclinic system in the P-1 space group and the details of the X-ray results are provided in Tables A-6 to A-10. The Mn-phosphate crystal is a polymeric chain with each Mn ion

Table 6-1: Mn EXAFS fit results.

Sample	Shell	R_{as} (Å)	σ_{as}^2 ($Å^2$)	ΔE_0 (eV)	f[b]
Mn-GMP	$Mn-O_5$	2.19	0.0032	2.07	0.064
	Mn-N	2.09	0.0001		
Mn-Phosphate	$Mn-O_6$	2.15	0.0073	-2.80	0.115
	$Mn-(S,P)_1$	4.48	0.0015		
Mn-ATP(γ)S	$Mn-O_6$	2.16	0.0050	2.12	0.110
	$Mn-(C,N,O)_3$	3.11	0.0056		
	$Mn-(S,P)_1$	3.32	0.0020		
Mn-A9 RpS	$Mn-O_6$	2.17	0.0021	2.42	0.129
	$Mn-(S,P)_2$	3.37	-0.0010		

coordinated to six bridging phosphate groups. The average Mn-O distance is 2.2 Å and the distance between the manganese and phosphorous atom of 3.39 Å. The EXAFS results for the powered Mn-phosphate crystal show a major feature at 2.2 Å that is fit to a shell containing 6 O atoms at a distance of 2.17 Å that are attributed to the oxygen atoms from the phosphate groups. There is also a less intense feature at a distance of 3.4 Å consistent with the presence of the P atom observed in the crystal structure (see Table 6-1 and Figure 6-5). The presences of only a single phosphate may be attributed to the hygroscopic nature of the Mn-phosphate crystal and when exposed to moisture hydrates the Mn ion replacing the some of the phosphates with water molecules. The origin of the feature at 4.3 Å is still not clear, but may be attributed to a further set of oxygen atoms

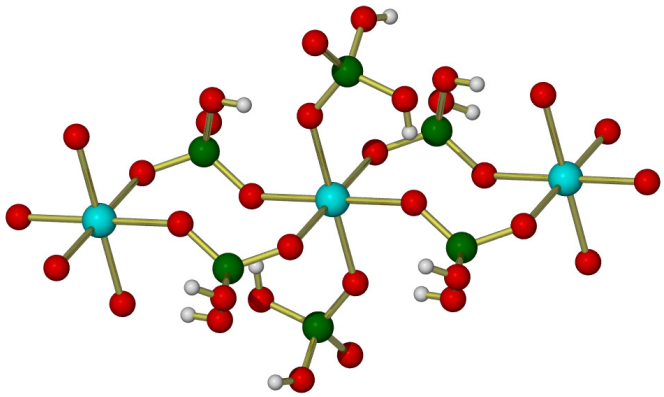

Figure 6-5: Crystal structure of the $[MnP_4O_{16}]^{6-}$ model complex. Coordination around the Mn (blue) consists of 6 bridging phosphate groups forming a chain.

from the phosphate group. The Mn-Mn distance from the crystal structure is 5.4 Å ruling out the possibility of a second Mn ion contributing to the EXAFS spectrum.

In an attempt to model the proposed Mn-thiophosphate interaction of the Mn-hammerhead samples with the presence of a phosphorothioate substitution, a Mn-ATP(γ)S (BioMol) complex in a 1 to 10 ratio was prepared in a 10 mM boric acid buffer at pH 8. A crystal of the Mn-ATP complex was not obtained and any attempts resulted in only the formation of precipitates. The EXAFS results for the solution of show a strong peak at 2.2 Å from an O/N shell and a somewhat broad feature at 3.4 Å that is consistent with a distant P atom (see Figure 6-7). Comparison to the Mn-ATP sample previously run, the intensity of the 3.4 Å feature is lower for the ATP(γ)S sample. There is little direct evidence for the presence of a sulfur atom in the coordination sphere. The features observed for the model complexes are similar to the results obtained for the WT hammerhead EXAFS spectrum and aids in assigning these features.

One concern from previous XAS experiments is the presence of high concentrations of NaCl, which could result in coordination of Cl^- ions to the EXAFS spectrum, a Mn A9 Rp S sample in 1 M $NaNO_3$, as opposed to the usual 1 M NaCl salt, was prepared using $Mn(NO_3)_2$. In order to rule out any contribution of signals from the presence of Cl^- ions coordinated to the Mn^{2+} ion to the EXAFS spectrum an A9 Rp S sample in 1 M $NaNO_3$, opposed to the usual 1 M NaCl salt, was prepared using

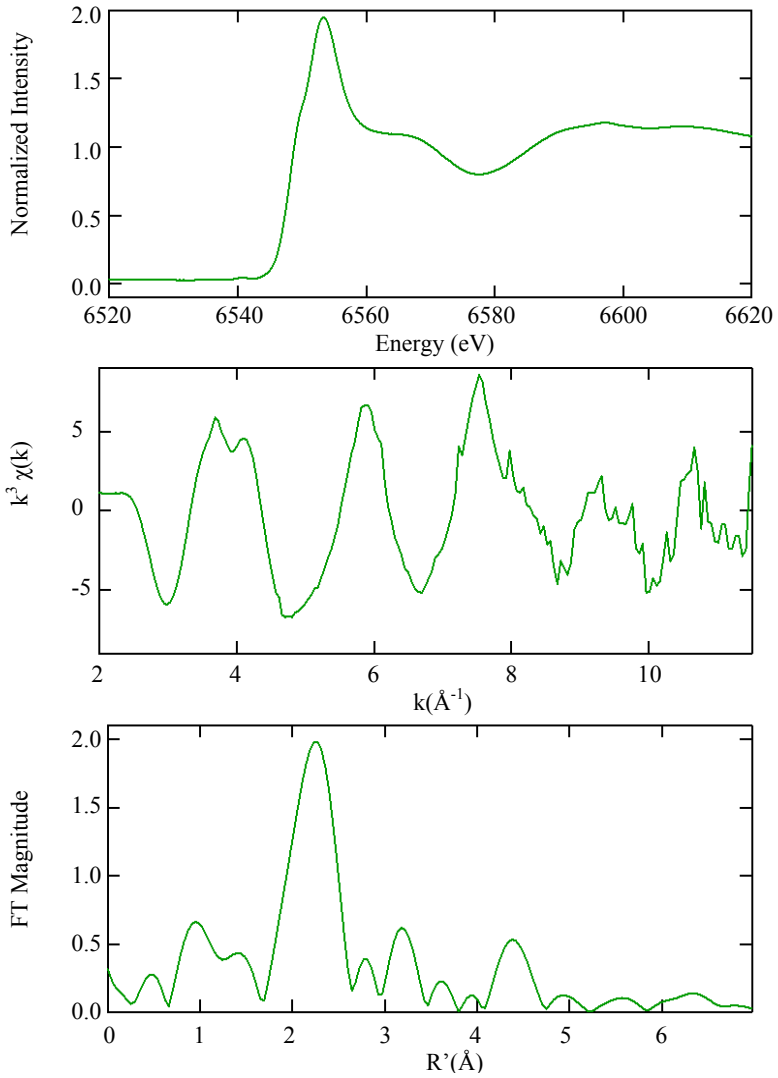

Figure 6-6: Mn EXAFS results for phosphate complex. Top is the K-edge, middle k-space, and bottom is the Fourier transform of the data.

$Mn(NO_3)_2$ source. The EXAFS results for the A9 Rp S hammerhead sample showed a feature at 2.2 Å and an additional feature at 3.4 Å (see Figure 6-7). Fits to these data show a O_6 shell at 2.17 Å and a $(S, P)_2$ shell at 3.37 Å (see Table 6-1). These results are consistent with the previous results for the A9 RpS sample, and indicate that there is no contribution of Cl^- ions coordinating to the Mn^{2+} ion at the high affinity site.

Cd EXAFS

Cd^{2+} ions often restore activity in phosphorothioate substituted samples that are inactivated in Mg^{2+}. To clarify the coordination environment of Cd^{2+} in these samples EXAFS was applied to study samples of the Cd^{2+} containing wild type hammerhead, and hammerhead samples with either a Rp or Sp phosphorothioate at the A9 position. The EXAFS results for the Cd-WT HH sample showed an intense feature at 2.40 Å that contains the first coordination sphere of the Cd^{2+} ions (see Figure 6-8). This shell is modeled with 6 N/O atoms at 2.40 Å (see Table 6-2). There is also a small feature at a distance of 3.2 Å that most likely arises from the presence of the coordination phosphate group. Both these features are similar to what has been observed for the Mn substituted wild type HH samples except the Cd-O/N distance is longer, as expected.

The substitution of the sulfur atom for oxygen at A9 position results in a definite change in the absorption K-edge of both the Rp and Sp phosphorothioate HH samples in comparison with the wild type HH sample. This slight change in the edge arises from the Cd^{2+} ion directly coordinated to the sulfur atom. The sulfur atom contains more electron density than the oxygen atom affecting the electronic environment around the Cd^{2+} ion

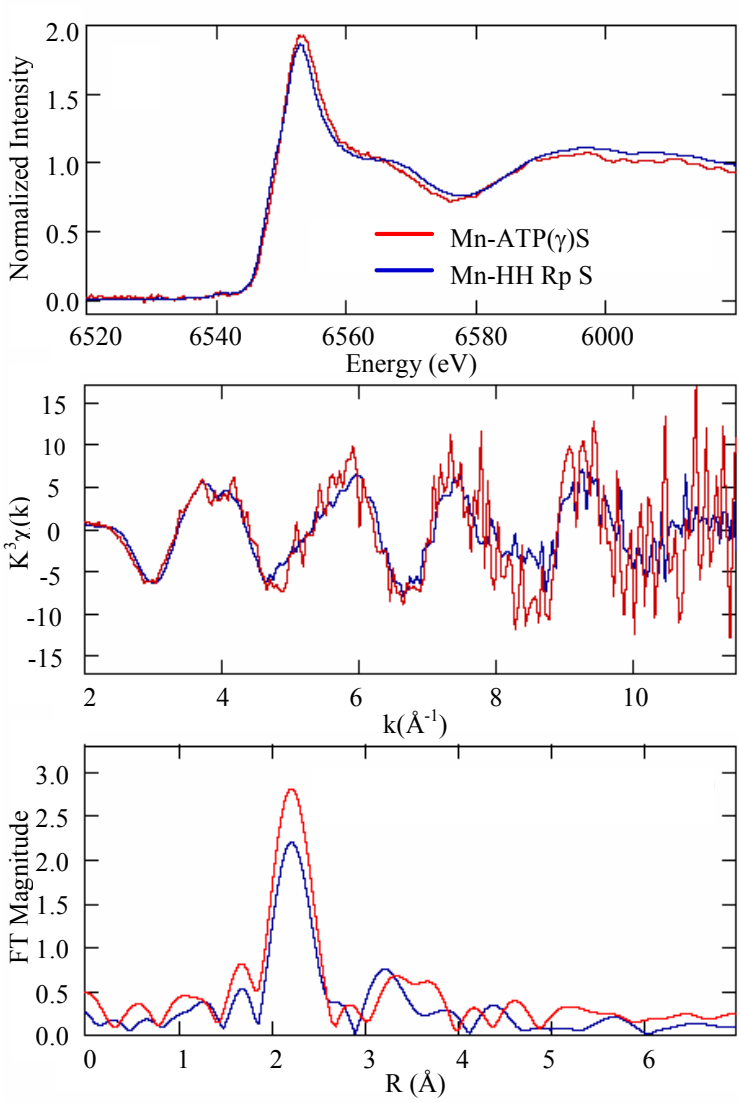

Figure 6-7: EXAFS results for Mn-ATP(γ)S and Rp S hammerhead. The ATP(γ)S sample shows a broad feature at 3 Å similar to the broad feature observed for the Rp S hammerhead sample.

and shifting the K-edge by a few eV reflecting a difference in the ionization potential of the core electrons. The presence of the sulfur atom with greater electron density affects the ionization potential of the Cd^{2+} ion (see Figure 6-8). The EXAFS results for the A9 Rp and Sp isomers have a greater intensity of the peak at 2.4 Å and a slight shift to a longer average distance (see Figure 6-8). The fit for the RpS data suggests a shell of five O atoms at 2.36 Å and a S atom at 2.59 Å (see Table 6-2). The fit for the SpS data also suggests a shell of five O atoms at 2.37 Å and a S atom at 2.60 Å (see Table 6-2) Both of these results are consistent with direct coordination of the Cd^{2+} ion to the sulfur atom of both isomers of the A9 phosphorothioate substitution in the hammerhead samples. The feature at 3.2 Å for the wild type HH samples shifts to a slightly farther distance for the Rp and Sp phosphorothioate samples consistent with the presence of the sulfur atom coordinating the Cd^{2+} ion having longer Cd-S and S-P bond lengths compared with to the oxygen atom making the phosphorous atom slightly farther away. The Cd^{2+} EXAFS results showed that the Cd^{2+} ion coordinates to the sulfur atom of both the Rp and Sp isomers of the phosphorothioate substitution, thus confirming predictions from previous ^{31}P NMR experiments.[53] These results also show the utility of the EXAFS technique to studying metal-RNA interactions involving the Cd^{2+} rescue effect of an RNA molecule with a phosphorothioate substitution.

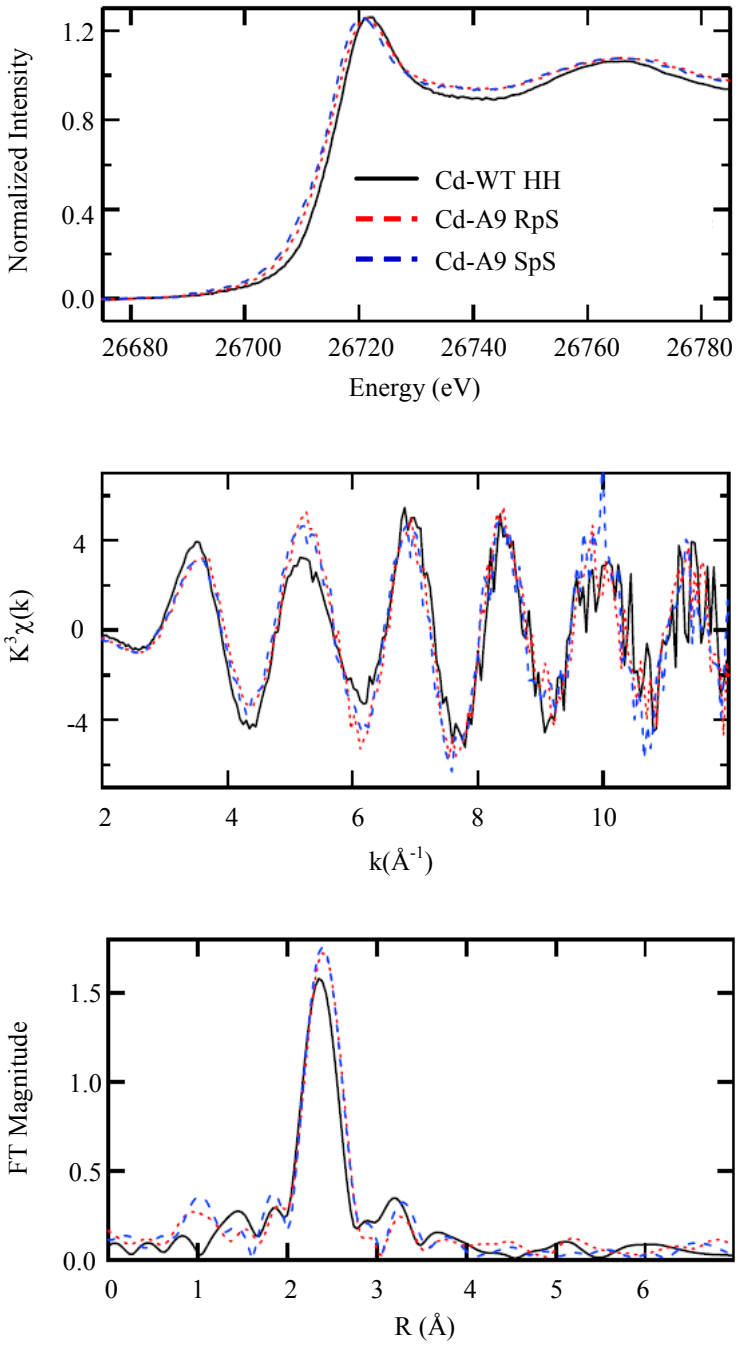

Figure 6-8: Cd^{2+} EXAFS of wild type and phosphorothioate substituted hammerhead. X-ray absorption edge for the sulfur at the A9 site shows a shift compared to the wild type sample. The FT shows a slightly longer distance for the sulfur containing samples consistent with the presence of sulfur coordination to the Cd ion.

Table 6-2: Cd EXAFS fit results.

Sample	Shell	R_{as} (Å)	σ_{as}^2 ($Å^2$)	ΔE_0 (eV)	f^b
Cd-WT HH	$Cd\text{-}O_6$	2.40	0.0032	1.80	0.112
Cd-A9 RpS	$Cd\text{-}O_6$	2.41	0.0022	4.23	0.113
	$Cd\text{-}O_5$	2.36	0.0033	-1.54	0.118
	$Cd\text{-}S_1$	2.59	-0.0011		
Cd-A9 SpS	$Cd\text{-}O_6$	2.42	0.0018	3.21	0.136
	$Cd\text{-}O_5$	2.37	0.0028	-3.58	0.087
	$Cd\text{-}S_1$	2.60	-0.0007		

Molecular modeling

Computational models are useful tools to shed light on the structural role that a metal ion has when coordinated to a biomolecule. Information obtained by moleculuar modeling can be used to aid in understanding structural changes to the RNA molecule upon binding of a metal ion and the effect that a specific substitution may have on the metal ion binding properties.

In order to investigate the structural role of the bound metal ion at the A9/G10.1 site in the hammerhead and understand the effects of changes in the coordination, simple molecular models were constructed. Molecular mechanics methods using the Cerius2 program were used to find the energy-minimized structure of several model complexes. The G8, A9, and G10.1 residues from a hammerhead crystal structure (1HMH) were isolated and used as a starting point for the calculations. Reducing the number of atoms involved in the calculations reduced the amount of time needed to perform the

calculations. Using the EPR results for the basis of the metal ion coordination as described earlier in Chapter III, a Mn^{2+} ion was modeled at the A9/G10.1 site directly coordinated to the N7 of G10.1 and the pro-R phosphate oxygen of A9 and with four H_2O ligands.

The A9/G10.1 site taken from the crystal structure is shown in panel A of Figure 6-9. Placing a Mn^{2+} ion coordinated at 2.2 Å to the N7 of G10.1 and within binding distance of the A9 phosphate gives a Mn-P distance of 3.9 Å. This Mn-P distance reduced to 3.2 Å in the energy minimized structure, which is closer to Mn-P distances previously observed from a crystal structure of Mn-ATP.[80] The minimized energy and distances are shown in Table 6-3. The overall structural change of the three nucleotides is minimal and reinforces that the N7 of G10.1 and the Rp oxygen of A9 are positioned in a way that a metal ion can coordinate to both positions with only minor alterations to the structure.[106] These slight changes observed between the crystal structure (panel A) and the minimized model (panel B) in Figure 6-9 and may be related to the low resolution of the crystal structure, and hence do not imply too much of structural change in the ribozyme upon metal ion binding.

Phosphorothioate effect at A9 site

Previously it was found that placing a phosphorothioate in the Rp position of the A9 site results in a dramatic reduction of the activity of the cleavage reaction in Mg^{2+}.[107] This activity can, however, be rescued when a thiophilic metal such as Cd^{2+} is added. In the presence of Mn^{2+}, the Rp phosphorothioate substituted hammerhead requires a very high concentration of ions (~15 mM) to recover activity, which reaches only 1/3 of the maximum WT activity. A study using EPR and EXAFS spectroscopy suggested that

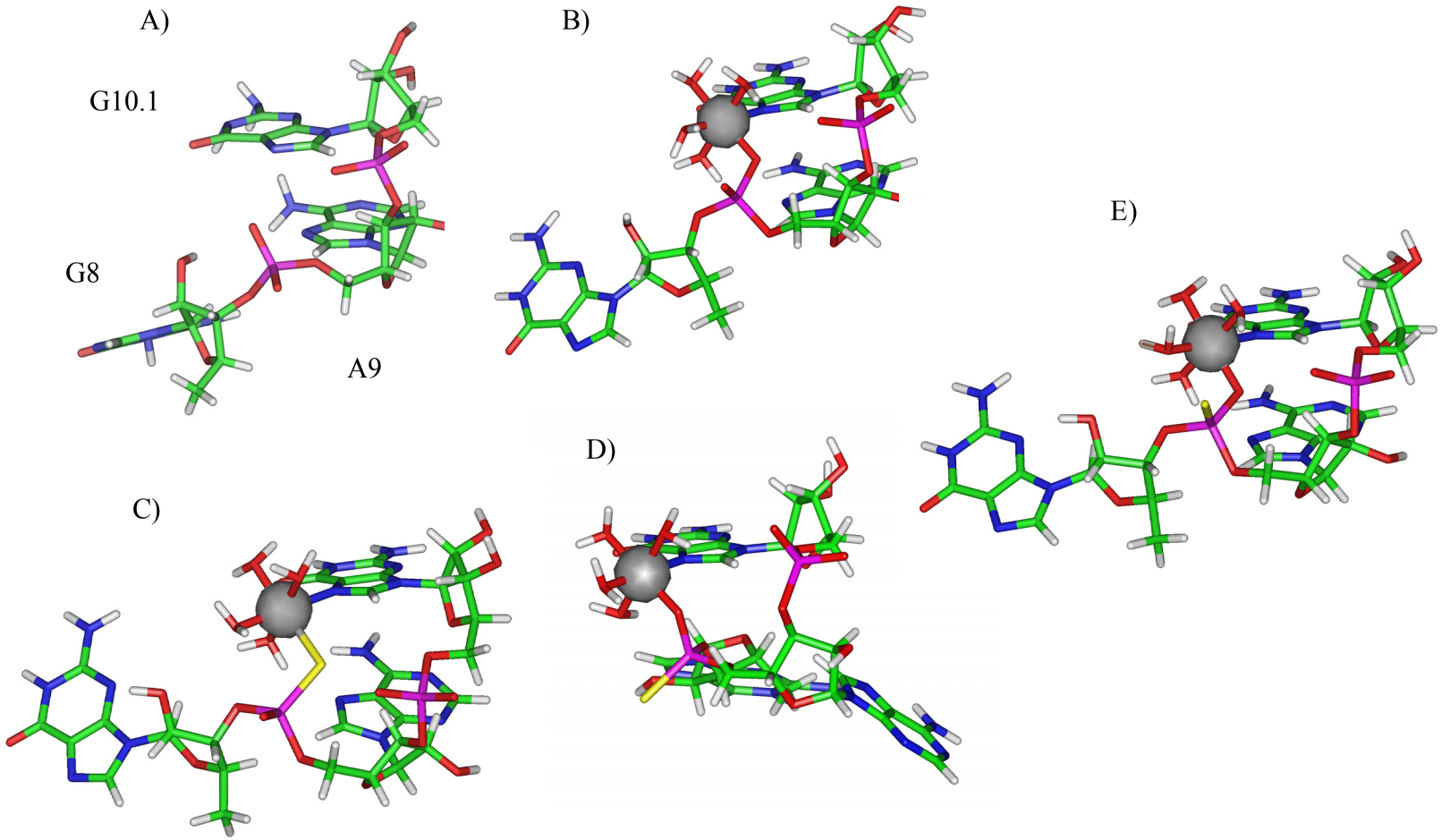

Figure 6-9: Molecular models of the hammerhead A9 site with Mn ion. A) A9 site without metal ion, B) WT HH, C) Mn-S coordination with the A9 Rp S, D) Mn-O coordination with the A9 RpS, E) Mn-O coordination with the SpS A9. Nucleotides were capped with a hydroagen on the 3' end and a methyl group at the 5' end.

the Rp thiophosphate the Mn^{2+} ion still being coordinates at the A9/G10.1 site without binding to the sulfur atom. It was proposed that the Mn^{2+} ion binds to the oxygen atom for both the Rp and Sp sulfur substitutions and distorts the RNA structure to accomplish this feat in the Rp phosphorothioate case. To understand the way the metal ions interact with the A9 site with a phosphorothioate substitution, models of the A9/G10.1 site in the hammerhead with a bound Mn^{2+} ion was constructed and energy minimized. A sulfur substitution was placed in either the pro-R or pro-S position and Mn coordinated to either the O or S ligand was studied.

The minimized structure of the hammerhead model with the Mn ion coordinated to the sulfur at the Rp position of the A9 phosphate shows a slight rearrangement from the wild type structure because this model has a longer Mn-P distance due to the longer Mn-S and S-P bond lengths (Table 6-3). Since Mn^{2+} is a borderline metal ion it might be expected to have a greater preference to coordinate an O or N containing ligand as opposed to a S containing ligand. Placing the sulfur atom at the Sp position with the Mn bound to the Rp oxygen atom, the energy and distances of the energy-minimized model are comparable with the non-sulfur substituted structure. The EXAFS results of the A9 RpS hammerhead showed the Mn ion is not coordinated to the sulfur atom, and the ESEEM results showed that the Mn is still located at the high affinity metal site. These results led to a model where the Mn ion is bound to the Sp oxygen of the phosphorothioate substitution.[105] The minimized structure for this model is quite compelling in that the energy and distances are comparable to the "wild type" model, but has the phosphate group between G8 and A9 twisted and the G8 nucleotide flipped out of alignment with the rest of the structure (Figure 6-9). Comparison of the torsion angles of

Table 6-3: Structural information for Mn^{2+} model complexes at the A9/G10.1 site.

Model	M-P distance (Å)	Min. Energy (kcal)	Torsion angle O3, P, O5, C5
Mn-O WT	3.2	384	-167.6
Mn-S Rp S	3.6	373	-170.0
Mn-O Rp S	3.2	372	174.0
Mn-O Sp S	3.2	386	-164.9

the phosphate backbone, the Mn-O Sp bound complex has a radically different value than those observed for any other model (Table 6-3). The WT model complex has a torsion angle of –167º measured from the O3, P, O5, and C5 direction while the Sp bound O model has a value of +174º for the same angle (see Table 6-3). This is a bend of the phosphate backbone in the opposite direction causing a severe twist distorting the RNA structure. This distortion would most likely affect the formation of part of the conserved core that is essential for catalytic activity, leaving the hammerhead inactive.

Cd interaction at the A9 site

The Cd^{2+} EXAFS results for the sulfur substituted A9 site in the hammerhead suggested that the Cd coordinates to the sulfur in both Rp and Sp isomers. Since the hammerhead is active in Cd^{2+} with both Rp and Sp A9 substitutions, these results suggest that Cd coordination to sulfur in either position produces little structural change. Molecular models of Cd^{2+} at the A9 site were constructed to test the likelihood of these results. When a Cd^{2+} ion is placed in the wild type structure, the minimized structure is similar to the structure of the Mn-HH structure. The main difference between the Mn^{2+} and Cd^{2+} models is the Cd^{2+} phosphate oxygen interaction is trans to the N7 group

opposed to the cis orientation observed for the Mn^{2+} HH structures (Figure 6-10). The minimized structure for the WT HH model with a coordinated Cd^{2+} ion has a Cd-P distance of 3.3 Å. The Cd^{2+} ion was directly coordinated to the sulfur atom at the Rp position of the A9 thiophosphate model and the energy of the structure was minimized resulting in a similar structure as observed for the Cd^{2+} wild type hammerhead structure. The Cd-S distance was 2.5 Å, similar to the value obtained for the EXAFS fit. Coordinating the Cd^{2+} ion to the sulfur atom in the Sp position also had a minimum effect on the energy and the structure of the minimized model (Figure 6-10). The Cd-P distances and phosphate torsion angles are shown in Table 6-4. The lack of changes in the structure with the phosphorothioate substitution is consistent with results that the phosphorothioate hammerhead is active in Cd.

Conclusion

The limited available information for metal-RNA interactions studied by EXAFS spectroscopy makes interpreting the spectral features of the hammerhead difficult. The approach used here was to characterize small model complexes to study by EXAFS in order to assign the EXAFS results obtained for the hammerhead. The Mn-GMP and Mn-phosphate models provided evidence of contribution of the guanine base to the 2.2 Å feature and a phosphate complex for the 3.4 Å feature, respectively, that aids in the interpretation of the observed Mn^{2+} EXAFS spectrum for the hammerhead.

The Cd^{2+} EXAFS results indicate the rescue of the catalytic activity of the phosphorothioate substitution at the A9 site involves direct coordination of the Cd^{2+} ion to the sulfur atom. The shift in the K-edge of the X-ray absorbance and the higher amplitude and longer distances observed in the EXAFS spectrum is suggestive of the Cd^{2+} coordinating through the sulfur of both Rp and Sp isomers at the A9 site and

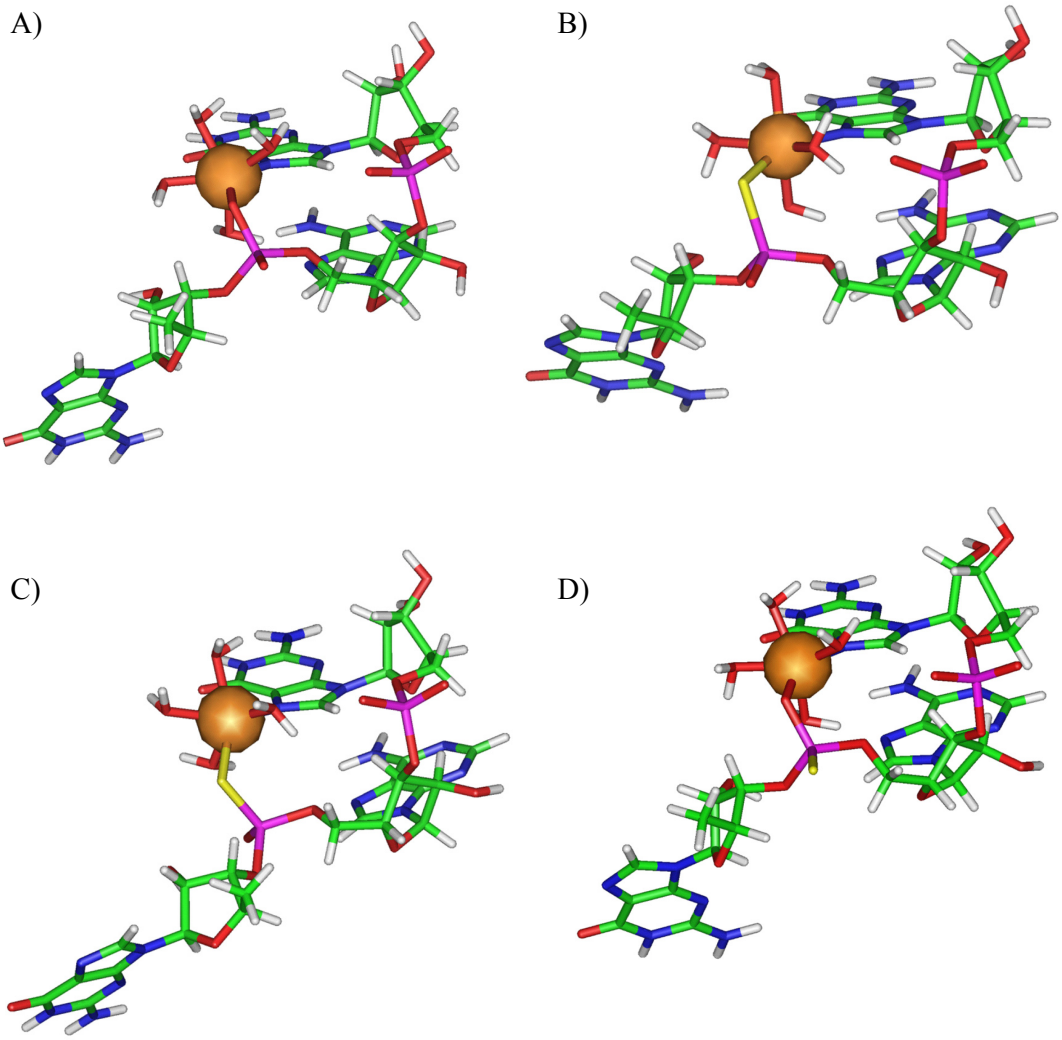

Figure 6-10: Molecular models of the hammerhead A9 site with Cd ion. A) WT HH, B) Cd-S with the A9 RpS, C) Cd-S with the A9 SpS, D) Cd-O with the A9 SpS. Models were capped with a H at the 3' end and a methyl group at the 5' end.

confirms previous ^{31}P NMR results.

Molecular modeling was used to create a picture of the high affinity metal ion site and understand the effects the A9 sulfur substitution has on the metal ion-binding site. The molecular models are suggestive of local flexibility of the A9/G10.1 site in the conserved core that is resulting in the details of the site being affected by metal ion binding. The change observed at this site may propagate and may affect the formation of the conserved core creating a misfolded form of the hammerhead thus reducing catalytic activity. The difference between the binding preference and the rescue of activity for the phosphorothioate at the A9 phosphate for Mn^{2+} and Cd^{2+} is based on the binding propensity for the ions. Mn^{2+} is a borderline hard-soft metal ion and has a much higher binding affinity for hard ligands like oxygen or nitrogen ligands over soft sulfur ligands. Cd^{2+}, on the other hand, is a soft metal ion and prefers coordination with a soft sulfur ligand. Cd^{2+} has a slightly larger ionic radius compared to Mn^{2+} (1.09 vs 0.86 Å).[17] Energy-minimized structures predict that Cd^{2+} binds the N7 and phosphate oxygen in a trans fashion, which is the reason why the Cd^{2+} ion so readily coordinates to the sulfur atom in both Rp and Sp positions without major structural changes of the phosphate

Table 6-4: Structural information for Cd^{2+} model complexes at the A9/10.1 site.

Model	Cd-P distance (Å)	Energy (kcal)	Torsion angle O3, P, O5, C5
Cd-O WT	3.2	568	-96.1
Cd-S Rp S	3.6	545	-88.6
Cd-S Sp S	3.4	569	-28.3
Cd-O Sp S	3.2	556	-118.6

backbone or the residues. This type of coordination can accommodate the binding of the metal ion to sulfur in both isomers without disrupting the formation of the conserved core.

The A9/G10.1 site is also positioned to coordinated Mn^{2+} through the phosphate oxygen and N7, but in a cis fashion for this smaller ion. Any attempt to coordinate these ligands in a trans orientation causes a severe distortion in the orientation of the Mn-guanine interaction. The molecular modeling of Mn coordinated to the Sp O ligand of an A9 RpS substitution, as predicted by the EXAFS studies, must twist the phosphodiester bond in order to accommodate this coordination and such a distortion would likely propagate to the structure of the conserved core.

EXAFS spectroscopy has the unique advantage that all the coordinating ligands to a metal ion will contribute to the observed signal. The homogeneous binding of a single metal ion to an RNA molecule is fundamental for accuracy in determining the coordination environment using EXAFS spectroscopy. Unfortunately, this may leave the use of EXAFS to RNA systems where only one metal ion can be isolated by some means, such as by sodium ion competition as in the present case for the hammerhead high affinity metal site. Using all available information obtained from EXAFS and EPR techniques, molecular modeling has provided the most likely picture of the metal ion coordinated at the A9/G10.1 site. The results presented here demonstrate the utility of EXAFS spectroscopy in determining the coordination environment of a metal ion coordinated to an RNA molecule. The use of molecular modeling in conjunction with knowledge of the ligands of the bound metal ion determined by various spectroscopic studies is helpful in understanding metal-RNA interactions.

CHAPTER VII

CHARACTERIZATION OF MN^{2+}-RNA INTERACTIONS WITH RNA SEQUENCES CONTAINING THE SHEARED G-A METAL ION BINDING MOTIF

Introduction

The secondary structure of RNA molecules is predominately determined by the formation of helical regions of Watson-Crick base pairs.[3] Functional RNA molecules often contain elements with non-standard base pairs that provide areas of flexibility in the RNA molecule and significantly contribute to the formation of tertiary structure.[108] Examples of these structural elements include hairpins, bulges and internal loops and occur as repeated motifs in large RNA molecules, such as the 16S and 23S rRNAs.[4] The internal loop is a set of mismatched bases that can be from one to several nucleotides in length that are flanked by Watson-Crick base pairs. An internal loop may be symmetrical or asymmetrical in size and/or in the type of nucleotides that are present.

The presence of an internal loop within an RNA molecule can have a profound effect on the stability of the RNA when compared to a normal duplex sequence. The degree that the RNA molecule is affected depends on the type and number of nucleotides that are present in the internal loop as well as the closing base pair of the loop. Although the internal loop contains mismatched bases with non-standard pairings, it does not mean that an internal loop is not structured. Mismatched bases have their own unique H-bond networks within the internal loop that can act to stabilize the RNA molecule, and have a distinct orientation compared to the adjacent standard base pairs.[109] Numerous studies have been conducted to study the effect that different possible mismatches have on the

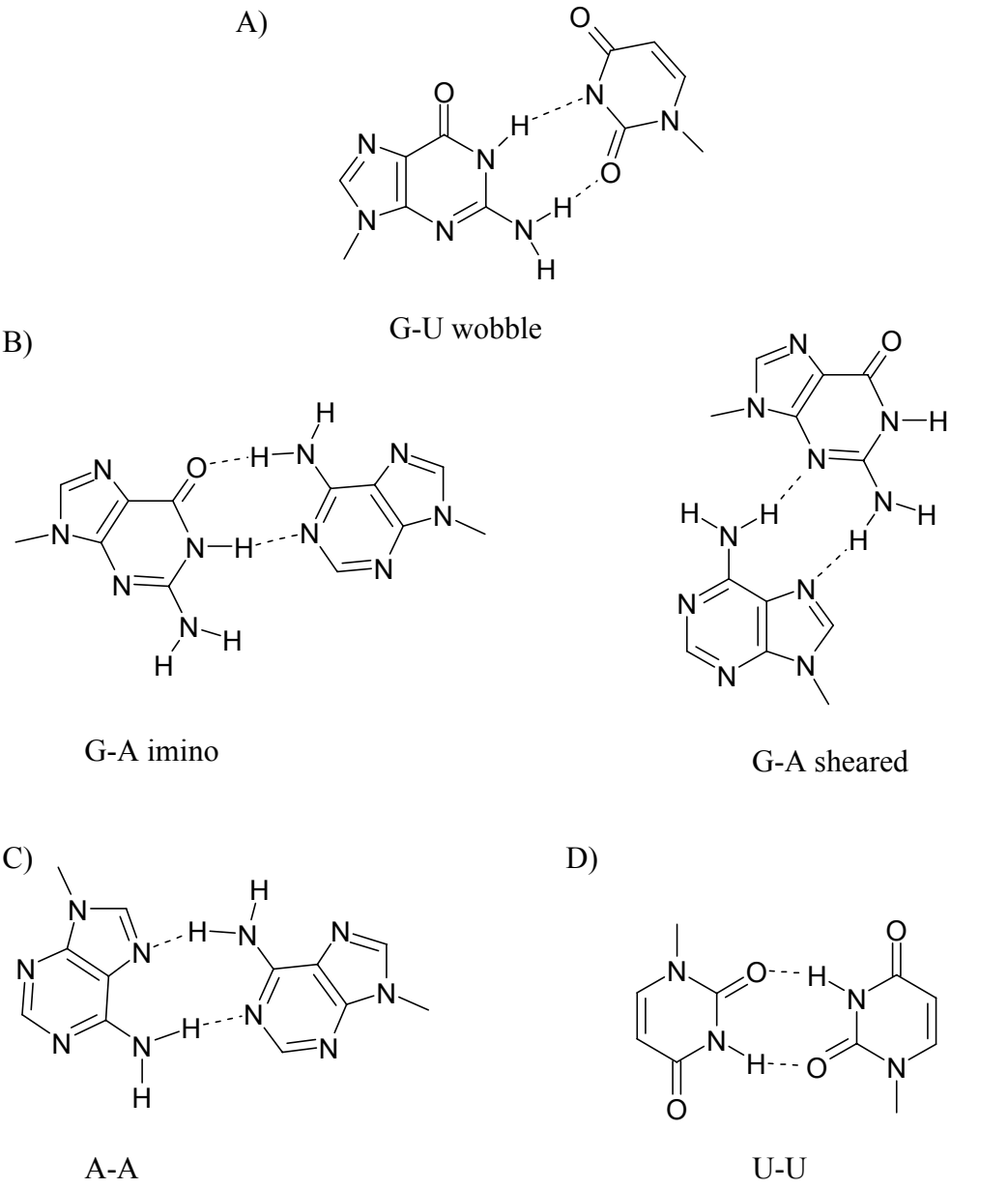

Figure 7-1: Examples of mismatched RNA bases. A) G-U wobble base pair, B) possible G-A interactions, C) A-A interaction, D) U-U interaction. Presence of non-Watson Crick base pairs produces internal loops or bulges that may destabilize and affect the helical structure of an RNA duplex.

stability of small RNA duplexes.[110-117] The G-U wobble base pair (Figure 7-1) is the most stable mismatch and is a very common element that may play a role in protein recognition or as a metal ion binding site.[118] The next most stable mismatches are the

sheared and imino G-A mismatches, followed by a U-U mismatch with the A-A mismatch being the least stable (Figure 7-1).[119] The effect of the closing base pair is that the internal loop of an RNA sequence is more stable when a G-C base pair closes the loop in comparison with an A-U closing (Figure 7-2).

The presence of tandem G-A mismatches with a GC closing base pair as shown in Figure 7-2 is a commonly occurring structural motif found in many RNA systems including the hammerhead ribozyme, the *Tetrahymena* ribozyme, and also in ribosomal RNA sequences (Figure 7-2).[120] Tandem sheared G-A mismatches are important due to their prevalence, structural variations, and biological functions,[107] where they can mediate tertiary interactions, protein recognition or act as metal ion-binding sites.

The G-A mismatch has been observed in two different conformations, the face-to-face imino H-bonded interaction and the sheared conformation, depending on the closing base pair. The sheared conformation occurs when the closing base pair is GC, while the imino conformation has a CG closing base pair (Figure 7-2). In the sheared conformation, the N3 position of the guanine residue hydrogen bonds with the exocyclic NH_2 group of the adenine residue. In the imino conformation, the O6 of the guanine residue hydrogen bonds with the exocyclic NH_2 group on the adenine residue. The stability of the G-A conformation depends on, at minimum, three factors; 1) electrostatic interactions between partial charges, 2) the number of H-bonds, including H-bonds to the backbone, and 3) backbone distortions.[107]

NMR solution structures of RNA duplexes with tandem G-A mismatches with either a GC[122] or a CG[107] closing base pair have been solved. The structure of the duplex containing tandem G-A mismatches with GC closing base pairs has an over-wound

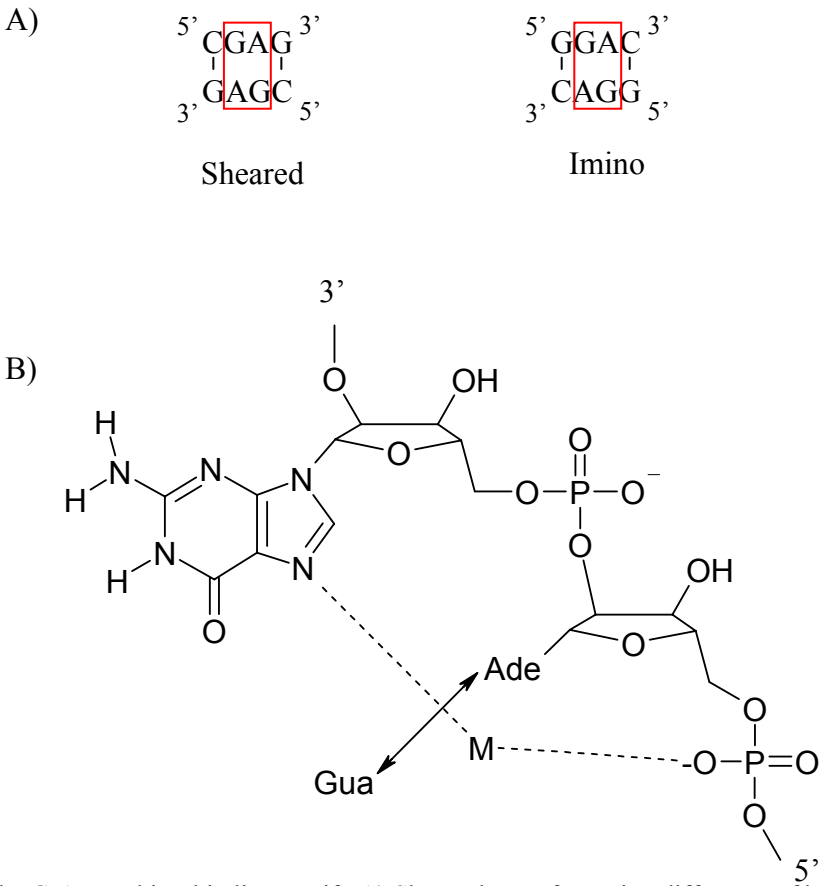

Figure 7-2: The G-A metal ion-binding motif. A) Shows the conformation difference of between GC and CG closing pairs. B) Representation of the metal ion binding at the N7 position of the guanine and the phosphate oxygen of the adjacent adenine. The double-headed arrow represents the sheared G-A base pair.

helical structure that facilitates interstrand stacking of the mismatched bases.[121,122] This causes an overall narrowing of the duplex creating a more compact structure.[120] A duplex containing tandem imino G-A mismatches with a CG closing base pair induces a different H-bonding pattern in the mismatch that minimizes unfavorable interactions between the partial charges of the G-A mismatch and the CG pairing.[107] The GAC containing duplex has an under-wound helical structure making the duplex wider than normal. This seemingly subtle switching of the closing base pair has a dramatic structural change on the RNA molecule. The sheared G-A mismatch closed with a GC

base pair has the pro-R phosphate oxygen positioned in closer proximity to the N7 of the closing guanine residue (4.1 Å) than that observed in a normal duplex with an A-U base pair instead of the G-A mismatch (7.6 Å). Thus, the sheared conformation of the G-A mismatch creates a small pocket that is an ideal metal ion-binding site in an RNA molecule. An example of the impact that switching the closing base pairs has on an RNA molecule is demonstrated by the metal ion-binding A9/G10.1 site in the hammerhead ribozyme, which has a G-A mismatch with a GC closing base pair that when switched to CG, greatly affects the activity of the cleavage reaction the hammerhead performs.[32]

The tandem sheared G-A mismatch of the hammerhead ribozyme is contained within the conserved core that is vital for the performance of the cleavage reaction. Several crystallographic studies of the hammerhead, as well as solution spectroscopic data indicate that a metal ion binds at the A9/G10.1 location. A metal ion has also been observed using NMR spectroscopy to bind at a G-A site in a fragment of the P5abc domain of the group I intron.[15]

A self-complementary 10mer RNA duplex containing two G-A mismatches within a GA_3 internal loop was crystallized in the presence of Mn^{2+} ions and has a similar coordination environment as that observed for the hammerhead ribozyme A9/G10.1 site.[123] The presence of this internal loop severely distorted the helix structure as compared to a regular based paired duplex. The major groove of the GAAA sequence was compressed to 2 Å (from 4 Å) and the minor groove widened to 13.5 Å (from 11.1 Å). These two G-A sites both contained a Mn^{2+} ion bound to the N7 position of the guanine and the phosphate oxygen of the adjacent adenine similar to that observed for the hammerhead crystal structures.

Taira and coworkers have studied a 10 nucleotide self-complementary RNA duplex containing tandem G-A mismatches as a model system for the metal ion-binding site of the hammerhead A9/G10.1 site.[124-126] Using ^{1}H NMR spectroscopy, they observed changes in the chemical shifts of the C8 position of the guanine residue upon titration of Cd^{2+} ions and determined an apparent K_d value of 320 μM in 40 mM NaCl for the metal ion binding to the guanine. Using ^{15}N NMR and labeling single residues they observed a large chemical shift for the peak from the N7 of the sheared guanine residue upon the addition of Cd^{2+} confirming the metal ion binding to the N7 position. They also proposed that the results obtained from this duplex could be directly correlated to the structural role of the metal ion at the A9/G10.1 site of the hammerhead ribozyme.

An in-depth characterization of the metal ion binding properties under solution conditions of RNA molecules with varying internal loops containing the G-A motif has not yet been performed. In this study, a series of loops are compared in order to observe the effect of the size and composition of the loop on the metal ion binding properties (see Figure 7-3). One series of RNA duplexes contain symmetrical internal loops consisting of two of the metal ion-binding motifs, sheared G-A with a GC closing base pair, and the addition of 0-2 A-A pairs inserted between the G-A motifs. The addition of the mismatched A-A was done to study the effect of the distance between the two G-A motifs on the metal ion-binding properties of the RNA molecule. The A-A mismatch generally has a destabilizing effect on an RNA sequence that may allow for more flexibility within the internal loop creating more distortion of the helical structure. This difference in stability can be attributed to the G-A mismatch having the potential to make four different types of H-bonds while the A-A mismatch only makes two H-bonds

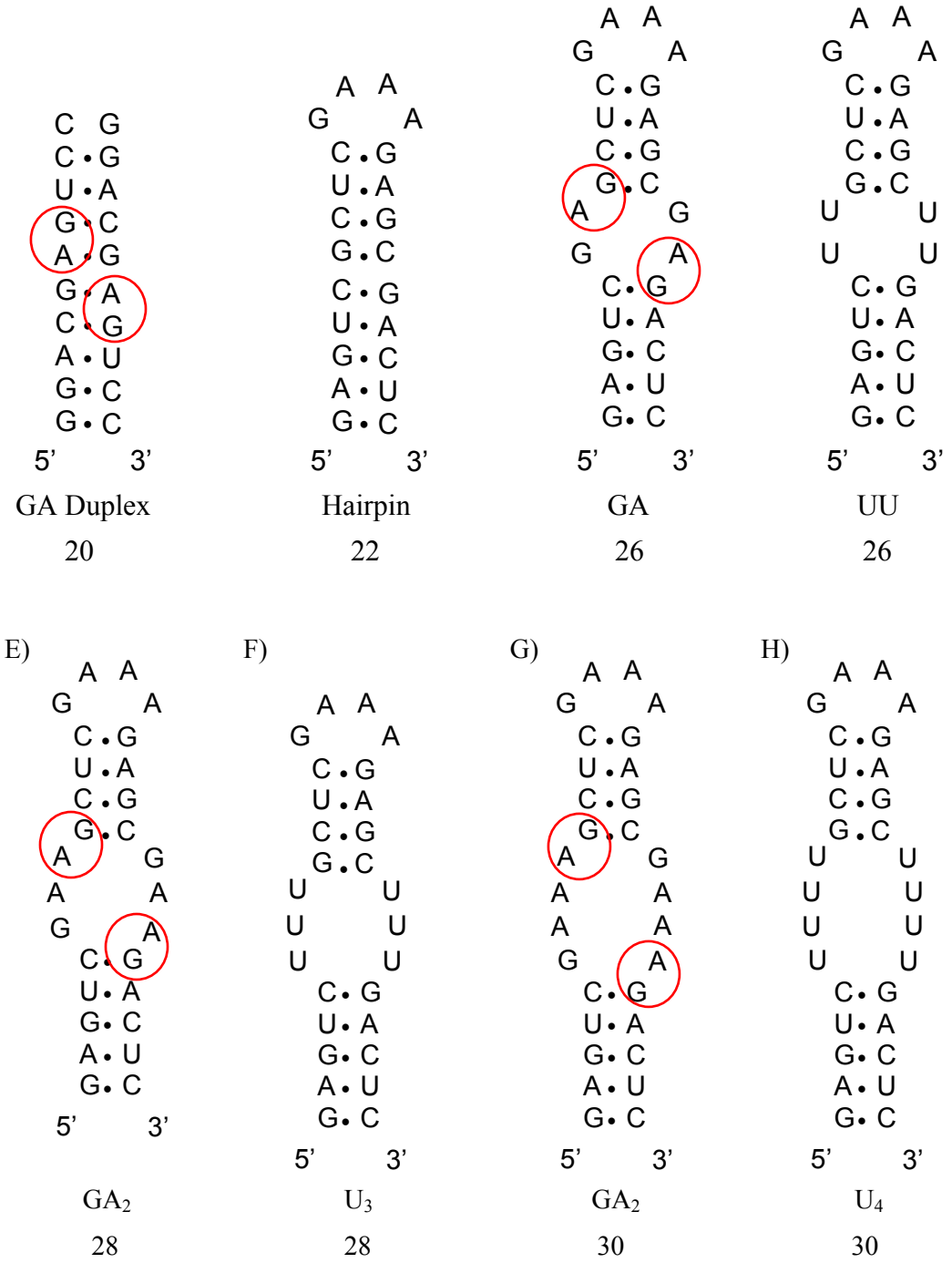

Figure 7-3: Secondary structure of RNA sequences containing internal loops. A) GA 10mer duplex, B) hairpin, C) GA loop, D) U_2 loop, E) GA_2 loop, F) U_3 loop, G) GA_3 loop, H) U_4 loop. The red circle is the site of the sheared G-A base pair that is a potential metal ion binding site.

through interactions between the amino groups.[112] As a comparison to the sequences containing the G-A metal ion-binding motif, a series of loop sequences containing all U-U mismatches of the same size was also investigated. The U-U mismatched sequences do not contain any proposed metal ion binding sites and are not expected to have an unusual affinity for metal ions. The presence of the U-U mismatch in an RNA duplex has been shown to maintain an overall A-form helical structure.[112] The U-U mismatch interacts through a pair of imino H-bonds, which allows this pairing to have a greater stability than the A-A mismatch.[113]

The RNA sequences used here were hairpins capped with a GAAA tetraloop in order to increase the stability of the molecules and better isolate the role that a specific metal ion may have on the structure of the RNA molecule (Figure 7-3). Studies with the GA containing 10mer duplex were also carried out to evaluate this sequence as a metal ion-binding motif. Detailed thermodynamic information for this series of RNA sequences was obtained by UV/Vis thermal denaturation experiments. The metal ion binding properties for each sequence were determined by using Mn^{2+} ions as a spectroscopic probe in order to employ room temperature EPR binding isotherm studies. Circular dichroism was also used to probe for any structural differences between the RNA sequences in the presence and absence of added Mn^{2+} ions.

Results and Discussion

Melt profiles

The effect of the size and type of internal loop to the RNA on the stability of the RNA helix was determined by UV melting profiles. The series of RNA molecules used in this study is shown in Figure 7-3. Increasing the size of the internal loop is expected to

decrease the stability of the RNA sequence and lead to lower T_m and ΔG values. The T_m values and enthalpy of all the RNA strands were obtained at 2 μM RNA concentration in 100 mM NaCl, 5 mM TEA, pH 7.8 and are shown in Table 7-1. Representative melt profiles with and without added Mn^{2+} ions are shown in Figure 7-4. The van't Hoff enthalpy was determined by fitting the melt profile using a two state model using the program Tmelt.[68] An example of the fit for the hairpin sequence is shown in Figure 7-5 where the raw data are in solid lines and the fits are in dashed lines. The fits for the other RNA sequences are shown in Figure A-3 and A-4. The thermodynamic values ΔH, ΔS, and $\Delta G_{37°C}$ for all the sequences studied are shown in Table 7-1.

The 10mer self-complementary duplex with the GA motif has a single broad melting profile with a T_m value of 45.0°C and a van't Hoff enthalpy of 47 kcal/mol. The melting profile of the hairpin RNA sequence, which contains no G-A mismatches, is a single sharp transition with a T_m of approximately 89.7°C and a van't Hoff enthalpy of 74.0 kcal/mol. The GA hairpin has a single transition melting profile with a lower T_m value of 77.4 ºC and van't Hoff enthalpy of 70.0 kcal/mol. This is an 11.3°C decrease in the T_m value compared to the hairpin sequence. Table 7-1 shows the ΔT_m from the hairpin sequence for all the sequences upon the addition of the internal loop. With the addition of an A-A mismatch for the GA_2 sequence, the melting profile is slightly broader than the GA sequence and has a lower T_m value of 72.4°C with a van't Hoff enthalpy of 56 kcal/mol. The ΔT_m for this sequence is 16.3ºC compared to the hairpin. The melt profile for the GA_3 sequence is slightly broader compared to the GA_2 sequence and has a lower T_m value of 69.8°C with a van't Hoff enthalpy of 42 kcal/mol. The ΔT_m for this sequence has a change of 19.9 °C compared to the hairpin sequence.

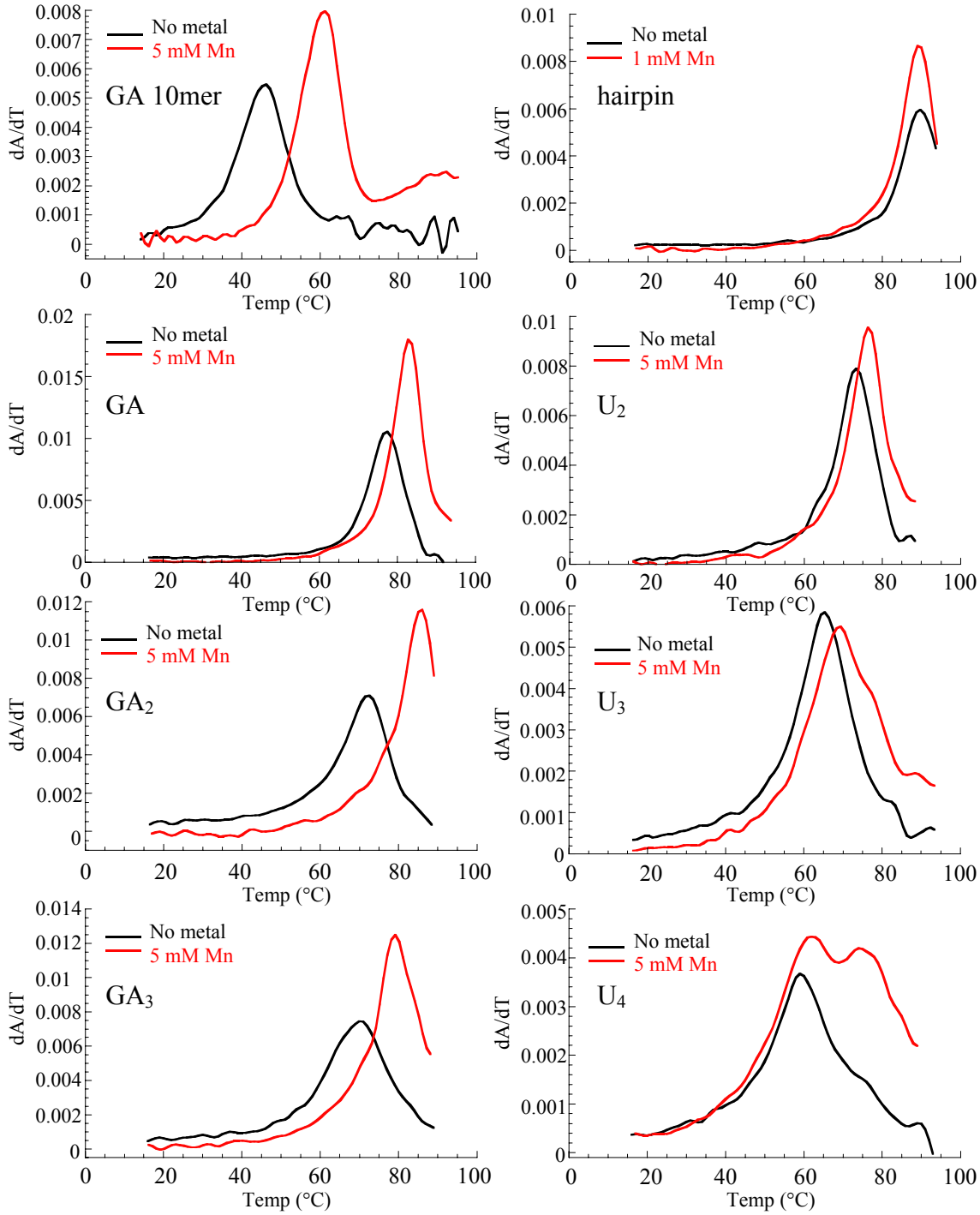

Figure 7-4: Melt profiles of RNA sequences used in loop study. Black traces are 260 nm derivative of absorbance in 100 mM NaCl, while red traces are 260 nm derivative of absorbance with the addition of Mn^{2+} ions.

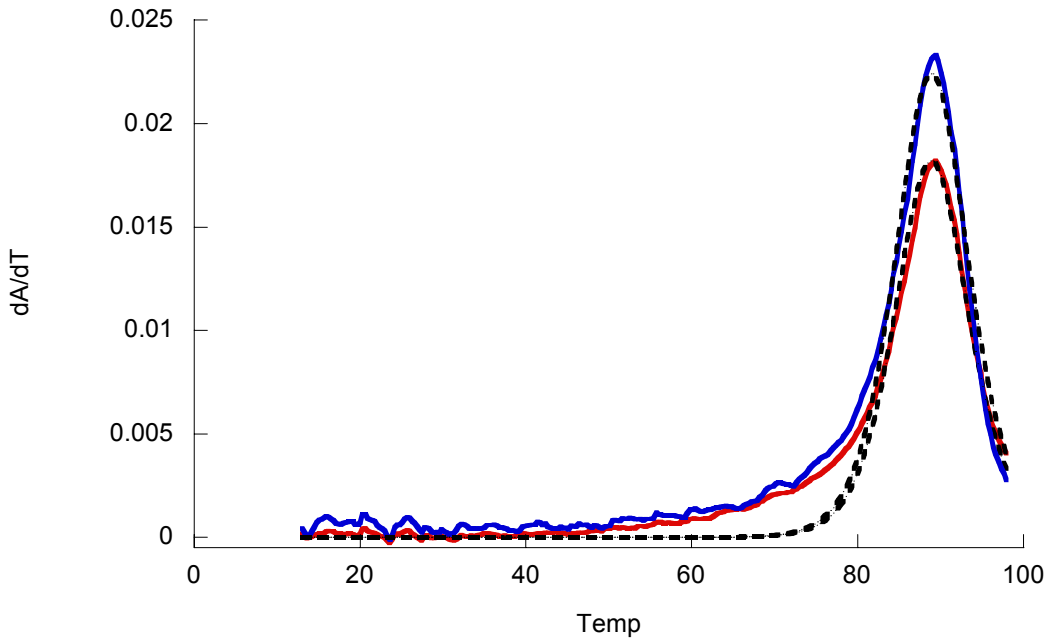

Figure 7-5: Example of melt profile fit for the hairpin sequence. The blue and red trace represents the first derivative of the 260 nm and 280 nm transitions respectively. The underlying black dashed line is the corresponding fit to each transition. All plots were fit using the program Tmelt to a single transition except where noted.

The addition of the A-A pairing between the two sheared G-A mismatches appears to have a small effect on the thermal stability and a modest effect on the determined enthalpy. The G-A sheared pairing is the most stable mismatch in this study that only causes a slight decrease in the enthalpy while the addition of the A-A pairings causes an additional slight destabilization of the RNA structure. The calculated $\Delta G_{37°C}$ values for the sequences decrease as the size of the loop increases, consistent with the presence of the mismatches destabilizing the RNA structure.

The thermodynamic values obtained for the U-U containing sequences shows a significant decrease of T_m and ΔH values in comparison with the G-A containing sequences. The U_2 sequence has a sharp melting profile with a T_m of 73.3°C and a van't

Table 7-1: Thermodynamic parameters derived from UV thermal denaturation of RNA sequences containing internal loops.

RNA	T_m (ºC)	ΔT_m (ºC)[a]	$-\Delta H$ (kcal/mol)[b]	$-\Delta\Delta H$[c]	$-\Delta S$ (eu)	$-\Delta G_{37ºC}$ (kcal/mol)
GA 10mer	45.0	—	47.0	12.0	148	1.1
Hairpin	89.7	—	74.0	14.0	204	10.7
GA loop	77.4	11.3	70.0	20.0	199	8.3
GA_2 loop	72.4	17.3	56.0	21.0	162	5.8
GA_3 loop	69.8	19.9	42.0	18.0	122	4.2
U_2 loop	73.3	16.4	61.5	15.5	177	6.6
U_3 loop	65.4	24.3	43.0	11.0	127	3.6
U_4 loop	58.9	30.8	32.0	47.0[d]	96	2.2

T_m determined under 100 mM NaCl, 5 mM TEA, at pH 7.8 and 2 μM RNA concentration.
a) Difference in T_m value compared to hairpin sequence.
b) van't Hoff enthalpy calculated from fitting using the program Tmelt.
c) Change in enthalpy with addition of Mn^{2+} ions.
d) Fit to two transitions.

Hoff enthalpy of 61.5 kcal/mol. The ΔT_m is 16.4°C lower than that of the hairpin sequence, which is only 4.1°C lower than the T_m value of the GA sequence. The U_3 sequence sees a further decrease in the T_m with a value of 65.4°C and a van't Hoff enthalpy of 43 kcal/mol. The ΔT_m is 24.3°C lower than the hairpin sequence. The U_4 sequence is the most destabilized RNA molecule and has a T_m value of 58.9°C with a van't Hoff enthalpy of 32 kcal/mol. The U_4 sequence has a ΔT_m of 30.8°C, which is the greatest change in the T_m value from the hairpin and has the lowest enthalpy of all the sequences studied here.

The T_m values and the determined enthalpies for the U_2, U_3 and U_4 sequences show steadily decreasing values as the size of the internal loop increases. The two U-U

mismatches of the U_2 sequence have two H-bonds from the imino groups and only slight alters the RNA structure compared to the hairpin sequence, which makes this sequence very stable. The U_3 and U_4 sequences, however, have a dramatic decrease in the thermal stability with a ~10 kcal lower enthalpy value than the corresponding G-A containing sequences. The presence of 3 or more consecutive U-U mismatches in an internal loop greatly affects the stability of the RNA sequence. The U_4 sequence has an 8.5 kcal/mol reduction in the ΔG_{37} value compared to the hairpin loop making it the least stable molecule in this series.

Metal ion dependency

The addition of divalent metal ions has a stabilizing effect on RNA sequences due to a higher charge to radius ratio making them more effective at charge screening the phosphate backbone when compared to monovalent ions. The T_m values for all the RNA sequences in this study were determined under a range of Mn^{2+} ion concentrations to obtain information on the influence the metal ions have on the RNA stability and the resulting effects on the T_m and enthalpy values. The melting profiles for all the RNA sequences with the addition of 5 mM concentration of Mn^{2+} ions (with the exception of the hairpin sequence where the highest Mn^{2+} concentration was only 1 mM) are shown in Figure 7-4. In all the G-A containing sequences the peaks shift to a higher T_m value and become more intense, indicating a higher enthalpy upon the addition of Mn^{2+} ions. The relationship between $1/T_m$ versus log [M] for the G-A containing sequences are shown in Figure 7-6 and the K_f and K_u, the apparent equilibrium constants for metal association for folded and unfolded form of the RNA, as well as the determined K_d values are reported in Table 7-2.

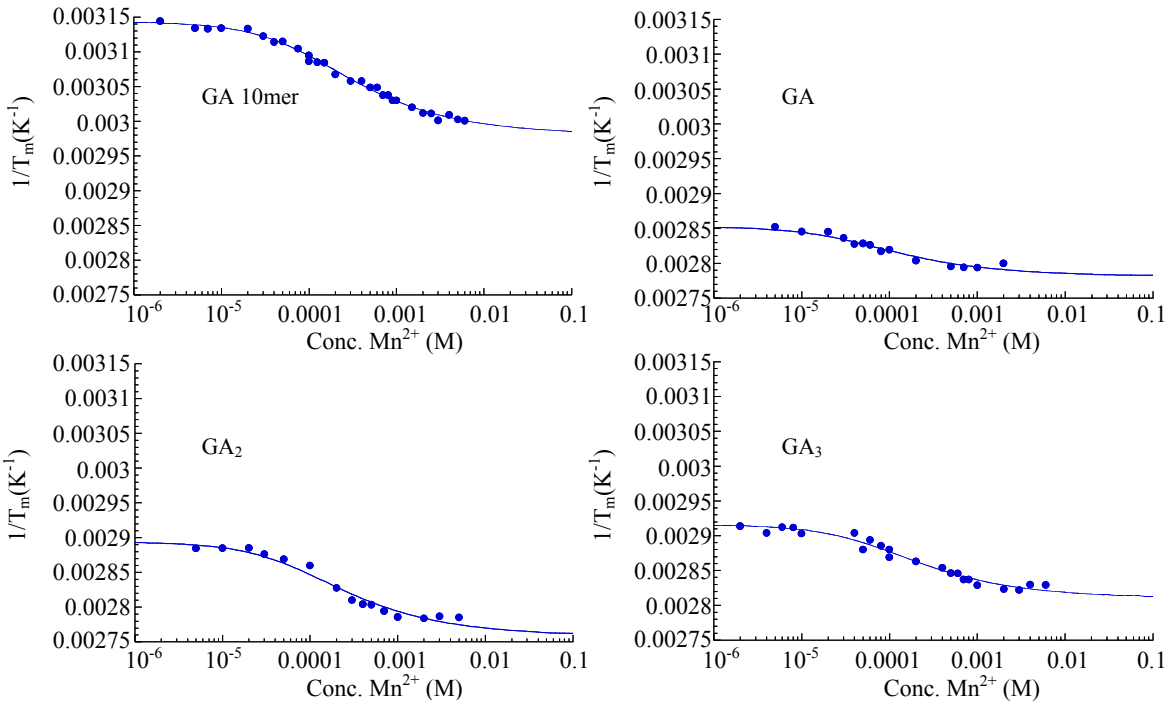

Figure 7-6: T_m values as a function of added metal ions. The G-A sequences each showed a change of ~10ºC in T_m values at the highest Mn^{2+} ions concentrations. Data were fit to equation 2-7 assuming a two state model and a single transition.

The hairpin RNA sequence sees virtually no change in the T_m value upon addition of Mn^{2+} ions, but an increase in the intensity of the melt profile is observed starting at low concentrations of around 200 μM Mn^{2+} and remains the same for the rest of the Mn^{2+} ion concentrations studied. This small change is suggests the Mn^{2+} ions have little or no interactions on the stabilization of the hairpin sequence, and results in a minimal affect on the T_m value, and enthalpy value. The apparent K_d value was not determined for the hairpin sequence due to the lack of major changes in the T_m values and the inability to track melting features greater than 90ºC.

The metal dependence for the melt profiles of the U-U containing loops shows several interesting results. The U_2 sequence has a minor change in the T_m value of only

3-4°C at the addition of the highest metal ion concentrations (3-5 mM Mn^{2+}). A closer inspection of this data shows a very small effect on the T_m with added Mn^{2+} ions indicating that there is little effect on the stabilization of the RNA structure.

While the melting profile of all the G-A containing sequences show a single transition at high Mn^{2+} concentrations, the melting profile for the U_4 sequence has a pronounced biphasic transition with the addition of ~500 μM Mn^{2+}, showing a second peak that grows in at around 70°C. At the highest Mn^{2+} concentrations, the intensities of the two transitions are roughly equal in intensity and clearly separated. Melting profiles for this sequence were also obtained under 100 mM NaCl with 10 mM Mg^{2+}, and under 1 M NaCl to test if the two peaks were present under these conditions. In both cases a major peak was observed at ~ 66°C with a slight shoulder at a higher T_m value. These results suggest that this sequence does not unfolding in a single step and the two-transition phenomenon is Mn^{2+} dependent.

To investigate possible dimer formation of this RNA strand, melt profiles of the U_4 sequence at concentrations of 20 μM and 27.5 μM were compared to the profile obtained with 2 μM RNA. With increasing RNA concentrations the T_m value is expected to increase for a bimolecular process such as dimer formation, whereas no change is expected if the melting transition is from a monomer. In both cases the majority of the transition occurred at 58°C with only a minor shoulder at ~70°C, similar to the profile observed at 2 μM RNA concentration, which rules out possible dimer formation. The most reasonable hypothesis for the biphasic melt profile at high Mn^{2+} concentrations is that the presence of four U-U mismatches greatly destabilizes the RNA molecule, as shown by the very low ΔG_{37} value of -2.2 kcal/mol, the melting transition is no longer a

single cooperative process, and two distinctive unfolding events are occurring. The addition of Mn^{2+} ions has a greater affect on the stability of the hairpin portion of the molecule and has a higher T_m value that begins to separate out from the first transition.

In contrast with the U_4 loop sequence, the sequences containing the sheared G-A pairing show a much greater change in the T_m value in the presence of Mn^{2+} ions and maintain a single melting transition. The GA sequence has a 6°C change in the T_m upon addition of Mn^{2+} ions. This relatively small increase can be attributed to this sequence having the highest $\Delta G_{37°C}$ value of all the loop containing sequences and is already only slightly less stable than the hairpin sequence. The GA_2 sequence has a 14°C increase in the T_m value while the GA_3 internal loop has a T_m increase of about a 10°C upon the addition of Mn^{2+} ions. The G-A 10mer duplex has an overall T_m change of 15°C with the addition of Mn^{2+} ions. Plots of $1/T_m$ versus the concentration of Mn^{2+} were fit to determine the K_f and K_u values and are shown in Table 7-2. Taking the reciprocal of K_f yields the apparent dissociation constant for the metal ions' effect on the stability of the RNA molecule and is shown in Table 7-2. The K_d values for the G-A containing sequences are around 200-400 μM and do not show much evidence for a particularly high affinity metal ion binding site. These data suggest that the Mn^{2+} ions act mostly in an electrostatic manner to stabilize the RNA structure. The U_2 loop sequence was the only sequence from the U-U containing series for which a full metal dependent T_m plot could be obtained due to the broadening and biphasic transitions of the U_3 and U_4 melt profiles at high Mn^{2+} concentrations. The apparent K_d for this sequence is quite tight, but is an artifact of the small and sudden change in the T_m value upon addition of low concentrations of Mn^{2+} ions. The small change in the thermodynamic values observed

for the thermal denaturation of the hairpin sequence shows only an increase in the enthalpy of the transition upon addition of Mn^{2+} ions, and little to no change in T_m.

Table 7-2: Apparent affinity constants obtained from metal ion dependence of melt profiles.

RNA	$K_f (M^{-1})$	$K_u (M^{-1})$	$K_d (\mu M)$
GA 10mer	3640 ± 200	1840 ± 116	275 ± 24
GA loop	8409 ± 1487	5534 ± 1075	119 ± 25
GA_2 loop	2914 ± 527	1712 ± 356	343 ± 75
GA_3 loop	4370 ± 639	3199 ± 496	229 ± 40

Conditions were 2 μM RNA in 100 mM NaCl, 5 mM TEA, pH 7.8.

Room temperature EPR

In order to quantitate directly the interactions of Mn^{2+} ions with the series of loop containing RNA sequences, room temperature EPR was used to determine the number and affinities of the metal ions bound to the RNA molecule. If an RNA sequence has a tight metal ion-binding site (a low K_d value), it would be expected that this site would be populated at low Mn^{2+} ion concentrations. The total number of Mn^{2+} ions bound to the RNA will be related the number of binding sites that are available. In the absence of monovalent ions, it would be expected that each Mn^{2+} ion would be able to screen the negative charges of two phosphates and consequently the total number of Mn^{2+} ions is expected to be approximately one-half of the number of negatively charged phosphate groups. Non-specific or weak metal ion-binding sites in the RNA would be in competition with Na^+ ions as so would have lower apparent affinities as the Na^+ concentration increase. The RT EPR experiment observes the Mn^{2+} ions that have a change in relaxation properties due to their association with the RNA molecule by inner-sphere or outer-sphere coordination through a water molecule.

The Mn^{2+} binding isotherms determined using EPR for the loop containing sequences are shown in Figure 7-7 and the number of Mn^{2+} ions bound to the RNA molecule and the apparent K_d values obtained are shown in Table 7-3. For the G-A containing sequences, the K_d value is lower than the other sequences indicative of an average stronger metal-RNA interaction. The GA sequence has the lowest K_d value of 115 ± 26 μM, and with the addition of each A-A mismatch the K_d value slightly increased for the GA_2 and GA_3 sequences to 131± 25 μM and 164 ± 40 μM, respectively. The U-U containing sequences all have a higher K_d value in the range of ~ 250 to 390 μM, indicating weaker set of metal-RNA interactions. The hairpin sequence also has a weak binding affinity comparable to the U-U containing sequences, consistent with a lack of a specific metal ion-binding site.

The GA 10mer duplex has a higher K_d value of 350 ± 162 μM than the capped G-A containing sequences and is more comparable with the U-U containing and hairpin sequences. Although the GA 10mer sequence contains the sheared G-A metal ion-binding motif, it has a $\Delta G_{37°C}$ of -1.1 kcal/mol making this RNA rather unstable compared to the other G-A containing sequences. The major difference between the GA 10mer duplex the other sequences is the absence of the tetraloop that greatly stabilizes the hairpin sequences, making the duplex very unstable. The metal ion interaction with this sequence is weak but has a major stabilization effect on the RNA structure.

All of the RNA sequences have approximately the same total number of ions bound of five to eight Mn^{2+} ions. The G-A sequences do have a lower apparent K_d value than the non-metal ion-binding motif sequences. This is reflects of a set of slightly tighter sites that are not observed for the hairpin or U-U containing sequences. The EPR

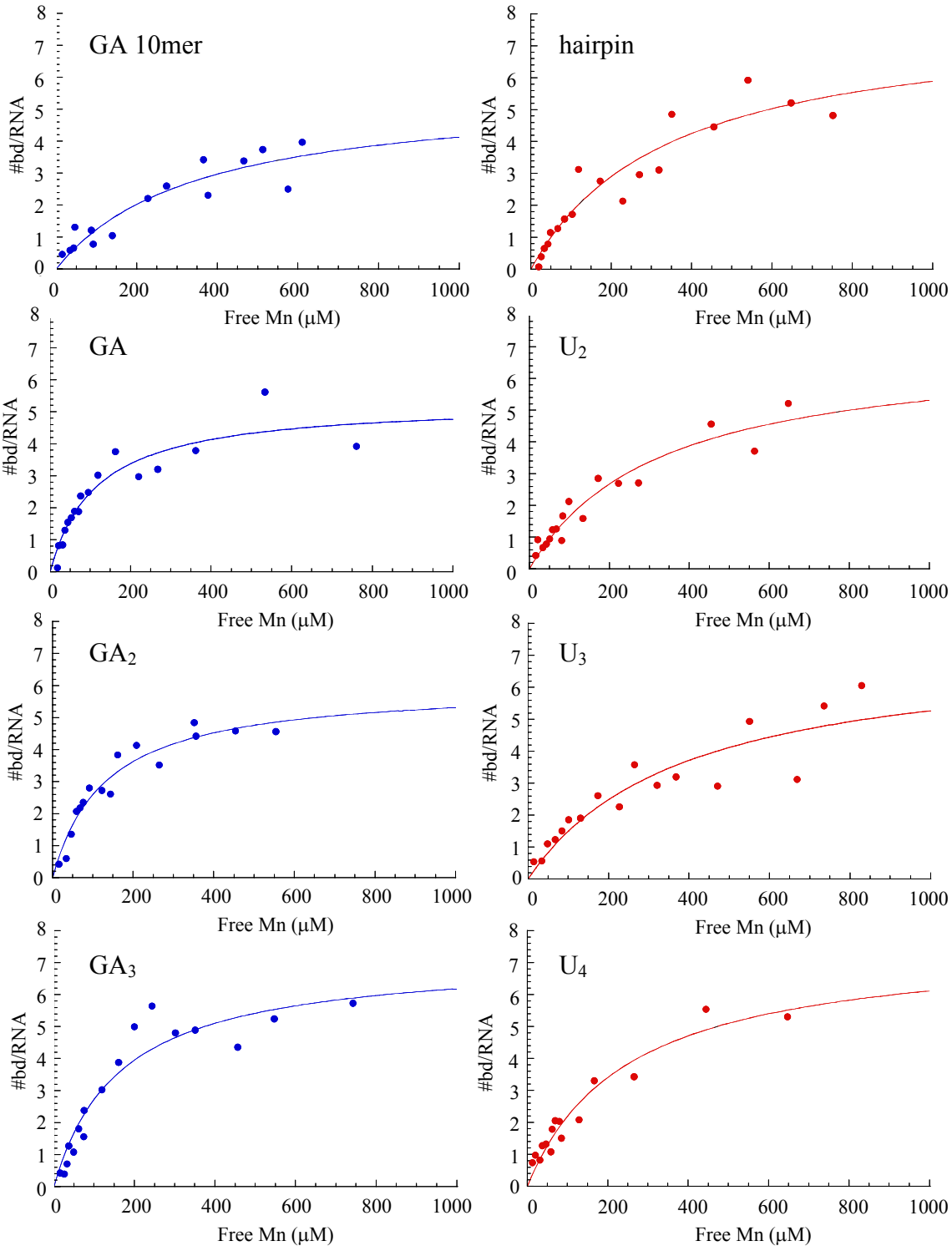

Figure 7-7: RT EPR binding isotherms of loop-containing RNA molecules. The results for all sequences were fit to a single type of site. Conditions were RNA concentration of 10 μM, 100 mM NaCl, 5 mM TEA, pH 7.8 at X-band frequencies.

results for the G-A sequences suggest the presence of both specific and non-specific metal-RNA interactions that are not observed in the UV melting experiment.

Table 7-3: Binding values of Mn^{2+} ion obtained from RT EPR.

RNA	K_d	# bound/RNA
GA 10mer	350 ± 162	5.6 ± 1.2
Hairpin	347 ± 109	7.9 ± 1.2
GA loop	115 ± 26	5.3 ± 0.5
GA_2 loop	131 ± 25	6.0 ± 0.4
GA_3 loop	164 ± 40	7.2 ± 0.7
U_2 loop	326 ± 83	7.0 ± 0.9
U_3 loop	388 ± 152	7.3 ± 1.4
U_4 loop	248 ± 51	7.6 ± 0.8

RNA concentration of 10 μM in 100 mM NaCl, 5 mM TEA, pH 7.8, at X-band. Data was fit to one type of site.

CD spectroscopy

To study the effects that the internal loops, and the metal binding to them, may have on the structure of the RNA sequence, circular dichroism spectroscopy was used to probe for differences in the RNA sequences with and without the addition of Mn^{2+} ions. The obtained ellipticity values in mdegrees were converted to molar residue ellipticity to normalize the signal amplitude by the number of nucleotides in the different RNA sequences.[71] The 200 to 240 nm region of the CD spectrum reports on changes in the backbone of the RNA molecule while the 250 to 300 nm region reports on changes in the base stacking of the RNA.[70] A 13mer duplex was used as a control in order to compare

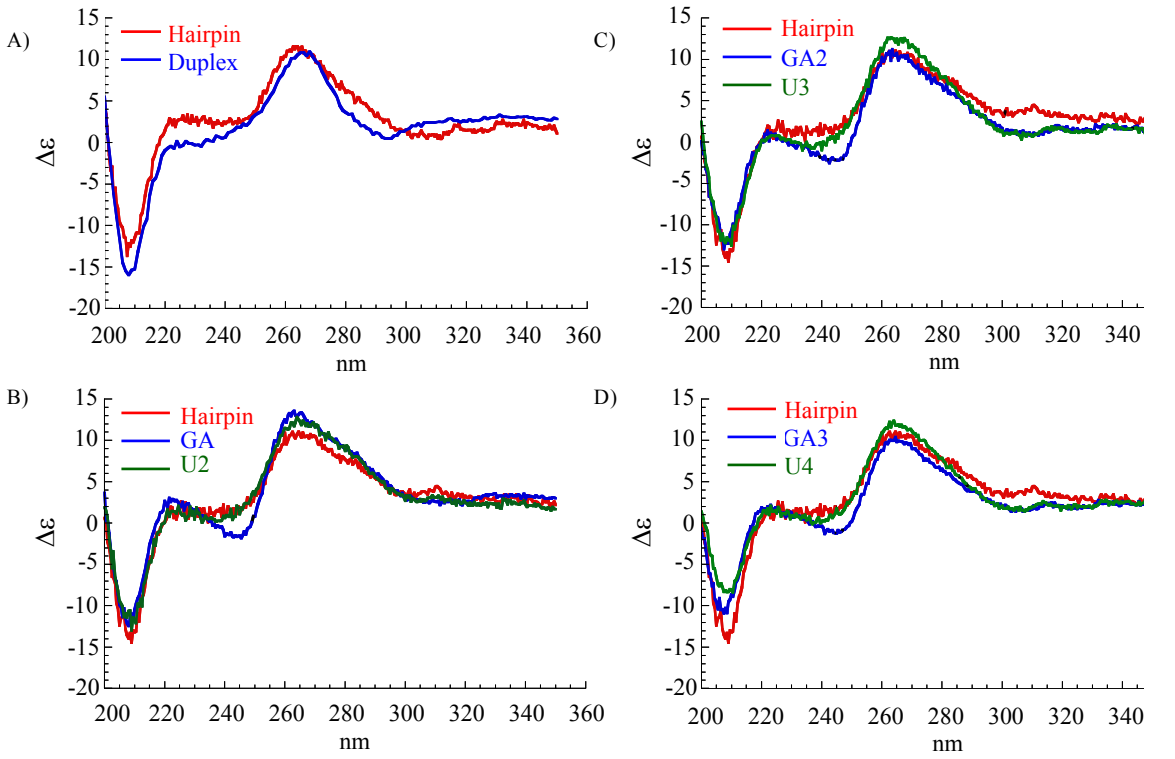

Figure 7-8: CD spectra of loop containing RNA molecules. A) A comparison of a 13nt duplex and the hairpin RNA molecule, B) the hairpin and the GA and U_2, C) the hairpin, GA_2 and U_3, D) the hairpin, GA_3, and U_4. All spectra were acquired at 25ºC, 100 mM NaCl, 5 mM TEA, pH 7.8 and were corrected for the length of the sequence for direct comparison.

the CD signal with and without the tetraloop present. The duplex RNA shows features typical of an A-form helix conformation with a strong, sharp positive ellipticity at 260 nm, and a strong negative ellipticity at 208 nm. The hairpin RNA sequence has similar features as those observed for the duplex except that the feature at 260 nm is broader than that observed for the duplex (see Figure 7-8). The broadening of the 260 nm feature is from the presence of the GAAA tetraloop and is consistent with a previously reported CD spectrum of GAAA hairpin sequence.[127]

The CD spectrum for the GA_3 internal loop sequence (Figure 7-8D) shows the same broad 260 nm feature as observed for the hairpin sequence, consistent with the

presence of the GAAA tetraloop. In the 220 to 240 nm region there are minor positive and negative features that are not seen in either the 13mer duplex or the hairpin spectra. This change can be attributed to slight differences in the backbone of the RNA molecule from the presence of the two sheared G-A mismatches in the internal loop characteristic of this mismatch. The CD spectrum for the U_4 internal loop has the same broad 260 nm feature and an overall similar spectrum to the hairpin.

The CD spectra for the GA containing sequences have similar features at 240 nm that arise from the presence of the sheared G-A mismatch (see Figure 7-8). The CD spectra of the U-U containing sequences are very similar to each other and do not have the small negative feature at 240 nm observed for the G-A containing sequences.

To observe the structural effects that divalent metal ion interactions may have on the internal loops, 1 mM Mn^{2+} was added to the RNA samples of the same concentration and CD spectra were obtained. The results from this experiment showed virtually no change in the CD spectrum upon addition of Mn^{2+} ions, indicating that there are no dramatic structural changes in the RNA molecule in the presence of Mn^{2+} ions (see Figure 7-9). This lack of any change is consistent with the internal loops already having a predefined structure in 100 mM NaCl, with the metal ion-binding site already orientated to accept a metal ion.

Conclusion

The locations of specific metal binding sites are generally found in areas of high negative potential that arise from the folded form of the RNA molecule. The sequences used in this study served as a model system to understand the effect a metal ion may have when bound to a specific site in an RNA molecule. In the presence of divalent ions, a

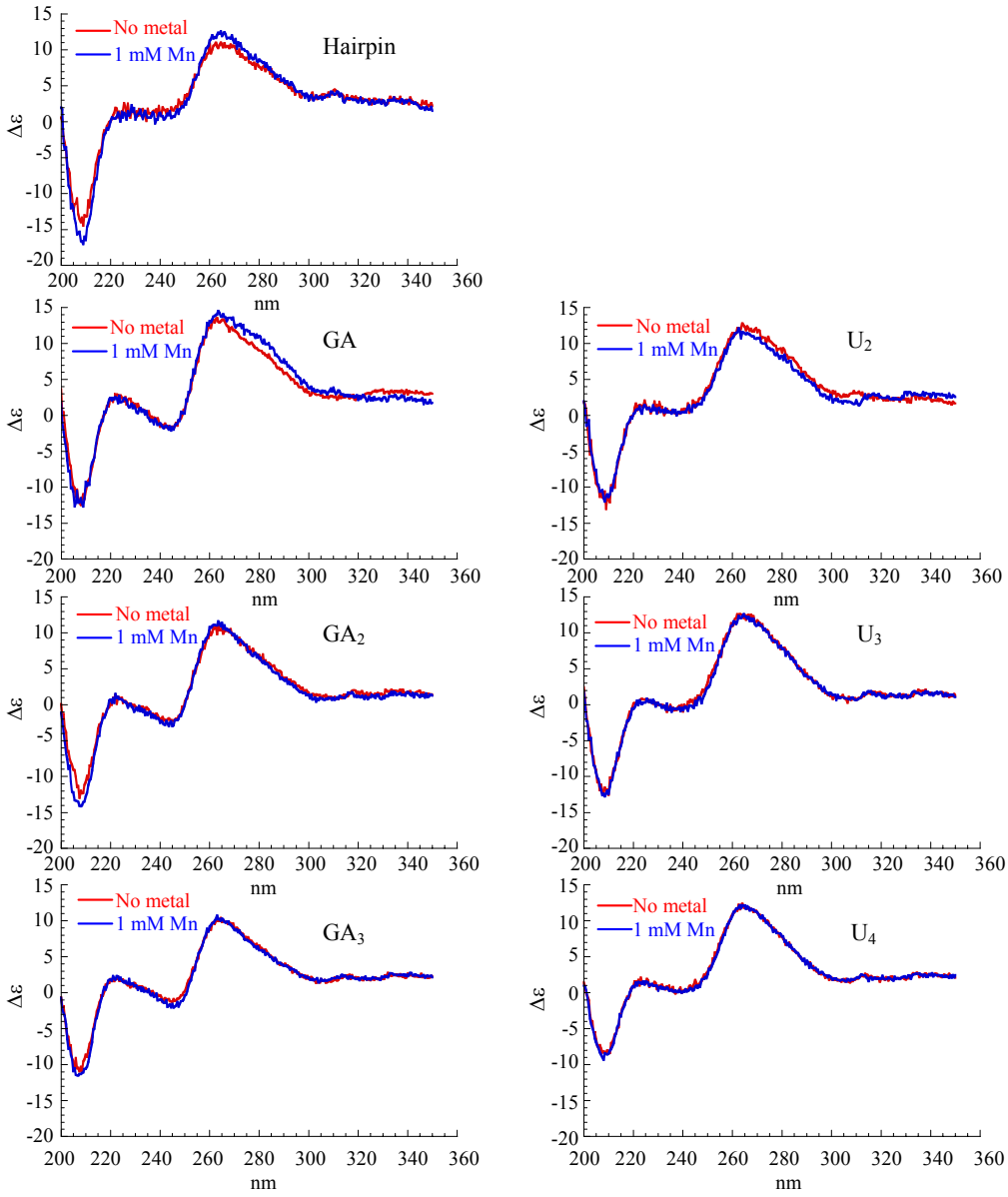

Figure 7-9: CD spectra with addition of 1 mM Mn^{2+} ions. The red lines show the sample without metal and the blue lines are with the addition of 1 mM Mn^{2+}. Conditions were 10 μM RNA, 100 mM NaCl, 5 mM TEA, pH 7.8 at 25ºC

metal binding motif helps to stabilize the RNA and lessen the energetic penalties arising from the mismatched bases in an RNA sequence. Comparing the thermal denaturation results for the G-A and the U-U sequences, the increase in the stability of the RNA molecule with the metal binding motif is more pronounced. The melting profiles for the

U-U sequences become highly destabilized as the length of the loop increases. In the U_4 U-U sequences become highly destabilized as the length of the loop increases. In the U_4 loop, the RNA molecule has become so unstable by the presence of the U-U interactions that the melting profile becomes uncooperative and the hairpin portion of the sequence begins to separate in the melt profile. This is the complete opposite of what is seen for the G-A sequences, which in all cases see an increase in enthalpy as well as retaining the cooperative unfolding transition of the RNA sequence upon addition of Mn^{2+} ions.

The results from RT EPR binding isotherms show a lower K_d value for the G-A containing sequences compared to the hairpin or the U-U containing sequences. The number of bound Mn^{2+} ions to all the RNA sequences was relatively close indicating between five and eight metal ions bound. There was evidence of all the RNA molecules in the sample on average coordinating less than one metal ion bound at low Mn^{2+} concentrations, but no indications of any tight binding sites. Even at the lowest Mn^{2+} concentrations the G-A sequences only bound a fraction of a metal ion. The GA 10mer duplex had an apparent K_d of 350 ± 162 μM for Mn^{2+} in 1 - 0.1 M Na^+ consistent with the results Taira and co-workers observed for the G-A 10mer duplex which was determined to have a Cd^{2+} ion bound with an apparent K_d value of 320 μM in 40 mM Na^+.[126] The GA 10mer duplex has a much higher K_d value than any of the G-A containing capped structures and may reflect more of a general stabilization of the RNA structure than a specific metal ion-binding interaction. This difference can be attributed to the presence of the tetraloop that greatly increases the stability of the capped sequences compared to the duplex sequence. This increased stability of the hairpin sequences helps identify the role of Mn^{2+} ions regarding the interaction with the sheared G-A site.

The apparent K_d values obtained from the EPR and UV experiments are comparable and show they are complementary techniques. The EPR technique provides information on the number of Mn^{2+} ions bound as well as the affinity of metal ion association to the RNA molecule, while the UV method provides information on the extent metal ions can stabilize the RNA structure.

Circular dichroism spectroscopy was employed to observe any differences between the overall structure of the G-A and the U-U containing loops. The G-A containing loop sequences show additional features around 240 nm that are not observed for the 13mer duplex or the hairpin spectra. This feature is a definite signature of the structural change the presence of the G-A sheared mismatch and A-A mismatch have on the RNA structure. The CD spectra for the U-U containing sequences lack the feature at 240 nm and more closely resemble that of the hairpin spectrum. The lack of changes in the CD spectrum upon addition of Mn^{2+} ions to the G-A containing loops is evidence that the G-A and A-A pairings are already in a predefined orientation independent of the presence of divalent metal ions.

The NMR structure of a duplex containing tandem sheared G-A mismatches shows that the phosphate oxygen is only 4.1 Å from the N7 position[106] compared to the 7.6 Å distance for a normal RNA duplex.[128] The positioning of the phosphate group results from the orientation of the sheared G-A mismatch that causes a distortion in the backbone region of the RNA helix compared to a duplex sequence.[106] The electrostatic plot of this sequence shows a region of higher negative potential around the G-A mismatch compared to a duplex strand making this site a good place for a metal ion to coordinate.[118] The coordination of Mn^{2+} ions to the G-A motif in these sequences has

very little structural change on the RNA molecule, although having a definite impact on the thermal stability of the RNA as demonstrated by the UV melting results. Preformed areas in an RNA molecule with high negative potential have a propensity to bind a cation to help stabilize the RNA structure through charge neutralization.[10] The lack of any dramatic structural change when the Mn^{2+} ion binds must be due to the metal ions having only an electrostatic stabilization on the RNA.

Although they both contain the same sheared G-A metal ion-binding motif, the hammerhead ribozyme and the G-A containing sequences have a 10 fold difference in the K_d values obtained by room temperature EPR binding isotherms. There are two possibilities for the discrepancy in the K_d values, an area of greater negative potential or greater structural stabilization of the the hammerhead. The hammerhead ribozyme is a compactly folded RNA that creates an area of high negative potential at the A9/G10.1 site. The core of the hammerhead has been shown to undergo a folding transition with the addition of Mg^{2+} ions. The binding of a metal ion at this site aids in the formation of the core to the folded form and may have an allosteric effect that stabilizes the entire core. If the metal ion binding to the RNA has this structural role, the interaction would be expected to be stronger because the energetic penalties associated with tightly binding a metal ion would be compensated by the gained stabilization of the folded form of the hammerhead ribozyme.

CHAPTER VIII

CONCLUSIONS

Conclusion

The work described in this thesis demonstrates the use of a multitude of spectroscopic techniques and computer based models to understand and characterize metal-RNA interactions under solution conditions. The coordination of cations to RNA molecules is essential to alleviate the negative charge of the phosphodiester backbone. X-ray crystal structures of RNA molecules can show potential metal ion binding sites, however, they do not show the apparent affinity for the metal ion binding to that site. The metal ion binding properties of the hammerhead ribozyme and a series of RNA molecules containing a metal ion-binding motif were extensively studied to understand the effect the metal ion has on biomolecules.

A combination of EPR and ESEEM techniques were employed to study the high affinity Mn^{2+} ion binding site in the hammerhead ribozyme and determine the exact location of the site. At high salt concentrations the hammerhead binds a single Mn^{2+} ion that has a characteristic low temperature EPR signal. This Mn^{2+} ion was conclusively proven to coordinate at the G10.1 by using site specific ^{15}N labeling of the guanine residue and ESEEM spectroscopy. These results conclusively prove the metal ion observed in the crystal structure bound at the A9/G10.1 site is the high affinity metal ion site in the hammerhead under solution conditions.

The hydration level of the high affinity Mn^{2+} ion was also determined by ESEEM to have 4.02 ± 0.12 coordinated water molecules. The high hydration level of the Mn^{2+} ion is consistent with the high energetic penalty associated with removing a coordinated

water molecule from the metal ion. The specific nature of the coordination environment of the high affinity Mn^{2+} ion is a clear indication of the A9/G10.1 site being structurally important to alleviate local negative potential and aid in the formation of the hammerhead's conserved core.

Using the results obtained in the work shown here in conjunction with previous ^{31}P ENDOR results[21] a molecular mechanics model of the Mn^{2+} ion coordinated at the high affinity site was constructed. The model showed the A9/G10.1 site in the hammerhead has the nitrogen and phosphate ligands positioned in a manner to coordinate a metal ion. These results for the high affinity site in the hammerhead are a paradigm for the further understanding and characterization of metal ion binding properties to RNA molecules through a combination of crystallographic and solution techniques.

The understanding of the differences between specific and non-specific metal ion interactions with RNA is of paramount importance in determining the role the metal ions have in stabilizing the structure of the RNA molecule. Distinguishing between specific and non-specific metal ion binding sites was achieved by comparing the room temperature Mn^{2+} binding isotherms obtained for the hammerhead ribozyme with the results from the 13nt RNA duplex. The RNA duplex coordinates 3-4 Mn^{2+} ions with a relatively weak apparent K_d of ~ 150 μM compared to the 2-3 tight sites with an apparent K_d of ~ 2 μM for the hammerhead.

Microwave power saturation was employed to study the proximity of multiple Mn^{2+} ions coordinated to the hammerhead under solution conditions and to determine if they are the same sites observed in the crystal structure. At four equivalents of Mn^{2+} ions to hammerhead RNA, the power saturation plot has an increase in the $P_{1/2}$ value

indicating that the metal ions are relatively close in proximity and provide additional relaxation pathways for each other. Comparative studies with the 13nt RNA duplex and buffer samples show little to no change in the observed $P_{1/2}$ values indicating the difference must arise from the metal ions coordinated to the hammerhead ribozyme and are most likely in similar sites as those observed in the crystal structure.

The Mn^{2+} EPR spectra of several model complexes were studied to understand the origin of the 6^{th} line spectral feature of the EPR spectrum observed for the high affinity Mn^{2+} ion bound to the hammerhead. Changes in the ligand environment of the Mn^{2+} ion produced varying effects on the EPR lineshape. The Mn-GMP spectrum had a slight line broadening, while the Mn-GTP spectrum had extreme line broadening. The Mn^{2+} ion in a mixed coordination environment with a high concentration of Cl^- ions yielded a spectrum with more resolved features similar to the high affinity spectrum observed for the hammerhead. Simulations of the Mn^{2+} EPR spectrum for the A9/G10.1 metal site showed severe rhombic distortion of the zero field splitting parameter with a value of 173 MHz for E compared to the E value of 90 MHz obtained for the Mn^{2+} in buffer spectrum. The coordination environment of the Mn^{2+} ion at the A9/G10.1 site causes a distinctive distortion in the geometry of the metal ion when bound at this site accounting for the signature EPR spectrum observed for the hammerhead high affinity site.

X-ray techniques were used to provide a unique characterization of the metal ion coordination sphere bound to the hammerhead and model complexes. Mn^{2+} EXAFS studies of model complexes of Mn-GMP and Mn-phosphate crystals provided a foundation for the understanding the source of the EXAFS results previously obtained for the hammerhead ribozyme high affinity metal ion site. EXAFS studies also characterized

the metal ion coordination sphere with the presence of a phosphorothioate substitution at the A9 site. Cd^{2+} EXAFS results demonstrated the coordination of the metal ion to both Rp and Sp isomers of the A9 phosphorothioate. These results are consistent with previous results obtained by ^{31}P NMR indicating the Cd^{2+} ion coordinates to the sulfur of both Rp and Sp phosphorothioate isomers.[53]

Molecular modeling demonstrated the effect the phosphorothioate substitution has on the metal coordination properties and explains the EXAFS results. Previous EXAFS results led to a hypothesis that the Mn^{2+} ion coordinates to the Sp oxygen of the Rp sulfur substitution and twists the RNA structure.[105] The molecular models shown here for the Mn^{2+} Rp S coordinated to the oxygen atom at the Sp position suggests a twist of the phosphate group occurs that distorts the RNA structure. The Cd^{2+} ion, with a slightly larger ionic radius than the Mn^{2+} ion, coordinates to the sulfur atom of both the A9 Rp and Sp isomers with minimal disturbance to the overall RNA structure and as demonstrated by the molecular models.

The Mn^{2+} ion binding properties of a series of RNA hairpin molecules with symmetrical internal loops containing the sheared G-A metal ion binding motif found in various RNA sequences including the hammerhead was extensively characterized. The internal loop had from 0 to 2 A-A mismatches separating the G-A mismatches. Comparisons were made to a hairpin sequence without an internal loop and sequences containing internal loops containing only U-U mismatches. The G-A mismatch containing sequences showed a much greater change in thermal stability upon addition of Mn^{2+} ions compared to the U-U containing sequences. The G-A mismatch containing sequences also had a lower apparent K_d value of approximately 120 μM for bound Mn^{2+}

ions than the other sequences studied. The binding of a metal ion to the G-A containing sequences, however, is not as tight as the G-A binding site in the hammerhead ribozyme. This difference must arise from either the electrostatic potential between the molecules or the structural role the coordination of the metal ion has in the hammerhead ribozyme to stabilize the folded form.

Future work

Minimal hammerhead

Although these studies presented here have located the position of the high affinity site as well as understanding of multiple metal ion interactions with the hammerhead, there are still several areas that are not yet well understood. Determining the second metal ion-binding site will provide a comparison to see if another site observed in the crystal structure. One possible method is to bind an EPR silent metal ion at the A9/G10.1 site to block the coordination of the Mn^{2+} ion. This could be accomplished by placing a sulfur substitution at the A9 site, which binds a Cd^{2+} ion more tightly than a Mn^{2+} ion. Addition of the Mn^{2+} ion should coordinate to the next highest affinity site and EPR techniques can be employed to characterize the coordination environment. This may, however, prove difficult if the binding site for the second ion is not as well defined as the A9/G10.1 site.

The exact role of the metal ion located at the A9/G10.1 site is still uncertain. Although the EPR studies shown here have provided the location of the metal ion, further experiments are required to understand its function in the hammerhead. Lilley and coworkers have had success in studying the formation of the conserved core and the folding pathway using FRET and ^{19}F NMR techniques. The folding pathway upon

addition of divalent ions to the hammerhead with mutations at the A9/G10.1 site can be studied using ^{19}F NMR and any alterations can reveal the structural role of the metal ion. Placement of a phosphorothioate at the A9 Rp position can test the hypothesis of the Mn^{2+} ion binding to the Sp oxygen. According to the molecular models, this type of coordination effectively twists the phosphate group in the opposite direction and effects the formation of the conserved core. Placing a 5-fluorouridine probe at the U7 position of the conserved core, the formation of domain 2 can be monitored with the addition of Mn^{2+} ions. If the folding pathway is disrupted, it should be reflected in the results for the ^{19}F titration. A similar titration experiment can be done using a Cd^{2+} ion to observe if there are any changes in the formation of domain 2 with the A9 sulfur Rp and Sp isomers.

The extended hammerhead

Some interesting results involving an extended hammerhead sequence have been published and much interest has been shown for this new construct.[129,130] The extended hammerhead sequence contains two interacting loops that more closely resembles the natural form found in the viroid genome. The most significant result found so far for the extended hammerhead is that it is catalytically active at a much lower concentration of Mg^{2+} ions compared to the minimal form. Some initial metal ion binding studies have been performed, but the Mn^{2+} ion binding characteristics have not yet been investigated.

Room temperature Mn^{2+} EPR binding isotherms can be used to characterize the number and affinities of the extended hammerhead sequence and how it compares to the minimal hammerhead. Salt competition studies can be used to isolate any strong metal ion binding sites and low temperature EPR studies to check for the presence of a Mn^{2+} ion coordinated to the A9/G10.1 site. The comparison between the minimal and

extended hammerhead sequences may provide information on whether the A9/G10.1 metal ion has a structural or functional role in the natural ribozyme or just important for the truncated form.

Paramagnetic probes

The spectroscopically active Mn^{2+} ion makes an ideal substitute for Mg^{2+} to investigate the coordination properties of metal ions in RNA molecules. One drawback of using Mn^{2+} as a probe is the complex EPR spectrum arising from the S = 5/2 and I = 5/2 values. Other EPR active transition metals have potential to be used as paramagnetic probes to study metal RNA interactions. The use of different metal ions can be used to exploit their inherent physical properties such as size and binding propensity to probe RNA binding sites.

A potentially good candidate for an EPR spectroscopic probe is the Cu^{2+} ion with an S = ½ and has an axial EPR spectrum. The $g_{\|}$ value is sensitive to the type of ligands coordinating the metal ion in the plane.[131] The $g_{\|}$ value will shift depending on the presence of either oxygen, nitrogen or sulfur ligands and allows for easy determination of the type of ligands coordinated to the Cu^{2+} ion from the EPR spectrum. Cu^{2+} is a soft metal ion and is more thiophilic than Mn^{2+} making the sulfur of a phosphorothioate substitution a potentially good ligand. A combination of EPR, ENDOR and ESEEM techniques can be used to fully characterize the coordination environment of the Cu^{2+} ion to an RNA molecule.

Metal ion binding motifs

The Mn^{2+} ion binding properties of the RNA sequences containing the sheared G-A motif showed several interesting trends. A potential interest would be to see the effect

on the Mn^{2+} ion binding properties of an asymmetrical loop containing the sheared G-A motif. The presence of an asymmetrical loop could cause a kink in the RNA structure and the binding of metal ion at the motif may possible affect the RNA structure. Similar studies as done for the sheared G-A sequences can be performed to observe the melting dependence of the asymmetrical RNA sequence upon addition of Mn^{2+} ions as well as to observe any changes in the room temperature EPR binding isotherms compared to the symmetrical loop sequences.

Other possible avenues of pursuit are changing the composition of the internal loop to have a series of different mismatches and possibly the study of different metal ion-binding motif. The G-U wobble base pair is one possible mismatch that can be investigated for potential metal ion binding properties. This mismatch has been shown to be important for recognition of a variety of different molecules including metal ions. The G-U wobble may potentially have specific interactions with a divalent metal ion affecting the structure of the RNA molecule in the presence of the metal ions. Sequences can be developed containing a G-U wobble with different mismatched nucleotides around it to see the effect it has on the RNA metal ion binding properties and compare it to the results of the sheared G-A containing sequences. Other changes can also be done to observe differences in metal ion binding properties between the internal loops.

REFERENCES

1. Mathews, C. K.; Van Holde, K. E. *Biochemistry*, 2nd ed.; Benjamin/Cummings Publishing Company, Inc.: New York, 1996.

2. Tinoco, I. *J. Phys. Chem.* **1996**, *100*, 13311-13322.

3. Westhof, E.; Fritsch, V. *Structure Fold. Des.* **2000**, *8*, R55-65.

4. Zorn, J.; Gan, H. H.; Shiffeldrim, N.; Schlick, T. *Biopolymers* **2004**, *73*, 340-347.

5. Biou, V.; Yaremchuk, A.; Tukalo, M.; Cusack, S. *Science* **1994**, *263*, 1404-1410.

6. Gueron, M.; LeRoy, J. L. *Biophys. J.* **1982**, *38*, 231-236.

7. Pyle, A. M. *J. Biol. Inorg. Chem.* **2002**, *7*, 679-690.

8. Misra, V. K.; Draper, D. E. *Biopolymers* **1998**, *48*, 113-135.

9. Misra, V. K.; Draper, D. E. *Proc. Natl. Acad. Sci. U.S.A.* **2001**, *98*, 12456-12461.

10. Draper, D. E. *RNA* **2004**, *10*, 335-343.

11. Mundoma, C.; Greenbaum, N. L. *J. Am. Chem. Soc.* **2002**, *124*, 3525-3532.

12. Mundoma, C.; Greenbaum, N. L. *Biopolymers* **2003**, *69*, 100-109.

13. Walter, N. G.; Yang, N.; Burke, J. M. *J. Mol. Biol*. **2000**, *298*, 539-555.

14. Feig, A. L.; Panek, M.; Horrocks, W. D.; Uhlenbeck, O. C. *Chem. Biol.* **1999**, *6*, 801-810.

15. Rudisser, S.; Tinoco, I. *J. Mol. Biol.* **2000**, *295*, 1211-1223.

16. Gonzalez, R. L.; Tinoco, I. *J. Mol. Biol.* **1999**, *289*, 1267-1282.

17. Douglas, B.; McDaniel, D.; Alexander, J. *Concepts and Models of Inorganic Chemistry,* 3rd ed.; 1994.

18. Leroy, J. L.; Gueron, M.; Thomas, G.; Favre, A. *Eur. J. Biochem*. **1977**, *74*, 567-574.

19. Horton, T. E.; Clardy, D. R.; DeRose, V. J. *Biochemistry* **1998**, *37*, 18094-18101.

20. Morrissey, S. R.; Horton, T. E.; Grant, C. V.; Hoogstraten, C. G.; Britt, R. D.; DeRose, V. J. *J. Am. Chem. Soc.* **1999**, *121*, 9215-9218.

21. Morrissey, S. R.; Horton, T. E.; DeRose, V. J. *J. Am. Chem. Soc.* **2000**, 121, 9215-9218.

22. Schiemann, O.; Fritscher, J.; Kisseleva, N.; Sigurdsson, S. T.; Prisner, T. F. *ChemBioChem* **2003**, *4*, 1057-1065.

23. Hansen, M. R.; Simorre, J. P.; Hanson, P.; Mokler, V.; Bellon, L.; Beigelman, L.; Pardi, A. *RNA* **1999**, *5*, 1099-1104.

24. DeRose, V. J. *Chem. Biol.* **2002**, *9*, 961-969.

25. Lilley, D. M. *Trends Biochem. Sci.* **2003**, *28*, 495-501.

26. Kruger, K.; Grabowski, P. J.; Zaug, A. J.; Sands, J.; Gottschling, D. E.; Cech, T. R. *Cell* **1982**, *31*, 147-157.

27. Guerrier-Takada, C.; Gardiner, K.; Marsh, T.; Pace, N.; Altman, S. *Cell* **1983**, *35*, 849-857.

28. DeRose, V. J. *Curr. Opin. Struct. Biol.* **2003**, *13*, 317-324.

29. Symons, R. *Nucleic Acids Res.* **1997**, *25*, 2683-2689.

30. Bassi, G. S.; Murchie, A. I.; Lilley, D. M. *RNA* **1996**, *2*, 756-768.

31. Bassi, G. S.; Mollegaard, N. E.; Murchie, A. I.; Lilley, D. M. *Biochemistry* **1999**, *38*, 3345-3354.

32. Ruffner, D. E.; Stormo, G. D.; Uhlenbeck, O. C. *Biochemistry* **1990**, *29*, 10695-10702.

33. Peracchi, A.; Beigelman, L.; Scott, E. C.; Uhlenbeck, O. C.; Herschlag, D. *J. Biol. Chem.* **1997**, *272*, 26822-26826.

34. Peracchi, A.; Beigelman, L.; Usman, N.; Herschlag, D. *Proc. Natl. Acad. Sci. U.S.A.* **1996**, *93*, 11522-11527.

35. Baidya, N.; Uhlenbeck, O. C. *Biochemistry* **1997**, *36*, 1108-1114.

36. Curtis, E. A.; Bartel, D. P. *RNA* **2001**, *7*, 546-552.

37. Murray, J. B.; Seyhan, A. A.; Walter, N. G.; Burke, J. M.; Scott, W. G. *Chem. Biol.* **1998**, *5*, 587-595.

38. O'Rear, J. L.; Wang, S.; Feig, A. L.; Beigelman, L.; Uhlenbeck, O. C.; Herschlag, D. *RNA* **2001**, *7*, 537-545.

39. Pley, H. W.; Lindes, D. S.; DeLuca-Flaherty, C.; McKay, D. B. *J. Biol. Chem.* **1993**, *268*, 19656-19658.

40. Pley, H. W.; Lindes, D. S.; DeLuca-Flaherty, C.; McKay, D. B. *Nature* **1994**, *372*, 68-74.

41. Scott, W. G.; Finch, J. T.; Klug, A. *Cell* **1995**, *81*, 991-1002.

42. Scott, W. G.; Murray, J. B.; Arnold, J. R. P.; Stoddard, B. L.; Klug, A. *Science* **1996**, *274*, 2065-2069.

43. Murray, J. B.; Dunham, C. M.; Scott, W. G. *J. Mol. Biol.* **2002**, *315*, 121-130.

44. Wedekind, J. E.; McKay, D. B. *Annu. Rev. Bioph. Biom.* **1998**, *27*, 475-502.

45. Bondensgaard, K.; Mollova, E. T.; Pardi, A. *Biochemistry* **2002**, *41*, 11532-11542.

46. Bassi, G. S.; Mollegaard, N. E.; Murchie, A. I.; von Kitzing, E.; Lilley, D. M. *Nat. Struct. Biol* **1995**, *2*, 45-55.

47. Bassi, G. S.; Murchie, A. I.; Walter, F.; Clegg, R. M.; Lilley, D. M. *EMBO J.* **1997**, *16*, 7481-7489.

48. Hammann, C.; Norman, D. G.; Lilley, D. M. *Proc. Natl. Acad. Sci. U.S.A.* **2001**, *98*, 5503-5508.

49. Wang, S.; Karbstein, K.; Peracchi, A.; Beigelman, L.; Herschlag, D. *Biochemistry*, **1999**, *38*, 14363-14378.

50. Murray, J. B.; Scott, W. G. *J. Mol. Biol.* **2000**, *296*, 33-41.

51. Hunsicker, L. M.; DeRose, V. J. *J. Inorg. Biochem.* **2000**, *80*, 271-281.

52. Horton, T. E.; DeRose, V. J. *Biochemistry* **2000**, *39*, 11408-11416.

53. Maderia, M.; Hunsicker, L. M.; DeRose, V. J. *Biochemistry* **2000**, *39*, 12113-12120.

54. Morrissey, S. R. Ph.D. Dissertation, Texas A&M University, College Station, TX, 1999.

55. Misra, S. K. *Physica B* **1997**, *240*, 183-197.

56. Stoll, S. Ph.D. Dissertation, EHTZ, Zurich, Switzerland 2003.

57. Reed, G. H.; Markham, G. D. *Biological Mag. Res.* **1984**, *6*, 73-142.

58. Woody, A. M.; Eaton, S. S.; Osumi-Davis, P. A.; Woody, R. W. *Biochemistry* **1996**, *35*, 144-152.

59. Addona, G. H.; Andrews, S. H.; Cafiso, D. S. *Biochim. Biophys. Acta* **1997**, *1329*, 74-84.

60. Subczynski, W. K.; Hyde, J. *Biochim. Biophys. Acta* **1981**, *643*, 283-291.

61. McCracken, J. In *Handbook of Electron Spin Resonance Vol. 2*; Poole, C. P.; Farach, H. A., Eds; Springer-Verlag, Inc.: New York 1994, 375.

62. Hoogstraten, C. G.; Grant, C. V.; Horton, T. E.; DeRose, V. J.; Britt, R. D. *J. Am. Chem. Soc.* **2002**, *124*, 834-842.

63. Sturgeon, B. E.; Britt, R. D. *Rev. Sci. Instrum.* **1992**, *63*, 2187-2192.

64. Sturgeon, B. E.; Ball, J. A.; Randall, D. W.; Britt, R. D. *J. Phys. Chem*. **1994**, *98*, 12871-12883.

65. Kevan, L. In *Time Domain Electron Spin Resonance*: Kevan, L.; Schwartz, R. N. Eds.; John Wiley & Sons, Inc.: New York 1979, 424.

66. Mims, W. B.; Peisach, *J. Biol. Magn. Reson.* **1981**, *3*, 213-263.

67. Hoostraten, C. G.; Britt, R. D. *RNA* **2002**, *8*, 252-260.

68. Christopher, J., *Tmelt*; Texas A&M University, College Station, TX, 1998.

69. Gluick, T. C.; Wills, N. M.; Gesteland, R. F.; Draper, D. E. *Biochemistry* **1997**, *36*, 16173-16186.

70. Agris, P. F.; Brown, S. C. *Methods in Enzymol.* **1995**, *117*, 270-299.

71. Proctor, D. J.; Schaak, J. E.; Bevilacqua, J. M.; Falzone, C. J.; Bevilacqua, P. C. *Biochemistry* **2002**, *41*, 12062-12075.

72. Scott, R. A. *Methods in Enzymol.* **1985**, *261*, 414-459.

73. De Meester, P.; Goodgame, D. M.; Jones, T. J.; Skapski, A. C. *Biochem. J.* **1974**, *139*, 791-792.

74. Aranda, M. A. G.; Attfield, J. P.; Bruque, S. *Inorg. Chem.* **1993**, *32*, 1925-1930.

75. Hammann, C.; Lilley, D. M. J. *ChemBioChem* **2002**, *3*, 691-700.

76. Wedekind, J. E.; McKay, D. B. *Nature Struct. Biol.* **1999**, *6*, 261-268.

77. Ferre-D'Amare, A. R.; Rupert, P. B. *Biochemical Soc. T.* **2002**, *30*, 1105-1109.

78. Yoshinari, K.; Taira, K. *Nucleic Acid Res.* **2000**, *28*, 1730-1742.

79. Danchin, A.; Gueron, M. *Eur. J. Biochem.* **1970**, *16*, 532-536.

80. Sabet, M.; Cini, R.; Haromy, T.; Sundaralingam, M. *Biochemistry* **1985**, *24*, 7827-7833.

81. Mollova, E. T.; Hansen, M. R.; Pardi, A. *J. Am. Chem. Soc.* **2000**, *122*, 11561-11562.

82. Forester, A. C.; Symons, R. H. *Cell* **1987**, *49*, 211-220.

83. Dahm, S. C.; Uhlenbeck, O. C. *Biochemistry* **1991**, *30*, 9464-9469.

84. Murray, J. B.; Terwey, D. P.; Maloney, L.; Karpeisky, A.; Usman, N.; Beigelman, L.; Scott, W. G. *Cell* **1998**, *92*, 665-673.

85. Feig, A. L.; Scott, W. G.; Uhlenbeck, O. C. *Science* **1998**, *279*, 81-84.

86. Portis, A. M. *Phys. Rev.* **1953**, *91*, 1071-1078.

87. Rupp, R.; Rao, K. K.; Hall, P. O.; Cammack, R. *Bioch. Biophys. Acta* **1978**, *91*, 1071-1078.

88. Goodman, G.; Leigh, J. S. *Biochemistry* **1985**, *24*, 2310-2317.

89. Melrovitch, E.; Poupko, R. J. *Phys. Chem.* **1978**, *82*, 1920-1925.

90. Allen, B. T. *J. Chem. Phys*. **1965**, *43*, 3820-3826.

91. Tan, X. L.; Bernardo, M.; Thomann, H.; Scholes, C. P. *J. Chem. Phys.* **1993**, *98*, 5147-5157.

92. Coffino, A. R.; Peisach, J. *J. Magn. Reson. B* **1996**, *111*, 127-134.

93. Chan, S. I.; Fung, B. M.; Lutje, H. *J. Chem. Phys.* **1967**, *47*, 2121-2130.

94. Levanon, H.; Luz. Z. *J. Chem. Phys.* **1968**, *49*, 2031-2040.

95. Allen, B. T.; Nebert, D. W. *J. Chem. Phys.* **1964**, *41*, 1983-1985.

96. Tsay, F. D.; Manatt, S. L.; Chan, S. I. *Chem. Phys. Letters* **1972**, *17*, 223-226.

97. Tan, X. S.; Xiang, D. F.; Tang, W. X.; Sun, J. *Polyhedron* **1997**, *16*, 689-694.

98. Misra, S. K. *Physica B* **1994**, *203*, 193-200.

99. Charnock, J. M. *Rad. Phys. Chem.* **1995**, *45*, 385-391.

100. Cramer, S. P.; Gillum, W. O.; Hodgson, K. O.; Mortenson, L. E.; Stiefel, E. I.; Chisnell, J. R.; Brill, W. J.; Shah, V. K. *J. Am. Chem. Soc.* **1978**, *100*, 3814-3819.

101. Cramer, S. P.; Hodgson, K. O.; Gillum, W. O.; Mortenson, L. E. *J. Am. Chem. Soc.* **1978**, *100*, 3398-3407.

102. DeRose, V. J.; Mukerji, I.; Latimer, M. J.; Yachandra, V. K.; Sauer, K.; Klein, M. P. *J. Am. Chem. Soc.* **1994**, *116*, 5239-5249.

103. Fujii, K.; Akamatsu, K.; Yokoya, A. *J. Phys. Chem. B* **2004**, *108*, 8031-8035.

104. Cech, T. R.; Golden, B. L. In *The RNA World,* 2nd ed.; Gesteland, R. F.; Cech, T. R.; Atkins, J. F., Eds; Cold Spring Harbor Laboratory Press: New York, 1999, 321.

105. Hunsicker, L. M. Ph.D. Dissertation, Texas A&M University, College Station, TX, 2001.

106. Wu, M.; Turner, D. H. *Biochemistry* **1996**, *35*, 9677-89.

107. Ruffner, D. E.; Uhlenbeck, O. C. *Nucleic Acids Res.* **1990**, *18*, 6025-6029.

108. Leontis, N. B.; Westhof, E. *Curr. Opin. Struct. Biol.* **2003**, *13*, 300-308.

109. Meroueh, M.; Chow, C. S. *Nucleic Acids Res.* **1999**, *27*, 1118-1125.

110. Kim, J.; Walter, A. E.; Turner, D. H. *Biochemistry* **1996**, *35*, 13753-13761.

111. Longfellow, C. E.; Kierzek, R.; Turner, D. H. *Biochemistry* **1990**, *29*, 278-285.

112. SantaLucia, J.; Kierzek, R.; Turner, D. H. *Biochemistry* **1990**, *29*, 8813-8819.

113. SantaLucia, J.; Kierzek, R.; Turner, D. H. *Biochemistry* **1991**, *30*, 8242-8251.

114. SantaLucia, J.; Turner, D. H. *Biopolymers* **1997**, *44*, 309-319.

115. Schroeder, S. J.; Kim, J.; Turner, D. H. *Biochemistry* **1996**, *35*, 16105-16109.

116. Schroeder, S. J.; Turner, D. H. *Biochemistry*, **2000**, *39*, 9257-9274.

117. Schroeder, S. J.; Turner, D. H. *Biochemistry*, **2001**, *40*, 11509-11517.

118. Chin, K.; Sharp, K. A.; Honig, B.; Pyle, A. M. *Nat. Struct. Biol.* **1999**, *6*, 1055-1061.

119. Wu, M.; McDowell, J. A.; Turner, D. H. *Biochemistry* **1995**, *34*, 3204-3211.

120. Villescas-Diaz, G.; Zacharias, M. *Biophys. J.* **2003**, *85*, 416-425.

121. SantaLucia, J.; Turner, D. H. *Biochemistry* **1993**, *32*, 12612-12623.

122. Ebel, S.; Brown, T.; Lane, A. N. *Eur. J. Biochem.* **1994**, *220*, 703-715.

123. Baeyens, K. J.; DeBondt, H. L.; Pardi, A.; Holbrook, S. R. *Proc. Natl. Acad. Sci. U.S.A.* **1996**, *93*, 12851-12855.

124. Tanaka, Y.; Kojima, C.; Morita, E. H.; Kasai, Y.; Yamasaki, K.; Ono, A.; Kainosho, M.; Taira, K. *J. Am. Chem. Soc.* **2002**, *124*, 4595-4601.

125. Tanaka, Y.; Morita, E. H.; Hayashi, H.; Kasai, Y.; Tanaka, T.; Taira, K. *J. Am. Chem. Soc.* **2000**, *122*, 11303-11310.

126. Tanaka, Y.; Kasai, Y.; Mochizuki, S.; Wakisaka, A.; Morita, E. H.; Kojima, C.; Toyozawa, A.; Kondo, Y.; Taki, M.; Takagi, Y.; Inoue, A.; Yamasaki, K.; Taira, K. *J. Am. Chem. Soc.* **2004**, *126*, 744-752.

127. Greenbaum, N. L.; Mundoma, C.; Peterman, D. R. *Biochemistry* **2001**, *40*, 1124-1134.

128. Klosterman, P.S.; Shah, S. A.; Steitz, T. A. *Biochemistry* **1999**, *38*, 14784-14792.

129. Khvorova, A.; Lescoute, A.; Westhof, E.; Jayasena, S. D. *Nat. Struct. Biol.* **2003**, *10*, 708-712.

130. Penedo, J. C.; Wilson, T. J.; Jayasena, S. D.; Khvorova, A.; Lilley, D. M. *RNA* **2004**, *10*, 880-888.

131. Peisach, J.; Blumberg, W. E. *Ach. Biochem. Biophys.* **1974**, *165*, 691-708.

APPENDIX

Table A-1: Crystal data and structure refinement for Mn-GMP.

Identification code	vdr01	
Empirical formula	C10 H28 Mn N5 O16 P	
Formula weight	560.28	
Temperature	110(2) K	
Wavelength	0.71073 Å	
Crystal system	Monoclinic	
Space group	C2	
Unit cell dimensions	a = 27.851(10) Å	α= 90°.
	b = 11.136(4) Å	β= 93.312(7)°.
	c = 6.674(2) Å	γ = 90°.
Volume	2066.5(13) $Å^3$	
Z	4	
Density (calculated)	1.801 Mg/m^3	
Absorption coefficient	0.809 mm^{-1}	
F(000)	1164	
Crystal size	0.30 x 0.10 x 0.10 mm^3	
Theta range for data collection	3.66 to 24.99°.	
Index ranges	-33<=h<=30, -13<=k<=10, -7<=l<=7	
Reflections collected	4776	
Independent reflections	2880 [R(int) = 0.0786]	
Completeness to theta = 24.99°	95.2 %	
Absorption correction	None	
Max. and min. transmission	0.9235 and 0.7933	
Refinement method	Full-matrix least-squares on F^2	
Data / restraints / parameters	2880 / 181 / 298	
Goodness-of-fit on F^2	1.035	
Final R indices [I>2sigma(I)]	R1 = 0.0793, wR2 = 0.1762	
R indices (all data)	R1 = 0.1011, wR2 = 0.1837	
Absolute structure parameter	0.01(4)	
Largest diff. peak and hole	1.029 and -0.878 $e.Å^{-3}$	

Table A-2: Atomic coordinates for Mn-GMP.

	x	y	z	U(eq)
Mn(1)	6450(1)	12031(1)	7647(2)	18(1)
P(1)	7425(1)	8372(2)	7419(3)	18(1)
O(1)	6965(2)	13528(6)	7431(9)	21(2)
O(2)	6245(2)	12764(6)	10583(9)	22(1)
O(3)	5941(2)	13066(6)	5790(9)	25(2)
O(4)	6759(2)	11104(6)	5117(9)	23(2)
O(5)	6928(2)	11025(6)	9574(9)	23(2)
O(6)	5101(2)	12610(6)	7452(9)	24(2)
O(7)	5282(3)	5646(7)	6804(11)	32(2)
O(8)	6060(2)	5381(6)	4556(8)	22(1)
O(9)	6095(2)	7134(6)	9087(8)	21(1)
O(10)	6945(2)	7617(6)	6884(9)	21(1)
O(11)	7416(2)	9275(5)	5725(8)	18(1)
O(12)	7850(2)	7553(6)	7405(9)	21(1)
O(13)	7372(2)	8933(6)	9466(8)	19(1)
N(1)	5878(3)	10609(7)	7757(10)	21(1)
N(2)	5617(3)	8706(7)	7904(11)	21(1)
N(3)	4761(3)	9010(7)	7585(10)	22(1)
N(4)	4572(3)	11062(7)	7362(10)	20(1)
N(5)	3972(3)	9623(8)	7244(10)	23(2)
C(1)	5390(3)	10572(9)	7600(12)	20(1)
C(2)	5020(4)	11497(9)	7432(13)	21(2)
C(3)	4430(3)	9870(8)	7369(12)	19(2)
C(4)	5212(3)	9408(8)	7709(12)	21(1)
C(5)	6010(4)	9481(9)	7945(13)	23(2)
C(6)	5644(4)	7406(8)	8325(14)	23(1)
C(7)	5540(4)	6683(8)	6375(14)	25(2)
C(8)	6048(3)	6412(8)	5805(13)	21(2)
C(9)	6340(3)	6277(8)	7902(13)	20(1)
C(10)	6854(3)	6511(8)	7939(13)	19(2)
O(1W)	8155(2)	13119(6)	7472(9)	23(2)
O(2W)	6842(2)	5720(6)	12707(10)	30(2)
O(3W)	5531(3)	4473(8)	974(11)	44(2)

Table A-3: Bond lengths and angles for Mn-GMP.

Mn(1)-O(5)	2.118(6)
Mn(1)-O(3)	2.162(6)
Mn(1)-O(4)	2.197(6)
Mn(1)-O(1)	2.210(6)
Mn(1)-O(2)	2.227(6)
Mn(1)-N(1)	2.250(8)
P(1)-O(12)	1.496(7)
P(1)-O(11)	1.512(6)
P(1)-O(13)	1.517(6)
P(1)-O(10)	1.601(7)
O(6)-C(2)	1.260(11)
O(7)-C(7)	1.397(12)
O(8)-C(8)	1.421(10)
O(9)-C(6)	1.362(12)
O(9)-C(9)	1.438(10)
O(10)-C(10)	1.448(11)
N(1)-C(5)	1.312(13)
N(1)-C(1)	1.357(11)
N(2)-C(4)	1.374(12)
N(2)-C(5)	1.392(12)
N(2)-C(6)	1.475(12)
N(3)-C(3)	1.332(12)
N(3)-C(4)	1.328(12)
N(4)-C(2)	1.338(12)
N(4)-C(3)	1.385(12)
N(5)-C(3)	1.304(11)
C(1)-C(4)	1.391(14)
C(1)-C(2)	1.458(14)
C(6)-C(7)	1.544(13)
C(7)-C(8)	1.517(13)
C(8)-C(9)	1.585(13)
C(9)-C(10)	1.452(13)

O(5)-Mn(1)-O(3)	177.5(3)
O(5)-Mn(1)-O(4)	87.6(2)

Table A-3 continued

O(3)-Mn(1)-O(4)	94.7(2)
O(5)-Mn(1)-O(1)	92.9(2)
O(3)-Mn(1)-O(1)	88.1(2)
O(4)-Mn(1)-O(1)	91.1(2)
O(5)-Mn(1)-O(2)	81.0(2)
O(3)-Mn(1)-O(2)	96.7(3)
O(4)-Mn(1)-O(2)	168.6(3)
O(1)-Mn(1)-O(2)	88.9(2)
O(5)-Mn(1)-N(1)	91.7(3)
O(3)-Mn(1)-N(1)	87.2(3)
O(4)-Mn(1)-N(1)	90.2(3)
O(1)-Mn(1)-N(1)	175.3(3)
O(2)-Mn(1)-N(1)	90.7(2)
O(12)-P(1)-O(11)	112.3(3)
O(12)-P(1)-O(13)	112.0(3)
O(11)-P(1)-O(13)	113.7(4)
O(12)-P(1)-O(10)	109.2(4)
O(11)-P(1)-O(10)	101.9(3)
O(13)-P(1)-O(10)	107.1(3)
C(6)-O(9)-C(9)	113.6(7)
C(10)-O(10)-P(1)	120.4(5)
C(5)-N(1)-C(1)	104.5(8)
C(5)-N(1)-Mn(1)	118.8(6)
C(1)-N(1)-Mn(1)	136.6(7)
C(4)-N(2)-C(5)	106.8(8)
C(4)-N(2)-C(6)	127.4(8)
C(5)-N(2)-C(6)	125.1(8)
C(3)-N(3)-C(4)	114.4(8)
C(2)-N(4)-C(3)	127.8(9)
N(1)-C(1)-C(4)	112.6(9)
N(1)-C(1)-C(2)	133.2(9)
C(4)-C(1)-C(2)	114.1(8)
O(6)-C(2)-N(4)	121.5(9)
O(6)-C(2)-C(1)	124.7(9)
N(4)-C(2)-C(1)	113.7(9)

Table A-3 continued

N(5)-C(3)-N(3)	121.6(9)
N(5)-C(3)-N(4)	118.7(9)
N(3)-C(3)-N(4)	119.6(9)
N(3)-C(4)-N(2)	125.7(8)
N(3)-C(4)-C(1)	130.3(9)
N(2)-C(4)-C(1)	103.9(8)
N(1)-C(5)-N(2)	112.2(8)
O(9)-C(6)-N(2)	108.9(8)
O(9)-C(6)-C(7)	108.8(7)
N(2)-C(6)-C(7)	110.3(8)
O(7)-C(7)-C(8)	112.6(8)
O(7)-C(7)-C(6)	109.4(8)
C(8)-C(7)-C(6)	100.6(7)
O(8)-C(8)-C(7)	111.3(7)
O(8)-C(8)-C(9)	114.3(7)
C(7)-C(8)-C(9)	103.7(7)
O(9)-C(9)-C(10)	111.8(7)
O(9)-C(9)-C(8)	100.7(7)
C(10)-C(9)-C(8)	117.0(7)
O(10)-C(10)-C(9)	110.2(7)

Table A-4: Anisotropic displacement parameters for Mn-GMP.

	U^{11}	U^{22}	U^{33}	U^{23}	U^{13}	U^{12}
Mn(1)	29(1)	19(1)	5(1)	0(1)	3(1)	-2(1)
P(1)	33(1)	19(1)	3(1)	2(1)	4(1)	2(1)
O(1)	25(4)	27(4)	12(3)	5(3)	8(3)	-2(3)
O(2)	26(4)	24(4)	17(3)	-8(3)	5(3)	-6(3)
O(3)	37(4)	26(4)	12(3)	4(3)	4(3)	0(3)
O(4)	32(4)	34(4)	5(3)	7(3)	5(3)	4(3)
O(5)	34(4)	21(4)	14(3)	3(3)	1(3)	4(3)
O(6)	33(4)	22(3)	18(3)	0(3)	11(3)	-5(3)
O(7)	40(4)	26(4)	30(4)	2(3)	5(3)	-9(3)
O(8)	41(4)	18(3)	7(3)	-3(2)	4(2)	-4(3)
O(9)	34(3)	17(3)	11(2)	-3(2)	11(2)	3(2)
O(10)	37(3)	18(2)	9(2)	5(2)	10(2)	4(2)
O(11)	31(3)	16(3)	6(2)	6(2)	4(2)	1(2)
O(12)	28(3)	29(3)	6(2)	1(2)	0(2)	-5(2)
O(13)	31(3)	20(3)	6(2)	-2(2)	6(2)	-1(2)
N(1)	33(3)	22(3)	8(3)	-2(3)	8(3)	-5(3)
N(2)	33(3)	22(3)	8(2)	0(2)	7(2)	-1(2)
N(3)	33(3)	23(3)	9(3)	2(3)	10(3)	-2(3)
N(4)	35(3)	16(3)	8(3)	0(2)	5(3)	-3(3)
N(5)	38(4)	20(4)	11(4)	-1(3)	6(3)	-5(3)
C(1)	33(3)	23(3)	5(3)	-2(2)	7(3)	-5(3)
C(2)	35(3)	21(3)	7(3)	0(3)	1(3)	-4(3)
C(3)	33(3)	20(3)	4(3)	0(3)	9(3)	-2(3)
C(4)	34(3)	24(3)	6(3)	0(2)	9(3)	-2(3)
C(5)	32(3)	26(3)	11(3)	2(3)	5(3)	2(3)
C(6)	35(3)	21(3)	14(3)	1(3)	11(3)	1(3)
C(7)	36(3)	22(3)	18(3)	-1(3)	4(3)	1(3)
C(8)	37(3)	17(3)	10(3)	-2(3)	8(3)	3(3)
C(9)	37(3)	15(3)	9(3)	0(2)	9(3)	7(3)
C(10)	37(3)	15(3)	7(3)	6(3)	9(3)	4(3)
O(1W)	40(4)	24(4)	4(3)	-1(3)	-1(3)	-5(3)
O(2W)	39(4)	35(4)	16(4)	11(3)	19(3)	12(3)
O(3W)	48(5)	60(6)	25(4)	-24(4)	5(3)	12(4)

Table A-5: Hydrogen coordinates and isotropic displacement for Mn-GMP.

	x	y	z	U(eq)
H(1O1)	7182	13469	8373	25
H(2O1)	7100	13555	6325	25
H(102)	6425	13355	10901	33
H(2O2)	5953	12992	10475	33
H(1O3)	5807	13139	6890	30
H(2O3)	6171	13184	5035	30
H(1O4)	6583	11340	4116	28
H(2O4)	7035	11046	4646	28
H(1O5)	7189	11415	9776	35
H(2O5)	6801	10910	10680	35
H(7B)	5087	5486	5834	48
H(8B)	6301	5418	3858	33
H(4A)	4339	11598	7304	24
H(5B)	3875	8872	7302	27
H(5C)	3759	10206	7102	27
H(5A)	6335	9224	8092	27
H(6A)	5403	7190	9323	27
H(7A)	5363	7180	5325	30
H(8A)	6174	7118	5074	25
H(9A)	6287	5453	8441	24
H(10A)	6984	6575	9347	23
H(10B)	7018	5837	7298	23
H(1W1)	7907	13488	7000	27
H(2W1)	8420	13371	8009	27
H(1W2)	6730	5742	13859	36
H(2W2)	7046	5679	11814	36
H(1W3)	5752	4089	429	53
4(1W3)	5426	5101	388	53

Table A-6: Crystal data and structure refinement for Mn-phosphate.

Identification code	vdr5	
Empirical formula	H8 Mn O16 P4	
Formula weight	442.88	
Temperature	110(2) K	
Wavelength	0.71073 Å	
Crystal system	Triclinic	
Space group	P-1	
Unit cell dimensions	a = 5.357(4) Å	α= 100.334(15)°.
	b = 7.203(5) Å	β= 97.718(17)°.
	c = 8.177(6) Å	γ = 92.472(14)°.
Volume	306.8(4) $Å^3$	
Z	1	
Density (calculated)	2.397 Mg/m^3	
Absorption coefficient	1.690 mm^{-1}	
F(000)	221	
Crystal size	0.30 x 0.20 x 0.10 mm^3	
Theta range for data collection	2.56 to 23.22°.	
Index ranges	-5<=h<=5, -7<=k<=7, -8<=l<=9	
Reflections collected	791	
Independent reflections	791 [R(int) = 0.0000]	
Completeness to theta = 23.22°	91.1 %	
Absorption correction	Semi-empirical from equivalents	
Max. and min. transmission	0.8492 and 0.6311	
Refinement method	Full-matrix least-squares on F^2	
Data / restraints / parameters	791 / 0 / 97	
Goodness-of-fit on F^2	1.083	
Final R indices [I>2sigma(I)]	R1 = 0.0535, wR2 = 0.1397	
R indices (all data)	R1 = 0.0551, wR2 = 0.1410	
Largest diff. peak and hole	0.945 and -0.676 $e.Å^{-3}$	

Table A-7: Atomic coordinates for Mn-phosphate.

	x	y	z	U(eq)
Mn(1)	0	0	10000	8(1)
P(2)	510(2)	3250(2)	7504(2)	8(1)
P(1)	5635(2)	1768(2)	12309(2)	7(1)
O(1)	5499(6)	3518(5)	13737(4)	10(1)
O(2)	8267(6)	1845(4)	11878(4)	10(1)
O(3)	5310(7)	-30(5)	13137(4)	11(1)
O(4)	3517(6)	1678(4)	10880(4)	9(1)
O(5)	-1062(6)	1869(5)	8198(4)	10(1)
O(6)	3021(6)	3943(5)	8679(4)	11(1)
O(7)	-884(6)	5017(5)	7223(4)	11(1)
O(8)	1133(7)	2344(5)	5735(4)	12(1)

Table A-8: Bond lengths and angles for Mn-phosphate.

Mn(1)-O(4)	2.157(4)
Mn(1)-O(4)#1	2.157(4)
Mn(1)-O(2)#2	2.177(3)
Mn(1)-O(2)#3	2.177(3)
Mn(1)-O(5)#1	2.204(3)
Mn(1)-O(5)	2.204(3)
P(2)-O(5)	1.510(4)
P(2)-O(7)	1.540(4)
P(2)-O(6)	1.550(4)
P(2)-O(8)	1.562(4)
P(1)-O(2)	1.500(4)
P(1)-O(4)	1.506(4)
P(1)-O(1)	1.568(3)
P(1)-O(3)	1.578(4)
O(2)-Mn(1)#4	2.177(3)
O(4)-Mn(1)-O(4)#1	180.000(1)
O(4)-Mn(1)-O(2)#2	91.22(13)
O(4)#1-Mn(1)-O(2)#2	88.78(13)
O(4)-Mn(1)-O(2)#3	88.78(13)
O(4)#1-Mn(1)-O(2)#3	91.22(13)
O(2)#2-Mn(1)-O(2)#3	180.000(1)
O(4)-Mn(1)-O(5)#1	89.86(13)
O(4)#1-Mn(1)-O(5)#1	90.14(13)
O(2)#2-Mn(1)-O(5)#1	89.35(13)
O(2)#3-Mn(1)-O(5)#1	90.65(13)
O(4)-Mn(1)-O(5)	90.14(13)
O(4)#1-Mn(1)-O(5)	89.86(13)
O(2)#2-Mn(1)-O(5)	90.65(13)
O(2)#3-Mn(1)-O(5)	89.35(13)
O(5)#1-Mn(1)-O(5)	180.000(1)
O(5)-P(2)-O(7)	112.6(2)
O(5)-P(2)-O(6)	112.13(19)
O(7)-P(2)-O(6)	107.3(2)
O(5)-P(2)-O(8)	110.9(2)

Table A-8 continued

O(7)-P(2)-O(8)	104.9(2)
O(6)-P(2)-O(8)	108.7(2)
O(2)-P(1)-O(4)	116.6(2)
O(2)-P(1)-O(1)	106.73(19)
O(4)-P(1)-O(1)	111.29(19)
O(2)-P(1)-O(3)	107.2(2)
O(4)-P(1)-O(3)	108.7(2)
O(1)-P(1)-O(3)	105.8(2)
P(1)-O(2)-Mn(1)#4	130.51(19)
P(1)-O(4)-Mn(1)	135.7(2)
P(2)-O(5)-Mn(1)	131.26(19)

Table A-9: Anisotropic displacement parameters for Mn-phosphate.

	U^{11}	U^{22}	U^{33}	U^{23}	U^{13}	U^{12}
Mn(1)	8(1)	6(1)	8(1)	-2(1)	2(1)	0(1)
P(2)	8(1)	8(1)	7(1)	-2(1)	-1(1)	-1(1)
P(1)	7(1)	6(1)	7(1)	-4(1)	1(1)	0(1)
O(1)	9(2)	8(2)	9(2)	-8(1)	-1(1)	2(1)
O(2)	9(2)	8(2)	12(2)	-5(1)	2(1)	1(1)
O(3)	8(2)	13(2)	10(2)	2(1)	1(1)	-4(2)
O(4)	10(2)	6(2)	9(2)	0(1)	-2(1)	2(1)
O(5)	9(2)	9(2)	11(2)	-1(1)	-3(1)	-5(1)
O(6)	8(2)	10(2)	13(2)	3(1)	-4(1)	-6(1)
O(7)	8(2)	5(2)	18(2)	-1(1)	2(1)	-3(1)
O(8)	13(2)	15(2)	7(2)	-3(1)	1(1)	7(2)

Table A-10: Hydrogen coordinates and isotropic displacement for Mn-phosphate.

	x	y	z	U(eq)
H(1A)	4148	4038	13530	15
H(3A)	3935	-638	12705	16
H(6A)	3264	3258	9407	16
H(8)	2245	1602	5474	18

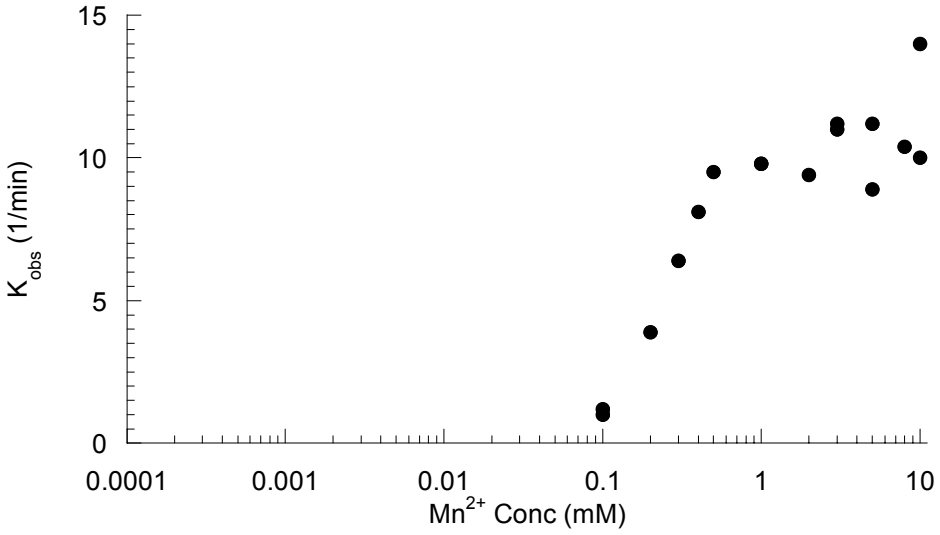

Figure A-1: Catalytic activity of dG10.1 modified hammerhead ribozyme. Excess enzyme was used to ensure single turnover conditions. Conditions were 3 μM RNA at room temperature.

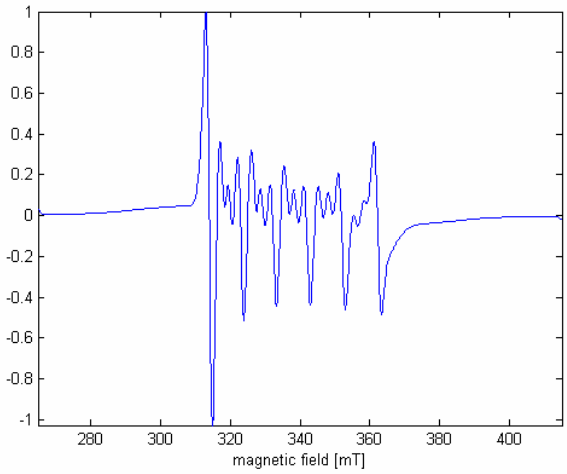

Line width = 15 G
D = 400 MHz
E = 133 MHz
D strain = 1
G strain = 0
A strain = 0

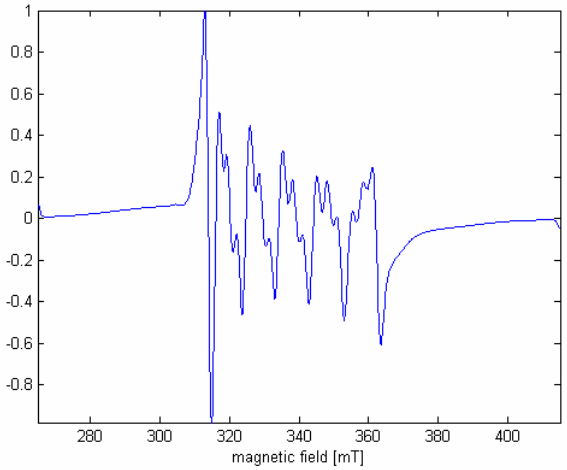

Line width = 15 G
D = 500 MHz
E = 166 MHz
D strain = 1
G strain = 0
A strain = 0

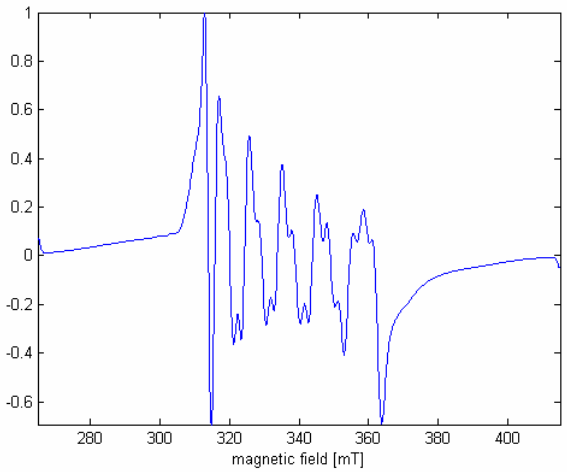

Line width = 15 G
D = 600 MHz
E = 200 MHz
D strain = 1
G strain = 0
A strain = 0

Figure A-2: EPR simulations and parameters.

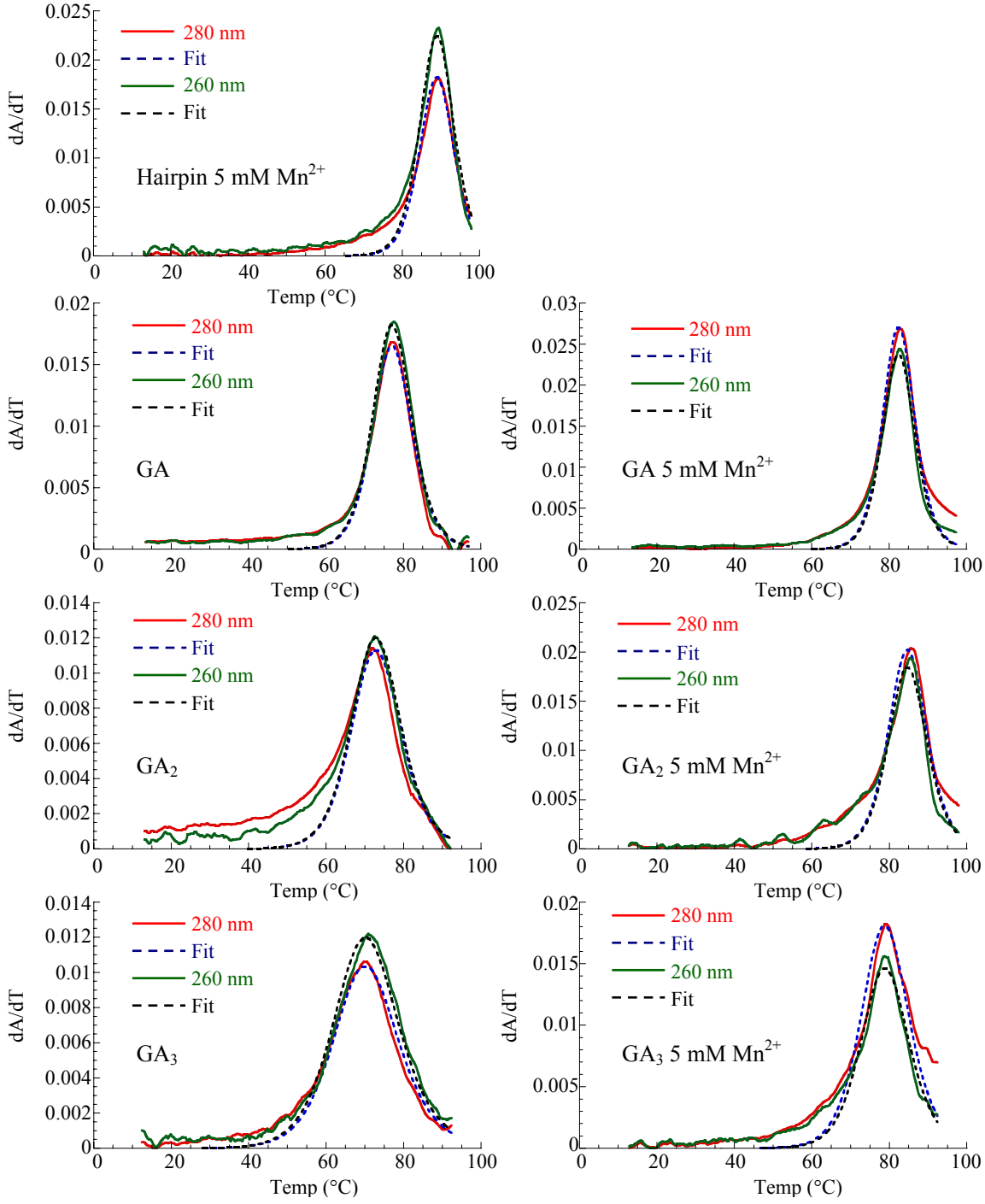

Figure A-3: Melt fits for GA containing hairpin sequences. All melt profiles were fit using the program Tmelt operating on Unix workstation.

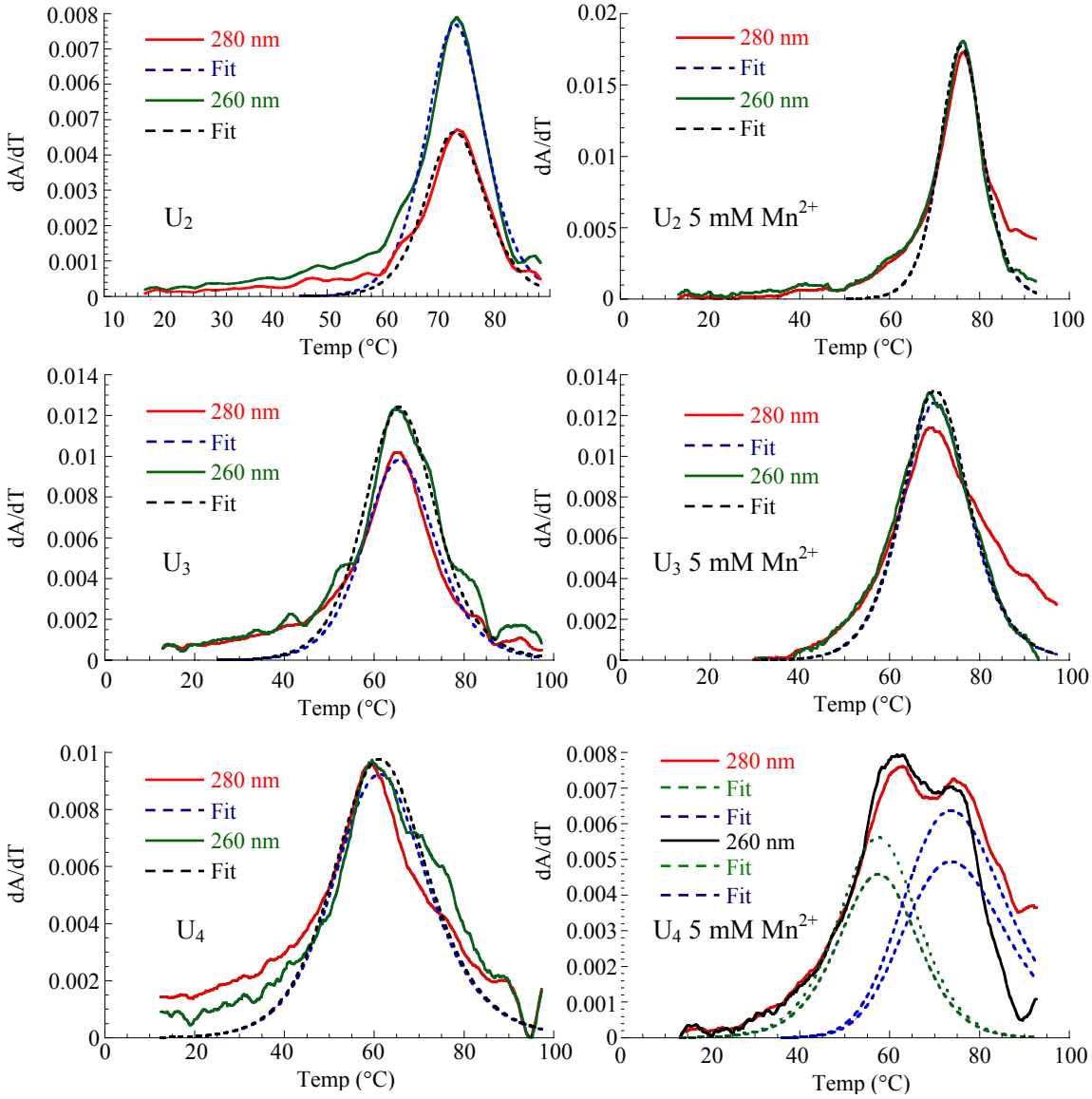

Figure A-4: Melt fits for UU containing hairpin sequences. All melt profiles were fit using the program Tmelt operating on Unix workstation.

VITA

Matthew Vogt was born in Paterson, New Jersey on March 6, 1975. He was raised in Wayne, New Jersey where he attended and graduated from Wayne Hills High School in June of 1993. He went on to attend Trenton State College located in Ewing, New Jersey where he received a Bachelor of Science Degree in chemistry in May of 1997. In the fall of 1998, he began his graduate research under the direction of Dr. Victoria J. DeRose at Texas A&M University. The author may be contacted through his parents at 82 Farmingdale Road, Wayne, NJ 07470.